Università di Pisa

Facoltà di Scienze Matematiche Fisiche e Naturali

Corso di laurea Magistrale in Fisica

Anno Accademico 2010/2011

Tesi di laurea magistrale

Observation and study of the X(3872) particle with the CMS experiment at LHC

Candidate
Alberto Vesentini

Supervisor
Dott. Fabrizio Palla

Abstract

The discovery of the $X(3872)$ resonance in the decay channel $J/\psi\pi^+\pi^-$ by Belle Collaboration in 2003 opened up a new chapter in the QCD landscape. Its subsequent observation in other experiments confirms the existence of this new particle.

The properties of $X(3872)$ are not in agreement with being a charmonium state. Different interpretations are still under study. One possible option is that it is a molecule of D^* mesons, another one is that it is a hybrid of bound state and a tetra-quarks state.

In this thesis it will be reported the study of the $X(3872)$ particle in the CMS experiment, at LHC, in the 2010 and a first view at the 2011 data. The observed decay channel is that one into a J/ψ (reconstructed with a muons pair) and a pions pair ($\pi^+\pi^-$).

The CMS experiment, one of the two general purpose experiments in the LHC collider, has an impressive performance in the tracks and muons detection and reconstruction, due to the superior tracking performances. This allows the detection of high purity signal for the J/ψ mesons and to reconstruct the $X(3872)$ particle.

In this thesis it will be shown the measurement procedure of the production cross section ratio of the $X(3872)$ and $\psi(2S)$ in the same decay channel, using the statistics collected by CMS at $\sqrt{s} = 7\,TeV$ at LHC in 2010, corresponding to $\sim 40\,pb^{-1}$ of integrated luminosity. The measurement of the ratio is convenient because of the cancellation of the errors, such the one of the luminosity and the one of the trigger. The value of the ratio is: $R = 0.084 \pm 0.017(stat.) \pm 0.009(syst.)$.

The increased number of reconstructed $X(3872)$, 5325 ± 358, in the 2011 collisions permits to continue the study of this particle. More study is undergoing, in this thesis it will be also shown a preliminary look at the first part of the 2011 data and a study of the non-prompt composition of the $X(3872)$ in the data.

Acknowledgements

I would like to thank Fabrizio Palla for his assistance and for the helpful suggestions he gave me during my work. His passion for his job and his experience in experimental physics have been a lighthouse for my works. I also would like to thank the $X(3872)$ group in CMS at CERN: D. Fasanella, A. Fanfani, M. Giunta, A. Meyer, X. Wang, J. Wang and the others for showing me the way with their wonderful work. I am grateful to L. Martini, F. Fiori, J. Bernardini and others from the Pisa group for giving me the right paths and codes to follow.

Then, I would like to thank my parents and my brother. Without their patience and support I could not arrive at this final step. I want to dedicate my thesis to them.

I would like to say thank to my girlfriend, Michela, without her encourage and force I would be lost many times. She helped me with the codes and with the calculations I forgot to do. She also takes jokes on me.

Many thanks to my old friends: Casto, Mona, Phil (ϕl) and the Marmirolo crew for their support, even if we are so far away.

And also to all the people I met in Pisa: the physics colleagues, the choir people, the room-mates ... thank you.

Contents

1 Introduction **1**

2 The LHC collider and the CMS experiment **3**

2.1 The LHC machine and the experiments 3

2.1.1 The Large Hadron Collider 4

2.1.2 The Compact Muon Solenoid 5

2.1.2.1 The solenoid 9

2.1.2.2 The electromagnetic calorimeter 9

2.1.2.3 The hadronic calorimeter 10

2.1.2.4 Trigger and data acquisition 11

3 The tracker and muon systems **15**

3.1 Overview 15

3.2 Layout 16

3.2.1 The pixel detector 17

3.2.2 The silicon strip 19

3.3 First operations 20

3.3.1 Tracker alignment 21

3.3.2 Physics performance 22

3.3.2.1 Track Reconstruction 22

3.3.2.2 Distributions of invariant masses 23

3.4 The Muon system 26

3.4.1 Physics performance 29

4 The Quark Model **35**

4.1 The history 35

4.2 Reaching the parton model 36

4.3 The theory of the quark model 39

4.3.1 The symmetry group 41

4.3.1.1 Compositions of representations 45

4.4 Quantum Chrodynamics and hadron production 47
4.5 The X(3872) particle 50
4.5.1 The interpretations 52
4.5.2 The charmonium production at LHC 54

5 Cross section measurement of the X(3872) with CMS 59
5.1 The overview 59
5.1.1 Samples used 60
5.1.2 Trigger and event selection 62
5.1.2.1 $J/\psi \to \mu^+\mu^-$ selection 62
5.1.2.2 $J/\psi \to \mu^+\mu^-\pi^+\pi^-$ selection 63
5.1.2.3 Acceptance and efficiency 66
5.1.3 Measurement of the non-prompt component 71
5.1.4 Systematic uncertainties 75
5.1.5 Data-driven cross check of pion acceptance and efficiency 78
5.1.6 Result 82
5.1.7 Kinematic properties of the signal using the sideband subtraction method 83
5.2 The 2011 data 84

6 Conclusions and prospects 89

Bibliography 91

1

Introduction

The actual particle physics world is quite well described by the Standard Model (SM). This model classifies all the building blocks as *quarks* and *leptons* on one side, and the *gauge bosons* carrying the electroweak force (γ, Z and $W^{\pm}$) and the strong interaction (g, *gluons*), figure 1.1. The part of SM that describes the quark interactions is called Quantum Chromodynamic (QCD).

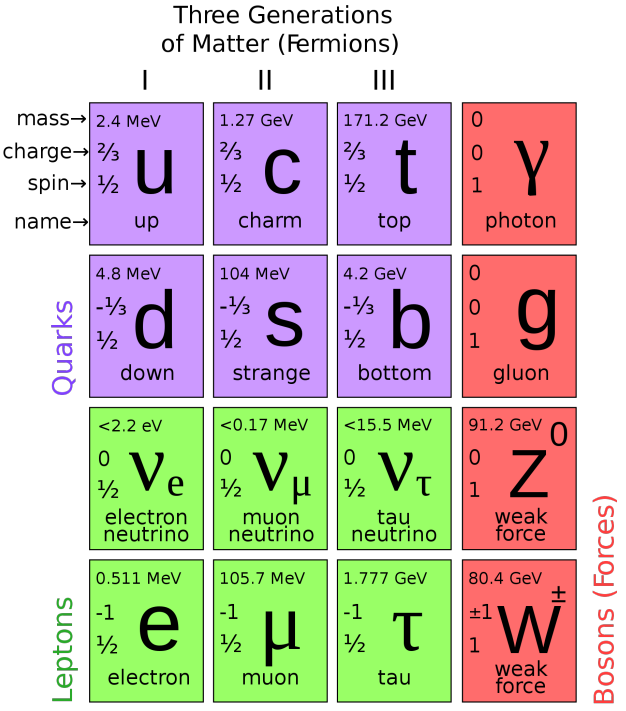

Figure 1.1: Particles and mediator of the forces of the Standard Model.

Since every quark and anti-quark, carries a colour charge and particles have to be colourless, the easiest cases are to build combinations with $q\bar{q}$ and qqq. The particles made by a quark anti-quark couple are called *mesons* and the particles made with three

quarks are called *baryons*. QCD theory explains how to build hadrons with several numbers of quarks to obtain colourless combinations and also describes the dynamics of them.
There could be other particles not described by this scheme: they are called *exotic*: Gell-Mann, predicted their possible existence in the original formulation of the quark model.
In the last decade, several exotic particles were discovered, named $X(3872)$, $Y(2175)$ and $Z(4433)$. Many experiments had seen these particles, and recently there are also seen by the LHC experiments (CMS and LHCb). There are different explanations for these particles. One possibility is that they are composed by two *mesons*, as a $[cd][\overline{c}\overline{d}]$ bound state. Another option is that they could be a tetraquark state, another one is that they could be a sort of molecule of mesons (for example D^*).
In this thesis I will discuss the $X(3872)$, its observation in the CMS experiment and the ongoing study on its properties. I will show the measurement of the ratio of the cross section of the $X(3872)$ with respect to the $\psi(2S)$.
At first, I will give an overview of the CMS experiment, with particular attention to the tracker and the muon systems, used for the reconstruction. The tracker is made by silicon pixel and strip detectors, and it has incredible performances in the reconstruction of the tracks. The muon system is based on different detector technology like drift tubes and cathode strip chambers. For example, the J/ψ meson is reconstructed through the cleanest and more efficient decay in CMS, the one into two muons.
Then I will discuss the QCD theory of the quark model based on the $SU(3)$ group and the history of the $X(3872)$ particle. The production mechanism and the decay of the charmonium state, one of the candidate to the $X(3872)$ interpretations, are important to best comprehend the real behave of this kind of particles.
Finally I will present my analysis on MonteCarlo simulation and 2010 and 2011 data in the CMS experiment. The measurement of the ratio of the cross section is shown with details. The ratio is calculated using the decay channel into $J/\psi\pi^+\pi^-$ of two particles: the $X(3872)$ and the $\psi(2S)$, a charmonium state. It is used a particular method to measure the pions efficiency: the ratio of other two decays, $\psi(2S) \to J/\psi\pi^+\pi^-$ over $\psi(2S) \to \mu^+\mu^-$.
A preliminary study on the prompt non-prompt component of the $X(3872)$ is shown.
Finally, using the 2011 data a rapid overview of the invariant mass spectrum is given.

2

The LHC collider and the CMS experiment

An overview of the LHC collider and a focus on the CMS experiment will be given in this chapter. All the sub-components of the detector will be viewed rapidly: the solenoid, the calorimeters (hadronic and electromagnetic) and the system of the trigger and the data acquisition.
A detailed description of the tracker and muon system will be given in the chapter 3.

2.1 The LHC machine and the experiments

After 20 years of design and construction, under the border between France and Switzerland is placed the brand new laboratory for the high energy physics, the Large Hadron Collider. This complex system accelerates protons beams in bunch over the $27\,km$ of circumference; on that there are positioned four great particle experiments over the four interaction points: ALICE, ATLAS, CMS and LHCb.

- *ALICE* (*A Large Ion Collider Experiment*) is positioned in the Interaction Point 2, and works both with the *pp* run and with the special LHC running with lead ions, to understand the first instants of the universe, when there was a gluon-quark plasma.

- *ATLAS* (*A Toroidal LHC ApparatuS*) is placed in the Interaction Point 1. It is one of the two general purpose experiments and it studies a wide range of physics: the search for the Higgs boson particle, extra dimensions and particles that could make up the dark matter, and new physics that could appear at the LHC scale of energy.

- *CMS* (*Compact Muon Solenoid*) in the Interaction Point 5 is the other general purpose experiment. It examines the same physics of the ATLAS experiment, but with different technical solutions and design.

- *LHCb* (*LHC beauty*) located in the Interaction Point 3 helps to understand the reason that we see only matter instead of antimatter in the universe. In particular it studies the the physics of the *b*-quark to comprehend it.

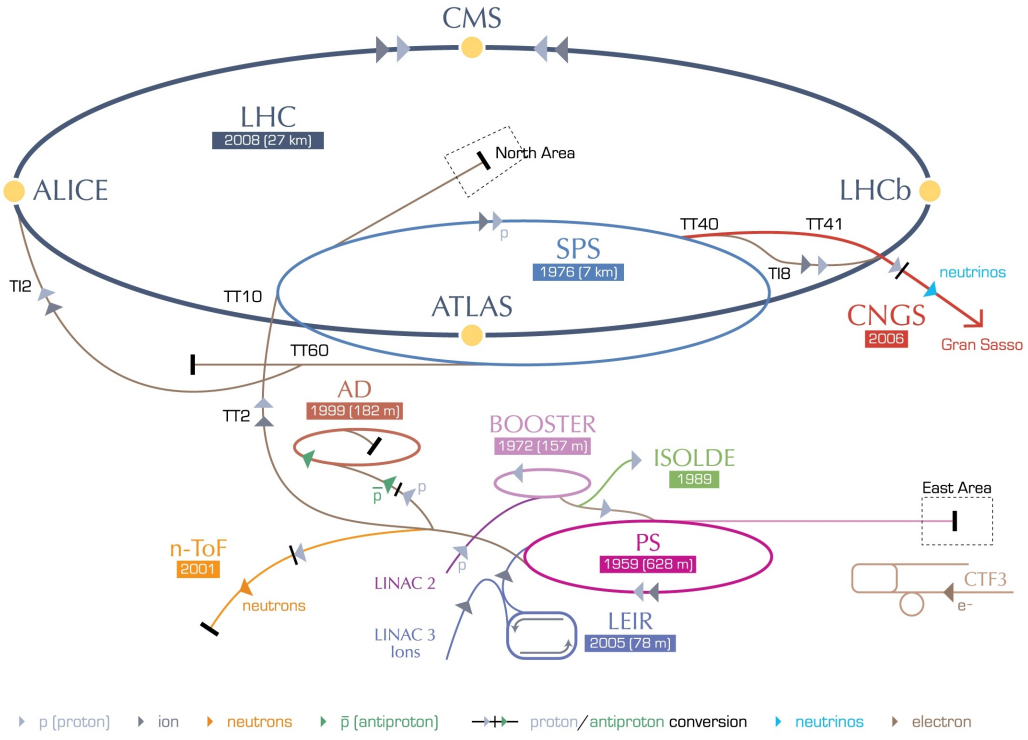

Figure 2.1: LHC accelerator system

2.1.1 The Large Hadron Collider

The LHC (Large Hadron Collider) is constructed in the previous LEP tunnel. It will ultimately deliver head-on collisions of two proton beams of $7\,TeV$ at the design luminosity of $10^{34}\,cm^{-2}s^{-1}$. It can also provide collisions of ion leads with an energy per ion of $2.75\,TeV$, the luminosity in this case would be of $10^{27}\,cm^{-2}s^{-1}$.

The main motivation of LHC is to give lights on the electroweak symmetry breaking, for which the Higgs mechanism is presumed to be responsible. Other new tests will be possible at the energy of the TeV, like the searching for physics beyond the Standard Model and the Supersymmetry (SUSY), that would be the prosecution of the model, but with a lot of new particles with a mass bigger than the known ones. Hence, there are many reasons to investigate the TeV energy scale.

At each of the four interaction points, the particle bunches collides with a frequency of $40\,MHz$, each bunch contains up to 1.15×10^{11} protons. The large number of particles

per bunch increases the number of the interesting events, but also puts problems with the multiple interactions per crossing (*pile-up*). For the low luminosity run ($2 \times 10^{33}\, cm^{-2}s^{-1}$) there will be 5 inelastic interactions per bunch crossing, for the high luminosity run ($10^{34}\, cm^{-2}s^{-1}$) these are 25, on average. This complicate the analysis since the particles of the investigated reaction have to be distinguished from the particles of the additional minimum bias events.

At the beginning of 2010 the machine started to accelerate proton beams and the experiments began to collect data from pp collisions at $\sqrt{s} = 7\,TeV$ with low luminosity $2 \times 10^{32}\, cm^{-2}s^{-1}$, and from lead ion collisions in the final part of the year. The integrated luminosity stored was about $40\, pb^{-1}$.

The correct operations of the machine allows in the 2011 to increase the luminosity (to few $10^{33}\, cm^{-2}s^{-1}$) and to continue the data taking. At the moment, the total stored data is $\sim 2\, fb^{-1}$.

2.1.2 The Compact Muon Solenoid

The CMS experiment (Compact Muon Solenoid) is one of the two general purpose experiments of the LHC [1].

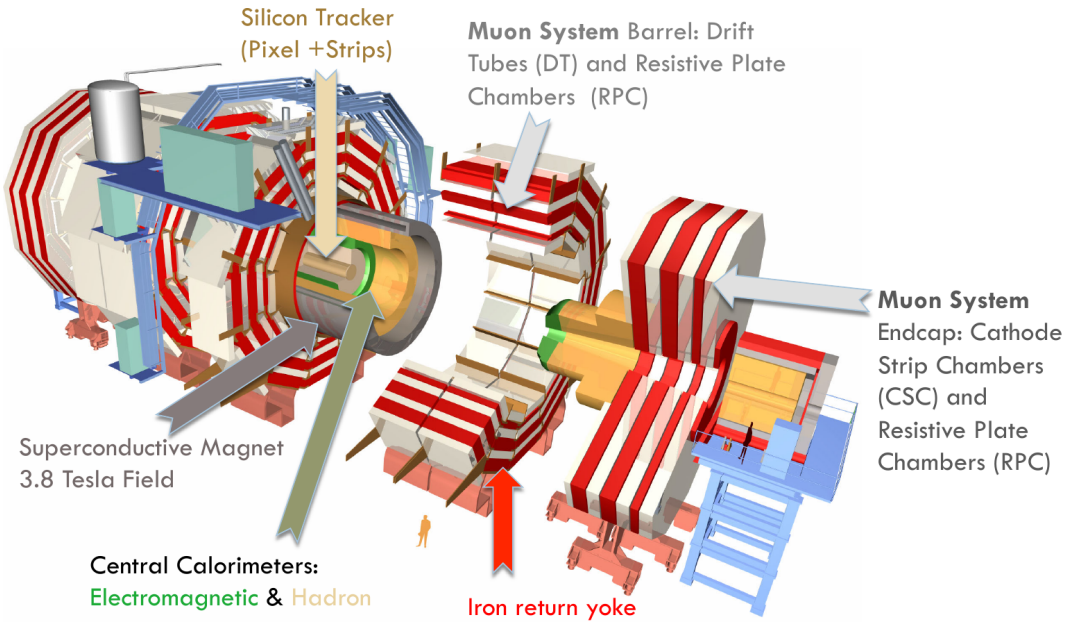

Figure 2.2: The CMS experiment with its subsystem.

Located in the Interaction Point 5, its main physics program is the research of the Higgs boson, the physics of the Standard Model as well as the physics beyond it. Hadron colliders are well suited in the task of exploring new energy domains, and the region around the $1\,TeV$ constituent the centre of mass energy can be explored if the proton energy and the luminosity are sufficiently high.

At the $\sqrt{s} = 14\,TeV$ the expected total proton-proton cross section is roughly $100\,mb$. With the designed luminosity the general purpose detector observes an event rate of approximately $10^9\,events/s$. With these numbers the challenge for the detector is impressive. The on-line event selection process, the *trigger*, must reduce of 10^7 times the huge rate of events/s for the storage and the successive analysis. Another problem for the read-out system is the short time between bunch crossing, of $25\,ns$: this has implications on the design and the trigger system.
25 inelastic collisions will be superimposed to the interested event at the design luminosity: around 1000 charged particle will emerge from the interaction region, every $25\,ns$. The products of an interesting interaction may be confused with those interactions form minimum bias: the problem is more severe when the electronic response is longer than the $25\,ns$ required.
These problem can be reduced by using high-granularity detectors with good time resolution. The resulting millions of channels of the detector electronic required have to be very good synchronized.
Due to the high radiation level in the interaction region, the detectors device (detectors and front-end electronics) must be able to support high radiation levels.
The requirement for the CMS detector to approach the goals of the LHC physics programme, can be summarized as follows:

- Good muon identification and momentum resolution in a wide range of momenta and angles, good dimuon mass resolution ($\sim 1\%$ at $100\,GeV$), and the ability to determine unambiguously the charge of muon with $p < 1\,TeV$;

- Good charged-particle momentum resolution and reconstruction efficiency in the inner tracker. Efficient triggering and off-line tagging of $\tau's$ and b-jets, requiring pixel detector close to the interaction region;

- Good electromagnetic energy resolution, good diphoton and dielectron mass resolution ($\sim 1\%$ at $100\,GeV$), wide geometric coverage, π^0 rejection, and efficient photon and lepton isolation at high luminosities;

- Good missing-transverse-energy and dijet-mass resolution, requiring hadron calorimeters with a large hermetic geometric coverage with fine lateral segmentation.

An important feature guiding the detector design and layout is the choice of the magnetic field configuration for the measurement of the muons momentum. A large bending power is necessary to measure with precision the momentum of the charged particle with high-energy, this forces the choice of a magnet with a superconducting technology.
At the heart of CMS sits a superconducting solenoid with a magnetic field of $4\,T$ providing

a large bending power ($12\,Tm$) before the muon bending angle is being measured by the muon system. The dimensions are $13\,m$ long and $6\,m$ of inner diameter. The return field is large enough to saturate $1.5\,m$ of iron, allowing the 4 muon stations to be integrated to ensure robustness and full geometric coverage. Each muon station consists of several layers of aluminium drift tubes (DT) in the barrel region and the cathode strip chambers (CSC) in the endcap region, complemented by resistive plate chambers (RPC). See figure: 2.2 for a sketch of the detector.

The borehole of the magnet coil is large enough to receive the inner tracker and the calorimetry systems. The tracking volume is given by a cylinder of $5.8\,m$ length and $2.6\,m$ diameter. Dealing with high track multiplicities CMS employs layers of silicon microstrip detectors, that provide the granularity and precision needed. In addiction to that, there are 3 layers of silicon pixel detectors in the barrel region and 2 disks in the forward region to improve the measurement of the impact parameter of the charged particle tracks, as well as the position of the primary and secondary vertices. The muon momentum resolution using only the muon system, using only the inner track and using both of the sub-detectors is shown in figure 2.3.

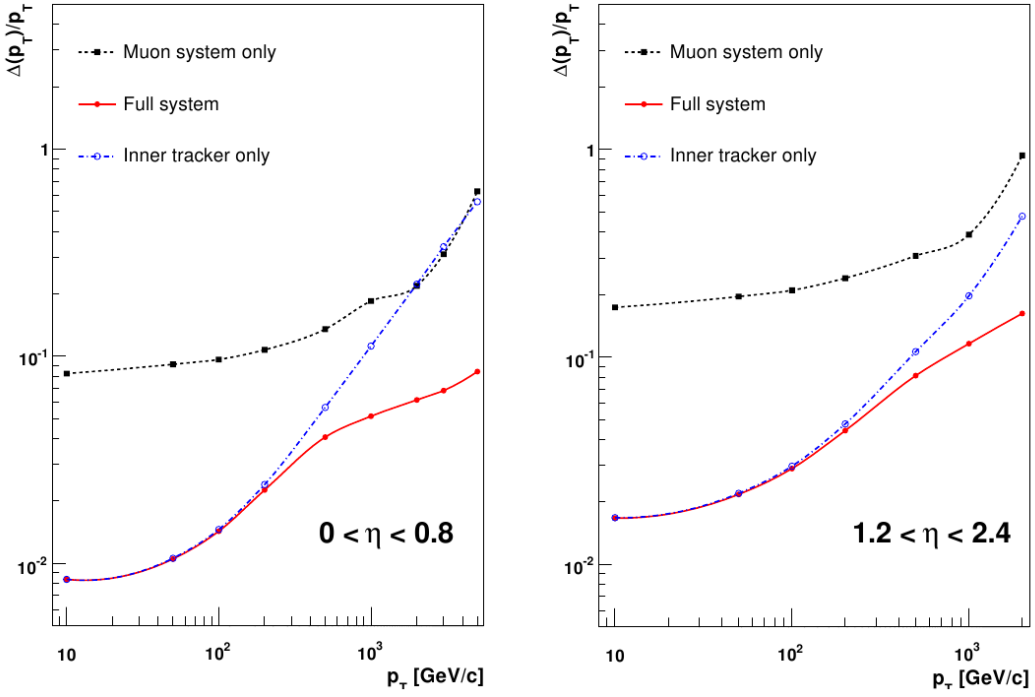

Figure 2.3: The muon transverse-momentum resolution as a function of the transverse-momentum (p_T) using the muon system only, the inner tracking only, and both. Left panel: $|\eta| < 0.8$, right panel: $1.2 < |\eta| < 2.4$

The electromagnetic calorimeter (ECAL) technology is based on lead tungstate ($PbWO_4$) crystal with coverage in pseudorapidity up to $|\eta| < 3.0$. The scintillation light is detected by silicon avalanche photodiodes (APDs) in the barrel region, and by vacuum phototriodes

(VPTs) in endcap region. A preshower system is placed in the front of the endcap ECAL for the rejection of π^0.

The ECAL is surrounded by a brass/scintillator sampling hadron calorimeter (HCAL) with coverage up to $|\eta| < 3.0$. The scintillator light is converted by wavelenghts-shifting (WLS) fibres embedded in the scintillator tiles and channelled to photodetectors via clear fibers. The light is received by photodetectors (hybrid photodiodes, or HPDs) that can provide gain and operate in high axial magnetic fields. This central calorimeter is complemented by a "tail-catcher" in the barrel region (HO) outside the coil ensuring that hadronic showers are sampled with nearly 11 hadronic interaction lengths (λ_I). Other coverage till $|\eta| \sim 5.0$ is provided by an iron/quartz-fibre calorimeter (HF, hadron forward). The Cerenkov light emitted in the quartz fibres is collected by photomultipliers. The forward calorimeters assure the full geometric coverage for the transverse energy in the event measure. Another forward coverage is obtained by additional dedicated detectors, as CASTOR. The expected jet transverse energy resolution in various pseudorapidity region is shown in figure 2.4. The ECAL thickness is larger than 25 X_0 radiation lengths, while the HCAL depths varies in the range 7-11 λ_I ($10 - 15\lambda_I$ with the HO included), depending on pseudorapidity.

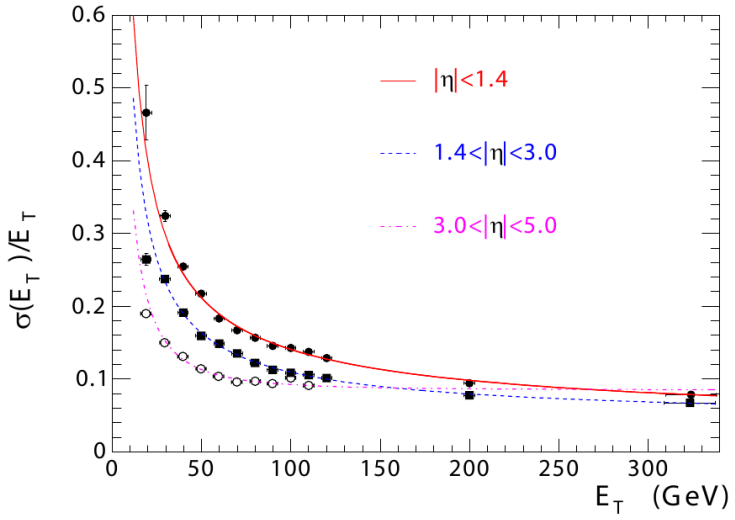

Figure 2.4: The jet transverse-energy resolution as a function of the jet transverse energy for barrel jets ($|\eta| < 1.4$), endcap jets ($1.4 < |\eta| < 3.0$), and very forward jets ($3.0 < |\eta| < 5.0$). The jets are reconstructed with an iterative cone algorithm (cone radius = 0.5).

Here I present an overview of the different part of the CMS detector: the solenoid, the hadron and electromagnetic calorimeters, the system of the data acquisition and the trigger.

Due to the important use in my analysis of the inner tracker and the muon systems, they are showed more precisely in the next chapter.

2.1.2.1 The solenoid

The superconductive solenoid magnet is run to provide a homogeneous magnetic field of $3.8\,T$ in a free bore diameter of $6\,m$ and $12.5\,m$ length with a stored energy of $2.6\,GJ$ at full current regime.
The flux is returned through a $10000\,t$ yoke comprising 5 wheels and 2 endcaps, composed of three disks each. The distinctive feature of the $220\,t$ cold mass is the 4 layers winding made from a stabilized reinforced NbTi conductor. The ratio between stored energy and cold mass is high (about $11.6\,KJ/Kg$), that causes a large mechanical deformation (0.15%) during energizing, well beyond the values of the previous solenoidal detectors magnets.
The superconducting solenoid presents three new features with respect to the previous detector ones:

- dealing with an high current per turn ($41.7\,MA - turn$) to generate the $4\,T$ magnetic field, the winding is composed of 4 layers, instead of the usual 1 (as in LEP experiment, Aleph and Delphi) or 2 (as in ZEUS, at DESY and BaBar, at SLAC, coils);
- the conductor, made from a Rutherford-type cable co-extruded with pure aluminium is mechanically reinforced with an aluminium alloy;
- the dimensions of the solenoid are very large ($6.3\,m$ of cold bore, $12.5\,m$ of length, $220\,t$ mass)

It is also used to measure the transverse momentum p_T of the charged particle together with the tracker. The design was chosen large enough to install all calorimeters systems inside the solenoid.This setup avoids scattering, absorption, and showering of particles in the solenoid material before entering in the calorimeters, which would degrade the resolution of the electromagnetic and hadronic energy measurement. The exception is the so-called tail-catcher of the HCAL, which is installed centrally to ensure the measurement of high transverse momentum jets. The magnetic flux is returned through saturated iron, the so-called return yoke.

2.1.2.2 The electromagnetic calorimeter

The electromagnetic calorimeter, ECAL, is a hermetic homogeneous calorimeter made of 61200 lead tungstate ($PbWO_4$) crystals mounted in the central barrel part, closed by 7324 crystals in each of two endcaps.

A preshower detector is placed in front of the endcap crystals for an extra spatial precision: this allows CMS to distinguish between single high-energy photons and pairs of low-energy photons. The preshower detector is a sampling calorimeter, based on two sequential lead absorber plates instrumented with silicon strip sensors for the energy and position measurement.

Avalanche photodiodes (APDs) are used as photodetectors in the barrel and vacuum phototriodes (VPTs) in the endcaps. The use of high density crystals has allowed the design of a calorimeter which is fast, has fine granularity and is radiation resistant, all important characteristics in an LHC experiment.

With the 2010 collisions it is possible to make the first calibration with *real* data [2]. The percentage of fully working channels in the electromagnetic barrel (EB) is about 99.30% and in the electromagnetic endcap (EE) is about 98.94%, while in the shower (ES) the fully strips functional is 99.79% and the resolution of electrons of 120 GeV is 0.5%.

In the figure 2.5 it is shown the energy spectra measured in individual EB channels from the data and Monte Carlo simulation and the azimuthal distribution of the channel with the highest reconstructed energy.[3]

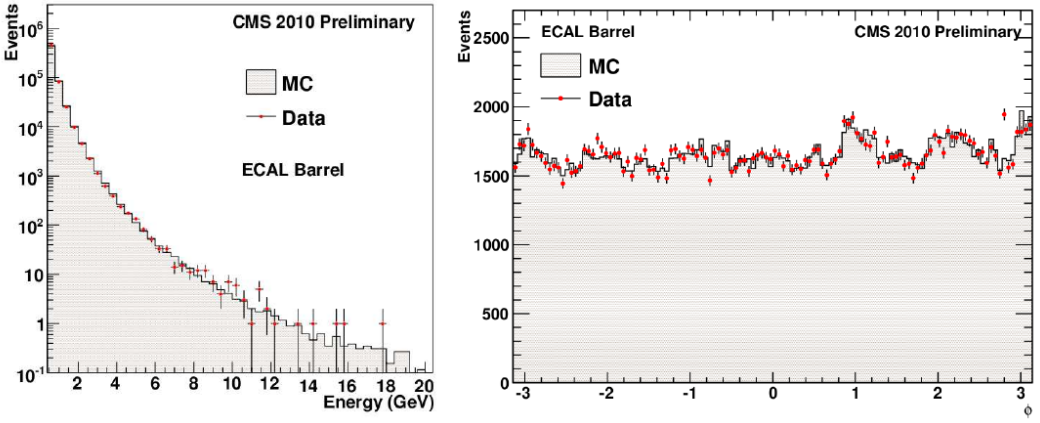

Figure 2.5: Left: single channel energy spectrum; Right: azimuthal distribution of the channel with the highest reconstructed energy; from 7 TeV minimum bias collision events

2.1.2.3 The hadronic calorimeter

The hadron calorimeters are important for the measurement of hadron jets and neutrinos, or exotic particles resulting with apparent missing transverse energy. Behind the tracker and the electromagnetic calorimeter sit the hadronic calorimeter barrel and endcaps, seen from the interaction point. The hadron calorimeter barrel (HB) is radially restricted between the outer extent of the electromagnetic calorimeter ($R = 1.77\,m$) and the inner extent of magnet coil ($R = 2.95\,m$). This constrains the total amount of material which can be put in to absorb hadronic showers. Therefore, an outer hadron calorimeter, or *tail*

catcher is placed outside the solenoid complementing the barrel one. Beyond $|\eta| = 3$, in the forward region, the forward hadron calorimeters, placed at $11.2\,m$ from the interaction point, extend the pseudorapidity range down to $|\eta| = 5.2$ using a Cerenkov-based radiation hard technology. Pions with energies of $150\,GeV$ and $300\,GeV$ were used to measure the response of the combined ECAL and HCAL system. The pion energy resolution obtained is:

$$\frac{\sigma(E)}{E} = \frac{138\%}{\sqrt{E}} \oplus 13\% \tag{2.1}$$

where E is in GeV.

2.1.2.4 Trigger and data acquisition

Trigger

The LHC provides proton-proton and heavy-ion collisions at high rates [1]. For the protons the beam crossing interval will be $25\,ns$ (now it is limited to $50\,ns$), corresponding to a frequency of crossing of $40\,MHz$. Depending on luminosity, several collisions occur at each crossing of the proton bunches (approximately 25 simultaneous *pp* collisions at the nominal design luminosity of $10^{34}\,cm^{-2}s^{-1}$). It is impossible to store and process the large amount of data associated with the resulting high number of events, the rate must be reduced. This task is performed by the *trigger system*, which is the beginning of the physics event selection process. The reduction takes place in two steps called *Level-1 Trigger* (L1) and *High-Level Trigger* (HLT).

The Level-1 trigger consists of custom-designed, largely programmable electronics.

The High Level Trigger is a software system implemented in a filter farm of about one thousand commercial processors. The rate reduction capability is designed to be about 10^6 for the combined L1 and HLT trigger. The design output rate limit of the L1 trigger is $100\,kHz$, which translate in practice to a calculated maximal output rate of $30\,kHz$, assuming a safety factor of three. The L1 trigger uses coarsely segmented data from the calorimeters and the muon system, while holding the high-resolution data in pipelined memories in the front-end electronics. The HLT has access to the complete read-out data and can therefore perform complex calculations similar to those made in the off-line analysis if required for specially interesting events. The HLT algorithms evolve with time and experience.

For reason of flexibility the L1 trigger hardware is implemented in FPGA technology where possible, but ASICs and programmable memory lookup tables (LUT) are also widely used where speed, density and radiation resistance requirements are important. The Trigger Supervisor, a software system, controls the configuration and operation of the trigger

components.
The L1 trigger has local, regional and global components. At the bottom end the Local trigger, also called Trigger Primitive Generators (TPG), is based on energy deposits in calorimeter trigger towers and track segments or hit patterns in muon chambers. Regional Triggers combine their information and use pattern logic to determine ranked and sorted trigger objects such as electron or muon candidates in limited spatial regions. The rank is determined as a function of energy or momentum and quality, which reflects the level of confidence attributed to the L1 parameter measurements, based on detailed knowledge of the detectors and trigger electronics and the amount of information available. The Global Calorimeter and Global Muon Triggers determine the highest rank calorimeter and muon object across the entire experiment and transfer them to the Global Trigger, the top entity of the Level-1 hierarchy. The latter takes the decision to reject an event or to accept it for further evaluation by the HLT. The decision is based on algorithm calculations and on the readiness of the sub detectors and the DAQ, which is determined by the Trigger Control System (TCS). The Level-1 Accept (L1A) decision is communicated to the sub detectors through the Timing, Trigger and Control (TTC) system. The L1 trigger has to analyse every bunch crossing. The latency of the L1 trigger, between a given bunch crossing and the distributions of the trigger decision to the detector front-end electronics is $3.2\,\mu s$. The processing must therefore be pipelined in order to enable an almost dead-time free operation. The L1 trigger electronics is housed partly on the detectors, partly in the underground control room located at a distance of approximately $90\,m$ from the experimental cavern.
The HLT is divided into the level 2 and 3 (L2 and L3) trigger steps. At L3 level typically the full tracker information is used. Due to the rate of the L1 trigger, more information can be processed for this trigger selection. Other selection and skimming are applied to reduce the rate in the L2 and L3 trigger steps.

Data acquisition

The CMS Trigger and DAQ system is designed to collect and analyse the detector information at the LHC bunch crossing frequency of $40\,MHz$. The rate of events to be recorded for offline processing and analysis is on the order of few $10^2\,Hz$. At the design luminosity of $10^{34}\,cm^{-2}s^{-1}$, the LHC rate of proton collisions will be around 25 per bunch crossing, producing approximately $1\,MByte$ of zero-suppressed data in the CMS read-out system.
The first level trigger is designed to reduce incoming average rate to a maximum of $100\,kHz$, by processing fast trigger information coming from the calorimeters and the muon chambers, and selecting events with interesting signatures. The DAQ system must sustain a maximum input rate of $100\,kHz$, for a data flow of $\approx 100\,GBytes/s$ coming from

approximately 650 data sources, and must provide enough computing power for a software filter system, the High Level Trigger (HLT), to reduce the rate stored events by a factor of 1000.
In CMS all events which pass the L1 trigger are sent to a computer farm (Event Filter) that performs physics selections, using faster version of the off-line reconstruction software, to filter events and reach the required output rate.
Each data source to the DAQ system is expected to deliver an average event fragment size of $\approx 2\,kByte$ (for the pp collision at the design luminosity). Sometimes two data sources are merged in order to achieve the nominal size. The various sub-detectors front-end system (FES) store continuously in $40\,MHz$ pipelined buffers. Upon arrival of a synchronous L1 trigger ($3.2\,\mu s$ of latency) via the Timing, Trigger and Control system (TTC), the corresponding data are extracted from the front-end buffers and pushed into the DAQ system by the Front-End Drivers (FEDs). The data from the FEDs are read into the Front-end Read-out Links (FRLs) that are able to merge data from two FEDs. The number of FRLs corresponding to the CMS read-out parameters is 458. In the baseline configuration there are 512 FRLs. These additional inputs are used for a combined operation with TOTEM experiment [4], and for inputs from local trigger units, among others. The sub-detector read-out FRL electronics are located in the underground electronics room (USC).

The event builder assembles the event fragments belonging to the same L1 from all FEDs into a complete event and transmit it to one Filter Unit (FU) in the Event Filter further processing. The event builder is implemented in two stages (referred to as FED-builder and TU-builder) and comprises a several number of components. The DAQ system can be deployed in up to 8 *slices*, each of which is a nearly autonomous system, capable of handling a $12.5\,kHz$ event rate. The event builder is also in charge of transporting the data from the underground to the surface (SCX), where the filter farm is located.
The system of acquisition includes back-pressure all the way from the filter farm through the event builder to the FEDs. Back-pressure from the down-stream event processing, or variations in the size and rate of events, may give rise to buffer overflows in the sub-detector's front-end electronics, which would result in data corruption and loss of synchronization. The Trigger-Throttling System (TTS) protects against these buffer overflows. It provides fast feedback from any of the sub-detector front-ends to the Global Trigger Processor (GTP) so that the trigger can be throttled before buffers overflow. During operation, trigger thresholds and pre-scales are optimized in order to fully utilize the available DAQ and HLT throughput capacity. Instantaneous fluctuations might lead to L1 trigger throttling and introduce dead-time. CMS has defined a *luminosity section* as a fixed period of time (set to 2^{20} LHC orbits, corresponding to $93\,s$), during which trigger thresholds and pre-scales are not changed. The GTP counts the live-time (in number of

bunch crossing) for each luminosity section and records them in the Conditions Database for later analysis.

The required computing power of the filter farm to allow the HLT algorithms to achieve the design factor of 1000 is substantial and corresponding to order of 1000 processing nodes. At the LHC luminosity of $2 \times 10^{33}\, cm^{-2}s^{-1}$ it is foreseen to operate at a maximum L1 rate of $50\, kHz$, corresponding to the 4 installed DAQ slices. It has been estimated that under these conditions the HLT algorithms will demand a mean processing time of around $50\, ms$ on a $3 - GHz$ Xeon CPU-core. This implies for the $50\, kHz$ DAQ system an equivalent of about 2500 CPU-cores must deployed for the HLT. After optimizing the trigger selection for the LHC design luminosity, the estimated required computing power is expected to be roughly twice as much for 8 DAQ slices, operating at a $100\, kHz$ L1 rate. For the first LHC run, the Event Filter is foreseen to comprise 720 PC-nodes (with two quad-core processors) for $50\, kHz$ operation. Based on initial experience and evaluation of candidate hardware, the additional filter farm nodes for $100\, kHz$ operation at design luminosity will be procured. The design of the DAQ system allows for this gradual expansion in event building rate and processing.

3

The tracker and muon systems

In this chapter I will discuss the inner tracker detector and the muon systems in the CMS experiment.
With the first collisions in $2009 - 2010$ the data collected gives an overview of the performance of the detector. The physics performance, the resolution in invariant masses and in the tracking reconstruction are important for a lot of analysis.

3.1 Overview

Designed to provide a precise and efficient measurement of the trajectories of charged particles coming from the collisions as well as a precise reconstruction of secondary vertex, the inner tracking system surrounds the interaction point for $5.8\,m$ length and $2.5\,m$ of diameter. The CMS solenoid provides a homogeneous magnetic field of $3.8\,T$ over the full volume of the tracker [1] (see chapter 2). With the design luminosity of LHC, $10^{34}\,cm^{-2}s^{-1}$, there will be about 1000 particle from more than 25 overlapping proton-proton interaction traversing the apparatus each bunch crossing, every $25\,ns$ at the design working frequency. Therefore a detector technology with high granularity and fast response is needed, such that the trajectories can be identified correctly and attributed to the correct bunch crossing. This features imply a high power density of the electronics on the detector that also require an efficient cooling system. This is against the goal to keep the minimum amount of material in order to limit multiple scattering, bremsstrahlung, photon conversion and nuclear interaction. The intense flux of particles will cause also severe radiation damage to the tracking system: the main challenge was to develop a device able to work in such a harsh environment for 10 years. These characteristic of granularity, speed and radiation hardness guide the choice to a silicon detector technology.
The tracker is made of a pixel detector with three barrel layers between $4.4\,cm$ and $10.2\,cm$ of radius and a silicon strip tracker with ten barrel detection layers extending the radius up to $1.1\,m$. Each of the system is completed by endcaps which consist of 2 disks in the

pixel detector and 3 + 9 disks in the strip tracker, on each side of the barrel, extending the region of acceptance of the tracker up to $|\eta| < 2.5$.
With $200\,m^2$ of active silicon area, the CMS tracker, is the largest silicon tracker ever built.
The construction of the CMS tracker, composed of 1440 pixel and 15148 strip detector modules, required the development of production methods and quality control procedures that are new to the field of particle physics detectors. A large factor of the testing and of the construction of the device was made by the Pisa group, at INFN laboratory.

3.2 Layout

Three cylindrical layers of hybrid pixel detector modules surround the interaction point at different radii: $4.4\,cm$, $7.3\,cm$ and $10.2\,cm$. The pixel detector delivers three high precision space points on each charged particle trajectory. In total the pixel detector covers an area of about $1\,m^2$ and has 66 million pixels.
The region beyond, between $20\,cm$ and $116\,cm$, is occupied by the silicon strip tracker. It is made by three different subsystems.

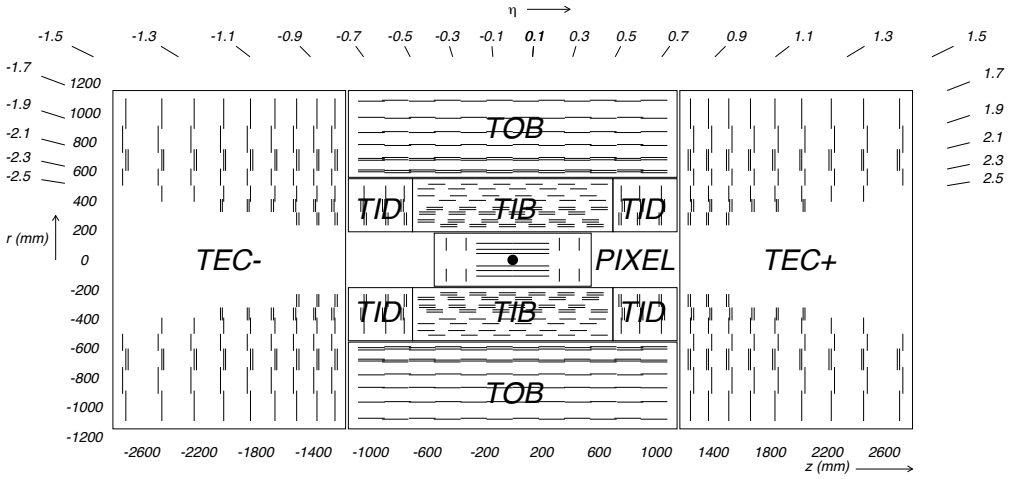

Figure 3.1: Schematic cross section of CMS tracker

To extend the radius towards $55\,cm$ there is the tracker inner barrel and disks (TIB/TID) composed of 4 barrel layers, supplemented by 3 disks at each end. (Fig. 3.1) TIB and TID makes up to $4\,r-\phi$ measurements on a trajectory using $320\,\mu m$ thick silicon micro-strip sensors with their strips parallel to the beam axis in the barrel and radial on the disk. The strip pitch is $80\,\mu m$ on layers 1 and 2 and $120\,\mu m$ on layers 3 and 4 in the TIB, leading to a single point resolution of $23\,\mu m$ and $35\,\mu m$, respectively. In the TID the mean pitch

varies between $100\,\mu m$ and $141\,\mu m$. The TIB/TID is surrounded by the Tracker Outer Barrel (TOB): it has an outer radius of $116\,cm$ and consists of 6 barrel layers of $500\,\mu m$ of thick micro-strip sensors with strip pitches of $183\,\mu m$ on the first 4 layers and $122\,\mu m$ on layers 5 and 6. It adds another $6\,r-\phi$ measurements with single point resolutions of $53\,\mu m$ and $35\,\mu m$. The TOB extends in z up to $\pm\,118\,cm$. Beyond this range the Tracker End Caps (TEC+ and TEC- depends on the location in the z axis) cover up the region $124\,cm < |z| < 282\,cm$ and $22.5\,cm < |r| < 113.5\,cm$. Each of the TEC is made by 9 disks, bringing to 7 the rings of silicon micro-strip detectors ($320\,\mu m$ thick on the inner 4 rings, $500\,\mu m$ thick on rings $5-7$) with radial strips of $97\,\mu m$ to $184\,\mu m$ average pitch.
Added to these, the modules in the first two layers and rings, respectively, of TIB, TID, and TOB as well as rings 1, 2, and 5 of the TECs carry a second micro-strip detector module which is mounted back-to-back with a stereo angle of $100\,mrad$ in order to provide a measurement of the second co-ordinate (z in the barrel and r on the disks). The reached single point resolution of this measurement is $230\,\mu m$ and $530\,\mu m$ in TIB and TOB, respectively, and varies with pitch in TID and TEC. This tracker layout ensures at minimum ~ 9 hits in the silicon strip tracker in the full range of $|\eta| < 2.4$ with at least ~ 4 of them being two-dimensional measurements. The acceptance of the tracker extends up to $|\eta| \sim 2.5$.
The CMS silicon strip tracker has a total of 9.3 millions strips and $198\,m^2$ of active silicon area.
The basic performance expected for the tracking detector is a transverse momentum resolution of $\sim 1-2\%$ for muons of $p_T \sim 100\,GeV$, an impact parameter resolution of about $10-20\,\mu m$ for tracks with a $p_T \sim 10-20\,GeV$ and the ability to reconstruct tracks in hadronic jets with an efficiency of $\sim 85-90\%$ and a fake rate lower than few percent.

3.2.1 The pixel detector

The pixel system is the part of the tracking system that is closest to the interaction region. It contributes precise tracking points in the $r-\phi$ angles and z axis, and therefore is responsible for a small impact parameter resolution that is important for good secondary vertex reconstruction.
With a pixel cell size of $100 \times 150\,\mu m^2$ emphasis has been put on achieving similar track resolution in both $r-\phi$ and z direction. Through this a 3D vertex reconstruction in space is possible, which is important for secondary vertices with low track multiplicity. The pixel system has a zero-suppressed read out scheme with analogue pulse height read-out. This improves the position resolution due to charge sharing and helps to separate signal and noise hits as well as to identify large hit clusters from overlapping tracks.
Covering a pseudorapidity range $|\eta| < 2.5$ matching the acceptance of central tracker, the

pixel detector is essential for the reconstruction and high level triggering. It consists of three barrel layers (BPix) with two endcaps disks (FPix). BPix layers are located at mean radii of $4.4\,cm$, $7.3\,cm$ and $10.2\,cm$. FPix disks extends from ~ 6 to $15\,cm$ in radius and are placed on each side at $z = \pm 34.5\,cm$ and $z = \pm 46.5\,cm$. BPix (FPix) has 48 millions (18 millions) pixel covering an area of $0.78(0.28)\,m^2$.

The arrangement of the 3 barrel layers and the forward pixel disks on each side gives 3 tracking points over almost the full η-range. In the high pseudorapidity region the 2 disk points are combined with the lowest possible radius point from the $4.4\,cm$ barrel layer.

The nearness to the interaction region also implies a very high track rate and particle flow that require a radiation hardness design. For the sensors this guide to an n^+ pixel on $n-$substrate detector design that allows partial depleted operation even at very high particle fluencies. For the barrel layer the drift of the electrons to the collecting pixel implant is orthogonal to the magnetic field of CMS. The resulting Lorentz drift leads to charge spreading of the collected signal charge over more than one pixel. With the analog pulse height being read out a charge interpolation allows to achieve a spatial resolution of $15 - 20\,\mu m$. The forward detectors are tilted at $20°$ in a turbine-like geometry to include charge sharing.

The charge sharing is mainly due to the $\overrightarrow{E} \times \overrightarrow{B}$ drift effect of the particle. In particular the width of the charge in the readout chip depends on the p_T of the particle. The width of the signal in the readout chip is also called *cluster-width*. A position resolution of approximately $15\,\mu m$ in both directions can be reached with charge-sharing between neighbouring pixels. The reduction in the depletion depth or the increase in bias voltage will lead to a reduction of charge-sharing and therefore a degradation of the spatial resolution with radiation damage. Allowing a replacement of the innermost layers, the mechanics and the cabling of the pixel system has been designed to permit access if needed.

At full LHC luminosity the expectation working time for the detector is at most 2 years.

The mechanics of the 3 barrel layer as well as the forward disks are divided into a left and a right half. This is necessary to allow the installation along the beam pipe and to pass beyond the beam pipe support wires at $z \pm 1632\,mm$. The 6 individual mechanical pieces are referenced to each other through precisely machined rails inside the TIB cylinder. Power, cooling, the optical controls as well as the optical read-out lines are linked to the detector through supply tube shells. For the barrel pixel system the supply tubes have a flexible connection that needs to bend by a few degrees during insertion following the slightly curved rails around the beam pipe support ring. The pixel system has been inserted as the last sub-detector of CMS after the silicon strip tracker installation and after the central section of the beam pipe has been installed and baked out.

3.2.2 The silicon strip

The sensors in the strip tracker are single sided $p-on-n$ type silicon micro-strip sensors. [5].

They have been manufactured on 6 inchess wafers in a standard planar process, leading to significant cost reduction per unit area when compared to the more traditional 4 inches ones.

The base material in n doped float zone silicon with $\langle 100 \rangle$ crystal orientation. This crystal orientation was preferred over the more common $\langle 111 \rangle$ one because measurements have shown that the built-up surface charge on $\langle 100 \rangle$ wafers due to irradiation is much smaller and consequently irradiation causes less inter-strip capacitance increase on this material. In TIB/TID and on the inner 4 rings of the TECs, thin sensors of $(320 \pm 20)\mu m$ wafer thickness are used, with substrate resistivity of $\rho = 1.55 - 3.25\, k\Omega cm$. TOB and the outer 3 rings of the TECs are equipped with thicker sensors of $(500 \pm 20)\mu m$, with substrate resistivity of $\rho = 4 - 8\, k\Omega cm$. These sensors, due to the single sided processing, show a significant bow, which is required to be less than $100\, \mu m$.

On the back side of the wafers, covered by aluminium, a uniform n^+ implantation forms an ohmic contact which is connected to positive charge voltage up to about $500\, V$. Those few sensors which are penetrated by beam of the laser alignment system feature a $10\, mm$ hole in the back side metallization, as well as an anti-reflective coating in order achieve transmission through up to four sensors with a sufficient signal on a fifth one.

On the front side the strip shaped diodes are formed by p^+ implantation into the n type bulk. The bulk material will undergo type inversion and change to p type, due to the radiation damage to the crystal lattice. The pn junction, at this point, moves from the strip side of the wafer to the rear side contact. Each implanted strip is covered by aluminium strip from which it is electrically isolated by means of a silicon oxide and nitride multilayer. This integrated capacitor allows for AC coupling of the signals from the strips to the read-out electronics chain, which is thus protected from the high leakage currents after irradiation. Each metal strip has two bond pads on each end, which are used to make a wire bond connection to the read-out chip and in case of a daisy chained sensors to make a wire bod connection between the two sensors in one detector module. For testing purposes there was also a DC pad connected to the p^+ implant. Each strip implant is connected via a $(1.5 \pm 0.5)\, M\Omega$ polysilicon bias resistor to a p^+ bias ring which encloses the strip region and also defines the active area of the sensor.

For all the sensors in the CMS strip tracker, the ratio of p^+ implant width over strip pitch is $w/p = 0.25$, leading to a uniform total strip capacitance per unit length of about $1.2\, pF/cm$ across all sensor geometries. The actual w/p value was chosen in order to minimize the strip capacitance while still maintaining a good high voltage behaviour of

the sensors. The aluminium strip feature a metal overhang of 4 to 8 μm on each side of the strip which pushes the high field region into the silicon oxide where the breakdown voltage is much higher, leading to stable high voltage operation. The bias ring is surrounded by a floating guard ring p^+ implant, for the same reason. It gradually degrades the electric field between the n^+ implant at the cut edge of the sensor and the bias ring, which are at a backplane potential (high voltage) and ground.
In order to equip all regions in the CMS tracker, 15 different sensor geometries are needed: two rectangular sensor types each for TIB and TOB, and 11 wedge-shaped sensor types for TEC and TID. They have either 512 or 768 strips, reflecting the read-out modularity of 256 channels (two 128−channels front-end chips multipixeled to one read-out channel). Since the sensors are fabricated on 6 inches wafers, they can be made rather large. Typical dimensions are $(6 \times 12)\, cm^2$ and $(10 \times 9)\, cm^2$ in the inner and outer barrel. The total number of silicon sensors in the strip tracker is 24244, making up a total active area of $198\, cm^2$ with about 9.3 million of strips.

Silicon read-out system

The signals from the silicon sensors are amplified, shaped and stored by a custom integrated circuit, the APV25. Upon a first level trigger decision the analogue signals of all channels are multiplexed and transmitted via optical fibres to Front End Driver (FED) boards in the service cavern where the analogue to digital conversion takes place. This read-out scheme brings the full analogue information to a place where it can be used for accurate pedestal and common mode subtraction as well as data sparsification. Clock, trigger and control signals are transmitted by optical links. A schematic view of the silicon strip tracker read-out scheme is in the figure 3.2.

This analogue read-out scheme was chosen for several reasons: optimal spatial resolution from charge sharing, operational robustness and ease monitoring due to the availability of the full analogue signal, robustness against possible common mode noise, less custom radiation hard electronics and reduced material budget as the analogue to digital conversion and its power needs are shifted out of the tracker volume.

3.3 First operations

The first pp collisions happened at energies of $\sqrt{s} = 900\, GeV$ and $2360\, GeV$, in December 2009, at relatively low luminosity when the CMS readout was triggered by the beam scintillator counters placed close to the beam line to collect minimum-bias collision events.
These data, together with the cosmic runs, provided the first commissioning of the track-

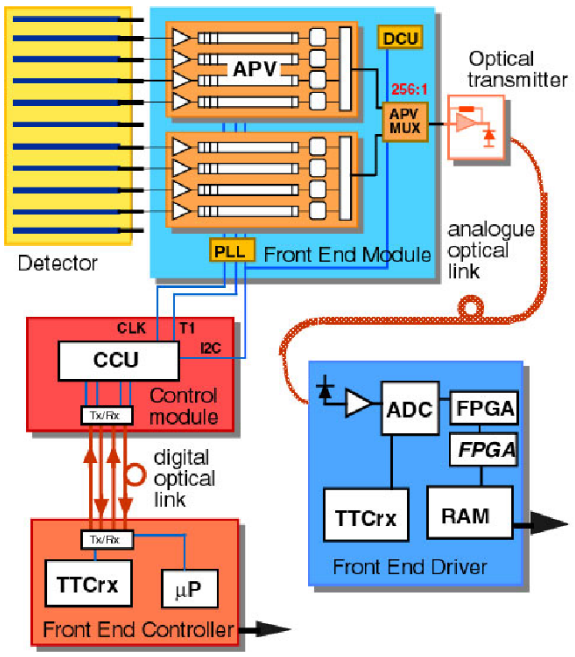

Figure 3.2: Read-out scheme of the CMS tracker.

ing detectors and allowed to reconstruct basic physics object as a demonstration of the performance [6], [7].

3.3.1 Tracker alignment

The good hit position resolution of the silicon tracker, ranging from about 10 to 30 μm requires a knowledge of the position of the 15148 strips and of the 1440 pixel sensors with an equal or comparable accuracy. The results of the optical surveys performed at each step of the tracker construction are a very useful starting point but do not provide the required accuracy and cannot correct the time dependent changes of the geometry which occurred after the installation of the tracker.
Therefore alignment algorithms used for the final determination of the sensor positions and orientations are based on the track reconstruction. There are two algorithms developed for CMS:

- *Millipede II* [8]: performs a global minimization of the χ^2 including also the track parameters which are optimized together with the sensor position parameters. To obtain that the track parameters dependence are linearised and *ad hoc* track model is used respecting the standard reconstruction. The sensors alignment parameters are determined by solving a matrix equation of the order of 10^5 elements.

- *Hit and Impact Points* (HIP)[9]: performs a local minimization of the χ^2 with respect of the position of each sensor; the parameters of the track used to compute the

residuals are fixed and determined by excluding the sensor under study from the track fit. The correlation among the alignment parameters of different modules and the track parameters are taken into account, effectively, by iterating the procedure several times and using the alignment parameters of the previous iteration to re-reconstruct the tracks used in the χ^2 computation. The HIP algorithm allows to include the results of the optical surveys as constraints in the χ^2 minimization.

Finally the two alignment algorithms are applied sequentially, using the alignment parameters determined by the first as starting point for the second, and the procedure is applied firstly on large scale substructures and finally at the sensor level.
The alignment parameters have been determined three times: with cosmic muon tracks in 2008 and 2009, and with about 1.5 million of cosmic tracks ($p > 4\,GeV$) and 1.7 million collision tracks ($p > 3\,GeV$). The complementarity of the cosmic and the collision tracks samples allowed to reach a good accuracy both in the barrel and in the endcaps of the tracker.

3.3.2 Physics performance

The first collisions recorded by CMS at LHC represented an important step for the commissioning of the tracking detector and of the track reconstruction.
Nevertheless they have been extremely useful to access the basic features of the performance of the tracker and of the reconstruction among which: the synchronization of the tracker readout the LHC beam, the measurement of the actual hit occupancy, its comparison with the simulation, and the performance of the track reconstruction pattern recognition with the actual occupancy. The full operation, readout and reconstruction chain, worked smoothly and as expected and the system proved to be robust also with respect to unexpected high multiplicity beam background events. The tracking detector data also has been very useful as a first feedback for the tuning of the simulation on non-perturbative QCD process.
All the measured observables have been compared to the simulation tuned to reproduce the realistic detector conditions with the disconnected channels (98.3% active channels in pixel tracker and 98.1% active channels in strip one) and alignment accuracy.

3.3.2.1 Track Reconstruction

Tracks are reconstructed in four steps in CMS.
The first is the *seeding step* when hit triplets or pairs (plus the beam spot constrain) from the pixel tracker or the inner layers of the strip tracker are selected and used as a candidate.

The second is the *pattern recognition step* when the candidates are propagated using a Kalman filter technique [10] to find new compatible hits and the track parameters are updated. In this passage there is the possibility to reject the track with not enough hits. The third step is the *final track fit* when the track parameters are estimated combining all the associated hits. In this step hits can be rejected if they look incompatible to the fitted track.
Finally at the tracks are given a quality flag based on the set of cuts sensitive to fake tracks and based on track normalized χ^2, track compatibility with interaction region, track length and number of missed hits. The tracks which pass the tightest selection are classified as *high purity* tracks while those that do not fulfil the loosest cuts are discarded. All the previous steps are made six times: at each iteration the hits associated to the high purity tracks are discarded and the seeding and the pattern recognition steps are performed using the remaining hits. This permit, at each iteration, to have looser cuts at the seeding step and at the final track selection step, thanks to the reduced combinatorial background. In addition a dedicated track and primary vertex reconstruction based only on pixel tracker hits is performed to provide a set of primary vertices which can be used for the full track reconstruction and also in the High Level Trigger algorithms which are run online, thanks to the speed of this simple reconstruction.

In figure 3.3 the distribution of few observables obtained at $7\,TeV$ are compared to the predictions obtained with $PYTHIA$ generator with the default tuning and a full GEANT-based simulation of the CMS detector.
The good agreement of the observation assures that the track reconstruction and in particular the pattern recognition works as expected also with the actual hit occupancy and there is no striking evidence of inefficiencies or strange fake rates. The distribution in pseudorapidity of the track and azimuthal angle and the number of hits per track prove that the simulation is able to reproduce tiny details thanks to a detailed description of the tracker geometry and of the dead channels.

3.3.2.2 Distributions of invariant masses

The subsequent step in the commissioning of the tracking detector and of the track reconstruction with the first collisions has been the reconstruction of the invariant masses of tracks from unstable particle resonance decays. The invariant mass distributions with the presence of narrow peaks provide references which can be used to compare momentum calibration and resolution between real data and simulation.
With the data collected in 2009 and 2010 only low mass particle and resonance decays have been produced with a sufficient statistics and in a transverse momentum range of a few GeV or less. The comparison with the simulation provides a valid tool to check the

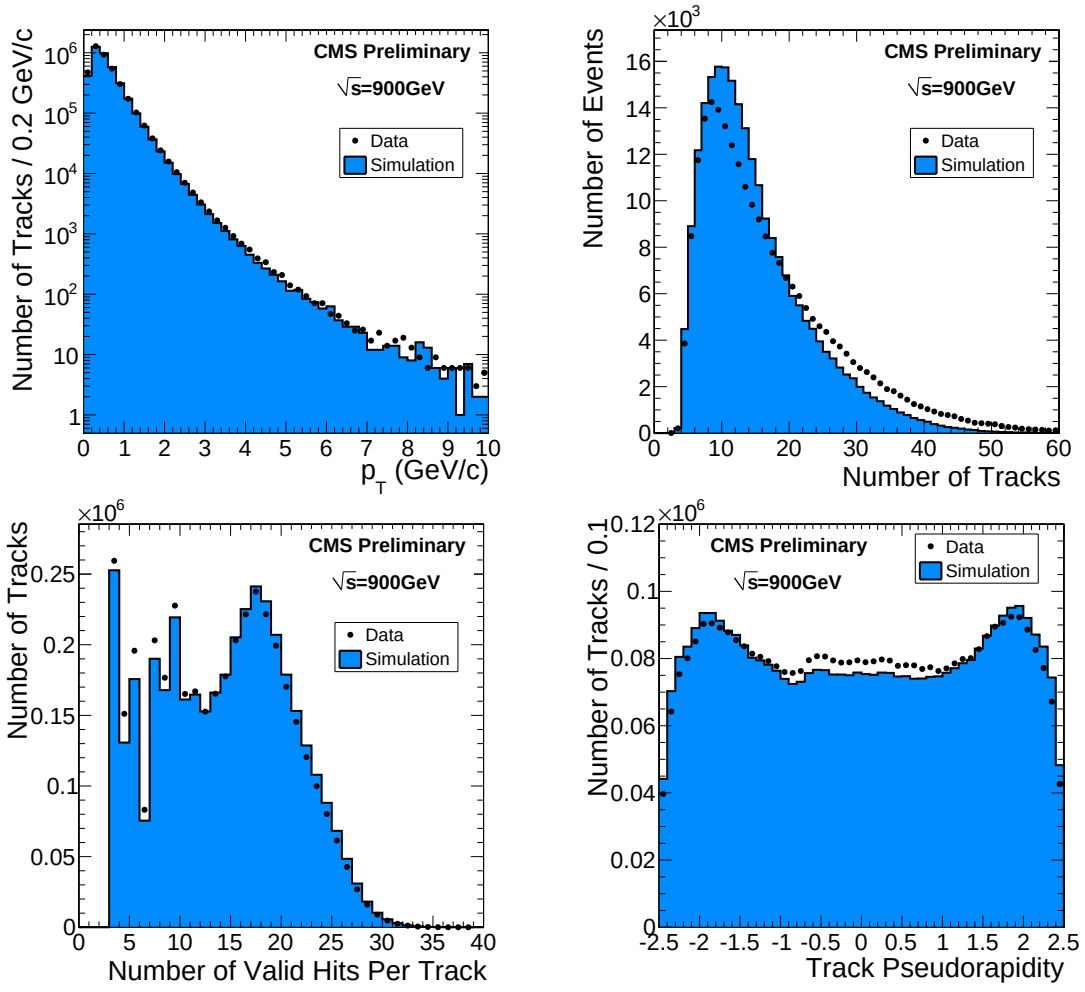

Figure 3.3: Comparison of data (points) and simulation (blu).

simulation of the multiple scattering and of the energy loss due to the detector material, which affect mostly the low momentum particle. Furthermore the relative contribution between the signal region and the combinatorial background is used to check the simulation of the background itself and to give feedback for the tuning of the simulation of the production yield of these particles.

$K_s^0 \to \pi^+\pi^-$ and $\Lambda^0 \to p\pi^-$ decay (V^0) invariant mass distributions have been produced with opposite charge tracks: they are required to be of good quality and to have a transverse impact parameter not compatible with the interaction region within 0.5σ. These pairs of tracks are fitted to a common vertex and if the fit is successful and with a good χ^2 the pair is kept if the significance of the transverse distance of the vertex from the interaction region is bigger than 15. In the Λ^0 decay, the particle with the largest momentum is given the mass of the proton, see figure 3.4.

In figure 3.5 there are the invariant mass distribution of the K_s^0 and Λ^0 decay candidates fitted with a double Gaussian function: the resolution obtained from the average of the

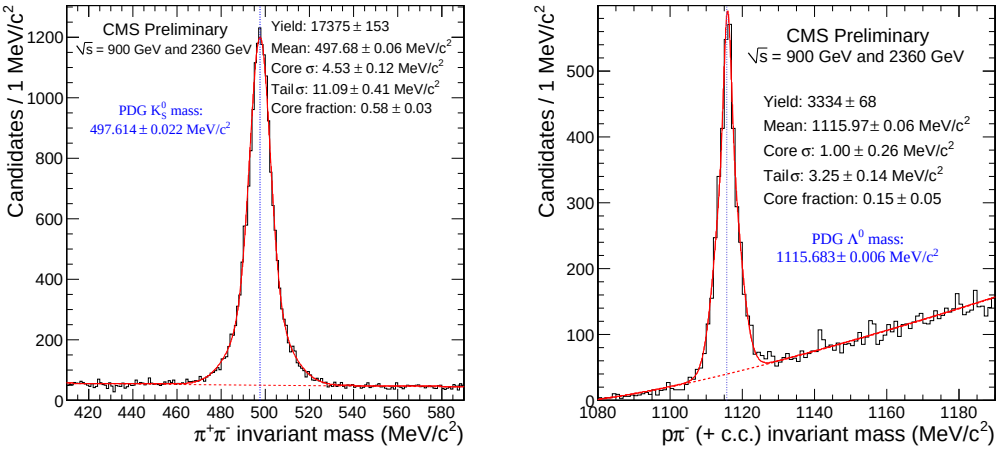

Figure 3.4: Left: $K^0_s \to \pi^+\pi^-$, right $\Lambda^0 \to p\pi^-$ candidate invariant mass distributions obtained with 900 GeV and 2360 GeV collision events

two Gaussian resolutions are 8.0 MeV for K^0_s and 3.0 MeV for Λ^0, in good agreement with the MC predictions: 7.6 MeV and 3.0 MeV. A similar agreement between MC and data is seen in the decays of the Ξ^- and $K^*(892)$. The data collected at the beginning of 2010 run data, about 10 million of minimum bias events, also have been used to search for D meson decays, like $D^* \to D^0\pi \to K\pi\pi$ decay chain has been studied by pairing opposite charge tracks with $p_T > 600\,MeV$ and which form a good vertex; if the invariant mass is close to the D^0 mass less than 25 MeV, a third track with $p_T > 250\,MeV$ is combined to form the D^* candidate.

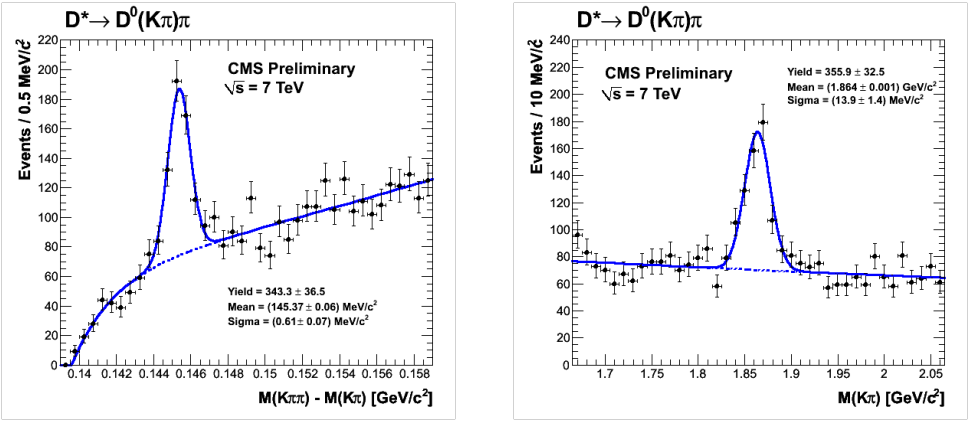

Figure 3.5: Left: Distribution of the invariant mass M($K\pi\pi$)-M($K\pi$) difference; Right: the Kπ invariant mass (right) obtained with 7 TeV collision events

Due to the large amount of collected data the invariant mass distribution are also used for qualitative estimate and calibration of the tracking performance.

There is not a single method of measuring track reconstruction efficiency that cover all the possible environments, kinematic ranges and systematic effects. It is important to

use different methods to account for different event occupancies, particle momenta and sources of systematic uncertainty. A track-embedding method is used to measure absolute tracking efficiency for muons and pions for transverse momenta above $500\,MeV/c$.
The tracking efficiency has been studied by comparing the ratio of observed $D^* \to D^0\pi \to (K\pi\pi\pi)\pi$ to $D^* \to D^0\pi \to (K\pi)\pi$ decays and applying the tag-and-probe algorithm to the $J/\psi \to \mu\mu$ decay [11], where the tag is a fully reconstructed muon and the probe is a muon reconstructed only in the CMS muon detectors and its reconstruction in the inner tracking detector is probed, see section 3.4. The reconstructing D^0 must has some kinematic properties, like a certain minimum transverse momentum and a minimum track vertex probability, in order to exclude bad candidates.
Another important point is that the tracking efficiency for hadron is expected to be different than that for muons, due to decays and nuclear interactions with the material of the detector [12]. The relative efficiency of reconstructing pions tracks in data and simulation can be determined by measuring the ratio of neutral charm meson decays to final states of four or two charged particles.
A way to study the momentum scale calibration and resolution uses the K_s^0 distribution of mass, together with the $J/\psi \to \mu\mu$ decays.

3.4 The Muon system

The detection of muon is a powerful tool for reconstructing interesting processes over the high background rate expected at the LHC luminosity.
One example is the Standard Model Higgs boson decay into ZZ or ZZ^* into four leptons: the *gold plated* case, when all the leptons are muons. The decays in four muons have the best mass resolution due to the less radiative losses in the tracker material with respect to the electrons. This example, and others from SUSY models, emphasize the discovery potential of muon final states and the necessity for the wide angular coverage for the detection of them.
The detection of muons is of central importance to CMS: precise and robust muon measurement was a central theme since the early design stage. The system has three important functions: muon identification, momentum measurement and triggering the event.
Good muon momentum resolution and trigger capability are enabled by the high field of the solenoidal magnet and its flux-return yoke. The last one is also a hadron absorber for the identification of muons.

The CMS muon system is designed to have the capability of reconstructing the charge and the momentum of the muons over the entire kinematic range of the LHC. CMS uses 3 types for the muon identification [13]. Due to the shape of the solenoidal magnet, the muon system was driven to have a cylindrical barrel section and 2 planar endcap regions.

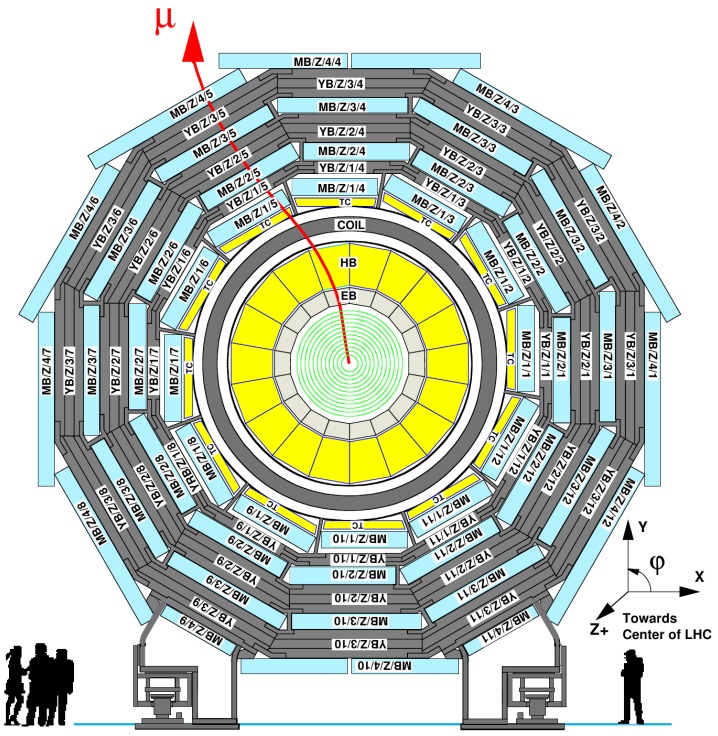

Figure 3.6: Layout of the CMS barrel muon DT chamber in one of the wheels. The chambers in each wheel are identical with the exception of wheels -1 and 1 where the presence of cryogenic chimneys for the magnet shortens the chambers into 2 sectors. In sector 4, at the top, and 10, at the bottom, the $MB4$ chambers are cut in half to simplify the mechanical assembly and the global chamber layout.

The entire system consist of about $25000\,m^2$ of detection planes, so the muon chambers have to be cheap, reliable and robust (figure 3.6).

In the barrel region, where the neutron-induced background is small the muon rate is low and the $4\,T$ magnetic field is uniform and mostly contained in the steel yoke, drift chambers with standard rectangular drift cells are used. The barrel drift tube (DT) chambers cover the pseudorapidity region $|\eta| < 1.2$ and are organized into 4 stations interspersed among the layers of the flux return plates. Each of the first 3 stations contains 8 chambers, in two groups of 4, which measure the muon coordinate in the $r-\phi$ bending plane, and the 4 chambers which provide a measurement in the z direction, along the beam line. The last station, the fourth, does not contain the $z-$measurement planes. The 2 sets of 4 chambers in each station are separated as much as possible to achieve the best angular resolution. The drift cells of each chamber are offset by a half-cell width with respect to their neighbour to eliminate dead spots in the efficiency. This configuration also provides a convenient way to measure the muon time with excellent time resolution, using simple meantimer circuits, for efficient, standalone bunch crossing identification. The number of chambers in each station and their orientation are chosen to provide good efficiency for

linking together muon hits from different stations into a single muon track and for rejecting background hits.

The 2 endcap regions of CMS receive an higher muon rate and the background levels are high and the magnetic field is large and non-uniform. To manage this the muon system uses the cathode strip chambers (CSC). Fast response time, fine segmentation and radiation hardness permit the CSC to work between $|\eta|$ values of 0.9 and 2.4. There are 4 CSC stations in each endcap, with chambers positioned perpendicular to the beam line and interspersed between the flux return plates. The cathode strips of each chamber run radially outward and provide a precision measurement in the $r - \phi$ bending plane. The anode wires run approximately perpendicular to the strips and are also read out in order to provide measurement of η and the beam-crossing time of a muon. Each $6-$layer CSC provides robust pattern recognition for rejection of non-muon backgrounds and efficient matching of hits to those in other stations and to the inner tracker.

The muon detector elements cover the full pseudorapidity range $|\eta| < 2.4$ with no gaps in acceptance, muon identification is ensured over the interval corresponding to $10^\circ < \theta < 170^\circ$. Off-line reconstruction efficiency of simulated single-muon samples is typically $95 - 99\%$ except in the regions around $|\eta| = 0.25$ and 0.8 (the regions between 2 DT wheels) and $|\eta| = 1.2$ (the transition region between the DT and the CSC system) where the efficiency drops. Negligible punch through reaches the system due to the amount of material in front of the muon system, which exceeds 16 radiation lengths.

The offline momentum resolution of the standalone muon system is about 9% for small values of η and p for transverse momentum up to $200\,GeV$, due to the multiple scattering in the detector before the muon station. At $1\,TeV$ the standalone momentum resolution varies between 15% and 40%, depending on $|\eta|$. A global momentum fit using also the inner tracker improves the momentum resolution by an order of magnitude at low momentum. At high momentum ($1\,TeV$) both detector parts together yield a momentum resolution of about 5%. The muon system and the inner tracker provide independent muon momentum measurements, this redundancy enhances fault finding and permits cross-checking between the systems. A crucial characteristic of the DT and the CSC systems is that they can each trigger on the p_T of muons with good efficiency and high background suppression, independent from the rest of the detector. The Level-1 trigger p_T resolution, at the threshold, is about 15% in the barrel and 25% in the endcap.

Due to the uncertainty in the eventual background rates and in the ability of the muon system to measure the correct beam-crossing time when the LHC reaches full luminosity a complementary dedicated trigger system consisting of resistive plate chambers (RPC) was added in the barrel and in the endcap regions. The RPCs are double-gap chambers operated in avalanche mode to ensure good operation at high rates. They produce a fast

response with good time resolution but coarser position resolution than the DTs or CSCs. They also help to resolve ambiguities in attempting to make tracks multiple hits in chambers.

Six layers of RPCs are present in the barrel muon system, 2 in each of the first 2 stations and 1 in each of the last 2 stations. The redundancy in the first 2 stations allows the trigger algorithm to work even for low-p_T tracks that may stop before reaching the outer 2 stations. In the endcap region there is a plane of RPCs in each of the first 3 stations in order for the trigger to use the coincidences between stations to reduce background and to improve the time resolution for bunch crossing identification, and to achieve a good p_T resolution.

A sophisticated alignment system measures the positions of the muon detectors with respect to each other and to the inner tracker, in order to optimize the muon momentum resolution. An sketch of the layout and a display collision is given in figure 3.7

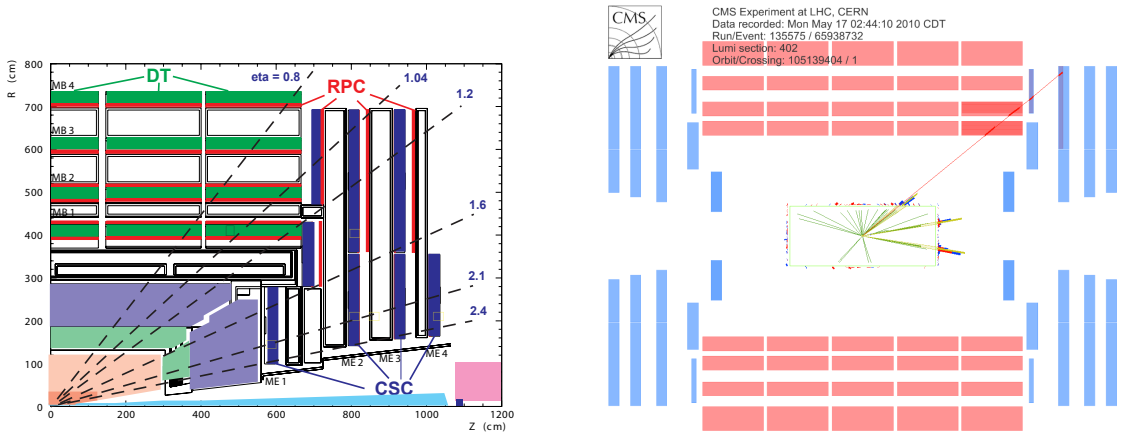

(a) (b)

Figure 3.7: Layout of the one quadrant of the CMS, 3.7(a), and a display collision event with a muon crossing the DT and the CSC chambers in the overlap region between barrel and endcap, 3.7(b)

3.4.1 Physics performance

Muon efficiency with tag-and-probe method on dimuon resonance

In CMS there are several kind of "muons", with different purities, which could be used for different analysis. The tracks reconstruction in CMS, for the *pp* collisions, is made independently in the silicon tracker and in the muon system. The first case is called a *tracker track* and the second case is called a *standalone-muon track*. The reconstruction has two approaches:

- *Global Muon reconstruction*, outside-in: starting from a standalone muon in the muon system, a matching tracker track is found and a *global-muon track* is fitted combining hits from the tracker track and standalone-muon track. At large transverse momenta (above $200\,GeV/c$), the global muon fit can improve the momentum resolution compared to the tracker-only fit.

- *Tracker Muon reconstruction*, inside-out: all tracker tracks with $p_T > 0.5\,GeV/c$ and $p > 2.5\,GeV/c$ are considered as possible muon candidates and are extrapolated to the muon system, taking into account the expected energy loss and the uncertainty due to multiple scattering. If at least one muon segment (such a short track stub made of DT or CSC hits) matches the extrapolated track in position, the corresponding tracker track is qualified as a *tracker-muon track*. At low momentum ($\sim p < 5\,GeV/c$) this approach is more efficient than the global muon one, since it requires only a single muon segment in the muon system, while global muon reconstruction typically becomes efficient with two or more segments.

- *Standalone-muon track only*: this occurs for $\sim 1\%$ of muons from collisions, thanks to the higher tracking efficiency. The acceptance of this type of muon track for cosmic ray muons is a factor $10^2 - 10^3$ less favourable than for the previous muon categories.

In my analysis (see chapter 5) the events are selected with two identified muon candidates, tracker muon or global muon.
Further selection can be made on the muon coming from these algorithms.
A *soft muon* is selected requiring the candidate to be a tracker muon, with the additional requirement that a segment is matched in both x and y coordinates with the extrapolated tracker track [14]. This additional requirement (and others) is optimized for low p_T muons ($< 10\,GeV/c$). A *tight muon* is reconstructed outside as a Global Muon (starting from a standalone muon in the muon system and fitted with the matching track found in the tracker: finally the global muon track is fitted combining these two informations) with other additional requirements, e.g. the minimum χ^2 and the muon chamber hits. A *particle flow muon* combine the information from all the sub-detectors to identify and reconstruct individually muon. This selection has been optimized to identify muons in jets, with high efficiency.
From the figure 3.9 it is possible to see that the plateau for the soft muons and the particle flows muons is reached at $p_T \sim 4(6)\,GeV/c$ in the barrel (endcap), while for the tight muon is reached at $\sim 10\,GeV/c$ in both regions.
The efficiencies for the prompt muon can be evaluated using the "tag-and-probe" technique to muon from the decays of J/ψ resonance. With this technique it is possible to obtain

almost unbiased estimates of the efficiencies of the different stages of muon trigger and off-line reconstruction. The events are selected with strict selection requirements on one muon (*tag*), and with a more relaxed selection on the other muon (the *probe*), the selection applied to the probe muon does not bias the efficiency that one wants to measure. The ratio of the probe muons which passes the selection under study gives an estimates of its efficiency.

When measuring muon identification efficiencies with this technique, the probes are tracks reconstructed using only the inner tracker, so there is no bias from the muon sub detectors. The efficiency to reconstruct a muon in the inner track has been measured separately and found to be larger than 99% in the whole tracker acceptance, in good agreement with the expectations from the simulations. See references [12] [15] for more informations.

In the muon identification measurement it is important to subtract the combinatorial background of tag-probe pairs not coming from the resonance under study, where the probe is usually a charged hadron. This subtraction is done by performing a simultaneous fit to the invariant mass spectra for passing and failing probes with identical signal shape and appropriate background shapes: the efficiency is computed from the normalizations of the signal shape in the two spectra, see figure 3.8(c) for the result.

For the J/ψ events, combinatorial backgrounds from the tracks in the event are generally high, making the background subtraction procedure challenging at low p_T. A powerful way to reduce this background is to require that the candidate probe muon has the signature of a minimum-ionizing-particle (MIP) in the calorimeter, see figure 3.8(a) . The reduction of the background is about a factor three without using any information from the muon system. Simulation studies show that in this low p_T range, the tag-and-probe efficiencies estimated with the MIP requirement are systematically $1-2\%$[1] higher than without the MIP requirement. See figure 3.8 for the complete results, with a simulated sample of $\sim 200\, nb^{-1}$.

In certain kinematic configurations, the muons from the J/ψ can be close to each other in the muon sub-detector. This introduce unwanted correlations in the measurement, and can result in inefficiencies for some muon identification algorithms. Unbiased measurement of single muon efficiencies can be obtained with a separation criteria applied to the tag-and-probe pairs: the extrapolated impact points of the two muon tracks on the muon detector must have an angular separation of $\Delta R > 0.5$[2].

In the figure 3.9 it is shown the muon identification efficiency given that a tracker track (see above for the definition) exists as measured from $J/\psi \to \mu^+\mu^-$ and $Z \to \mu^+\mu^-$ events. The results on the data are collected in the 2010 LHC run are compared with

[1] absolute difference in efficiency

[2] $\Delta R = \sqrt{(\Delta\phi)^2 + (\Delta\eta)^2}$

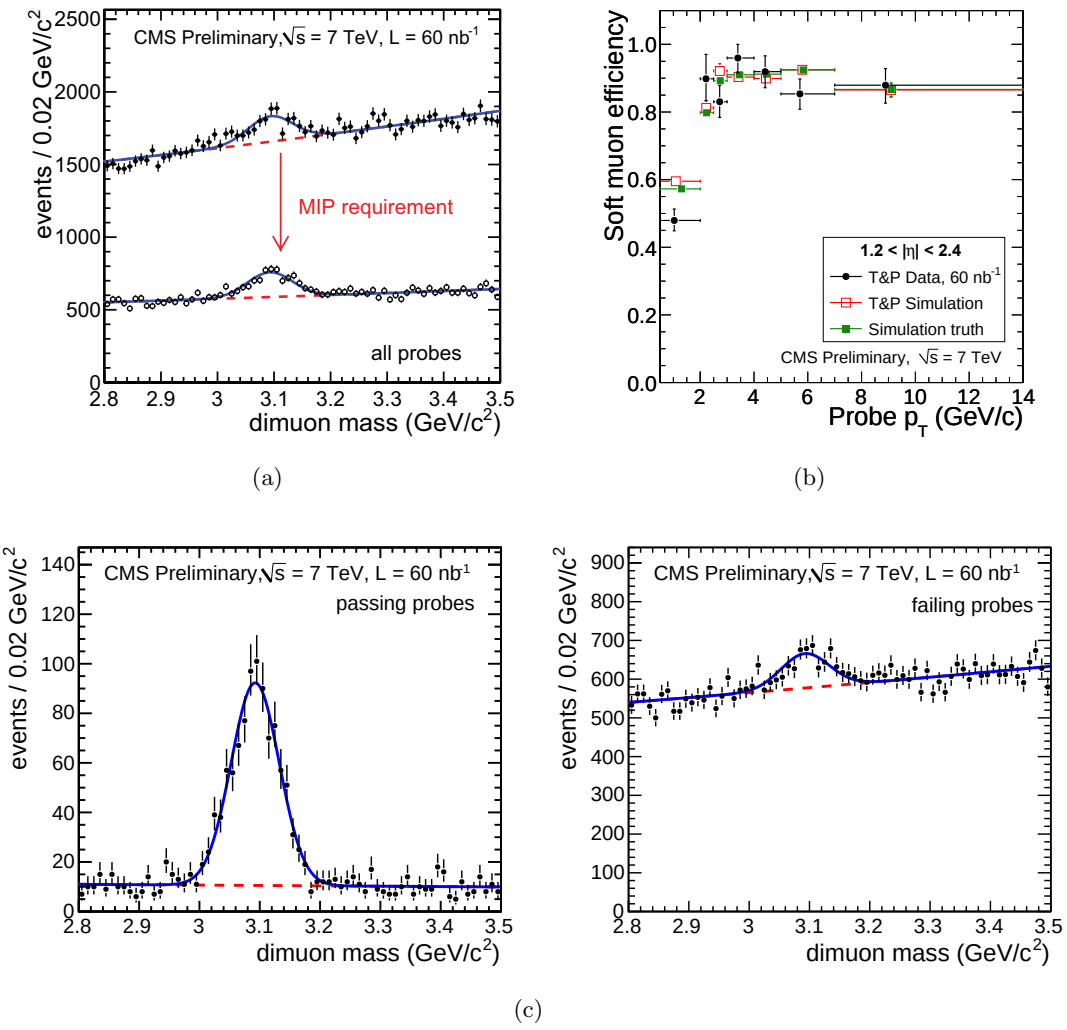

Figure 3.8: Example of background subtraction to determine the soft muon identity efficiency for $0 < p_T < 2\,Gev/c$ and $1.2 < |\eta| < 2.4$ given that the tracker track exists. 3.8(a) shows the reduction of the background (for all probes) using the MIP requirement. 3.8(c) these two plots show the line shapes for passing and failing probes. Background subtraction is applied, to produce the first bin in plot 3.8(b), where the tag-and-probe efficiencies as a function of p_T in the endcaps ($1.2 < |\eta| < 2.4$) in data and in simulation are compared to the efficiency with perfectly subtracted background in simulation.

the ones extracted applying the same procedure in the simulated events. The tag-and-probe results in data and in simulation agree within the statistical uncertainties of the measurement almost everywhere. The only significant discrepancy is in the barrel around the turn-on of the efficiencies, where the efficiency in data is systematically higher than in the simulations.

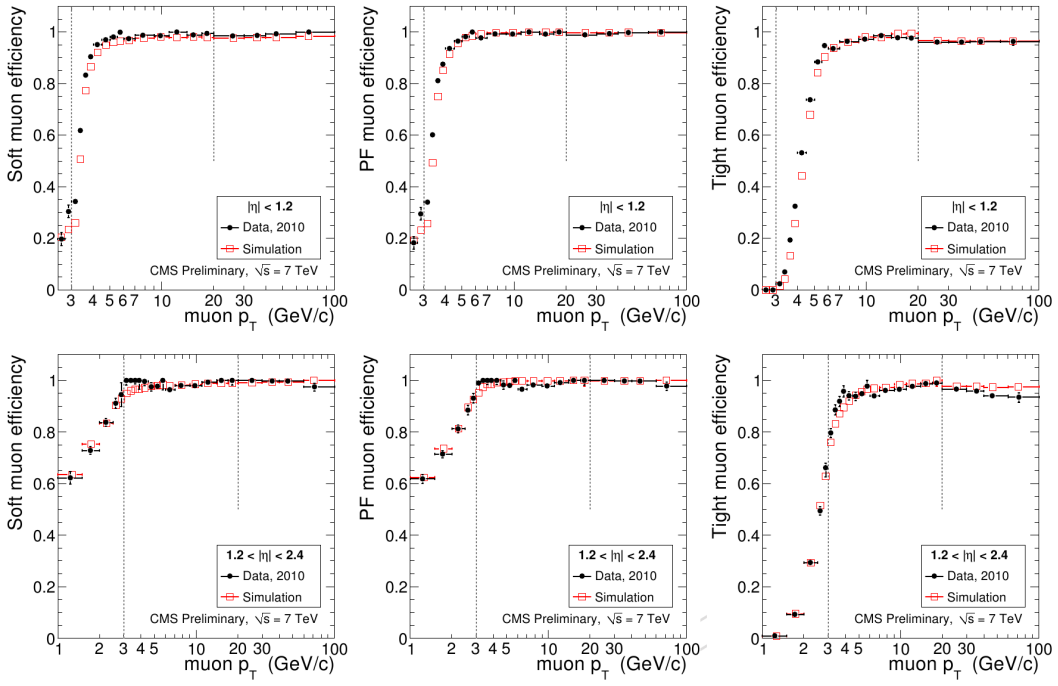

Figure 3.9: Tag-and-probe results for the muon identification efficiency in data compared to simulation. Given that a tracker track exist, the plots show the efficiency as a function of muon p_T for *soft muon* (left), *particle flow muons* (middle) and *tight muons* (right) in the barrel and overlaps (top) and in the endcaps (bottom). The measurement is done using the $J/\psi \to \mu^+\mu^-$ events for $p_T < 20\,GeV/c$ and $Z \to \mu^+\mu^-$ events above. For the tracks with $p_T < 3\,GeV/c$ MIP signature are consider.

4

The Quark Model

This chapter deals with the quark model, in particular its development of it and its new characters, like the *exotic* states. It will also given an overview of the discovery of the $X(3872)$ in the recent experiments.

4.1 The history

The preliminary study on the atom begun with the Rutherford scattering experiment. He probed the fact that the atom is composed by an heavy nucleus positively charged and a cloud of negative charged material.
This model viewed the atom like the solar system, with great part of the mass concentrated in the nucleus and was against the Thompson model which described the atom like a uniformly cake made by positively and negatively charged particles.
As occurs in optics, small wavelengths can probe smaller parts of the target, similarly electrons of high energies (and therefore small wavelengths) can scatter on protons inelastically, and in this way it is possible to look at the composition of the proton.
In the late part of the 1960*s* Bjorken [16] predicted at very high energy the dependence of the inelastic structure on function of the exchanged momentum between the particles colliding (q^2). The important thing is that at a given point, the exchanged virtual photon of the interaction interacts with the particles inside the proton, the *quarks*.
The quark model was born to explain and understand the proton composition in terms of quarks and gluons. The model also included a different type of quarks that was discovered in the meantime. After years of study, the whole scheme evolves to the model describing all the particles physics world: the standard model (SM).
The following Sections explain the basic model and its completion to describe the composition of the elementary particles. A brief overview of the theory which describes their decays within the SM is finally given.

4.2 Reaching the parton model

From the cosmic rays to the strange particles

After the discovery of the new particles in the cosmic rays, for a brief period in 1940s it was believed that the major problems of elementary particle physics were solved. After a lengthy detour in pursuit of the muon, the pion (Yukawa's meson), the positron (Dirac's antiparticle of the electron) were under control and observed. [17]
In December 1947 Rochester and Butler [18] published the cloud chamber photograph where they saw a decay into two charged secondary particles, forming the upside-down "V": there was a new neutral particle, with at least twice the mass of pion, later known as kaon K^0. The decay observed was: $K^0 \to \pi^+ + \pi^-$. In the subsequent years it was also observed the specular decay of the charged kaon: $K^+ \to \pi^+ + \pi^- + \pi^+$. The meson family was growing with the η, the ϕ, the ω and the ρ and others in the subsequent years. Also the baryon family was expanded with another particle: the $\sigma's$, the $\Xi's$, the $\Delta's$ and the Λ, saw in the 1950 in the decay channel: $\Lambda \to p + \pi^-$. The theorists tried to understand why the proton does not seem to decay. Because the proton is the lightest baryon, they try to explain the fact that it does not decay by introducing a new quantum number which has to be conserved: the *baryon number*. There is not any evidence of a conservation number for the mesons.
The discovery of the V^0 was a surprise and its production and its decays was strange for that period, so this particle was named "strange". In fact it is produced copiously on a time scale of about $10^{-23}\,s$, and decay relatively slowly $10^{-10}\,s$. With the nowadays interpretation, it is produced with strong force but decay with the weak force. To justify the particular decays, it was introduced a new quantum number: the strangeness. This number was not conserved in the weak interaction. The garden which seemed so tidy in 1947 had grown into a jungle by 1960: there were only two big families, the mesons and the baryons.

The eightfold way

An equivalent of the periodic table for the chemical elements was designed for particle by Murray Gell-Mann, who introduced the *Eightfold way* in the 1961, figure 4.2. This scheme arranges the baryons and the mesons into geometrical patterns, according to their number of strangeness and charge. In this way it was possible to arrange all the particles known in the 1960s.

The model predicted the existence of a new particle: it must had electric charge -1 and strangeness -3. In the 1964 the Ω^- was discovered, which in effect had the predicted quantum numbers of the Gell-Mann missing particle. In addition to the particle scheme

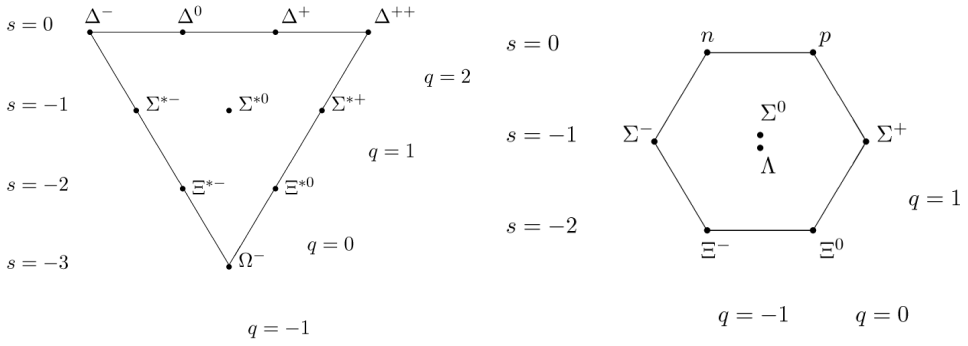

Figure 4.1: The multiplets of the baryons.

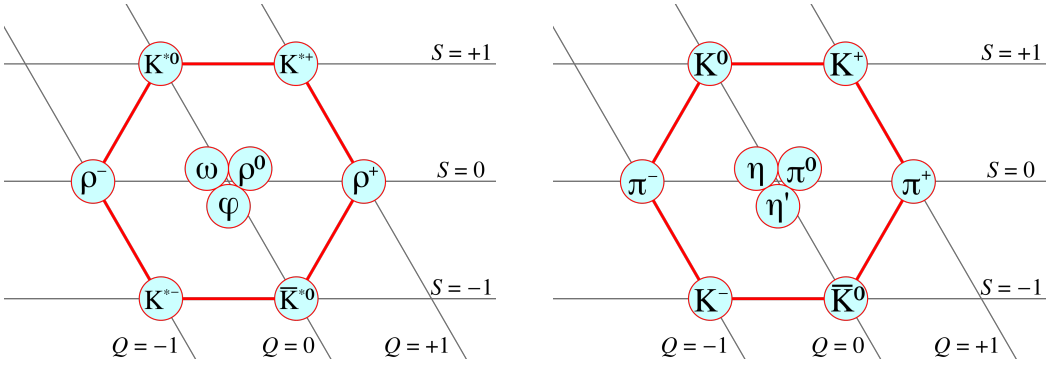

Figure 4.2: The multiplets of the mesons.

there exists an antiparticle geometric scheme. For the mesons, the antiparticles lie in the same multiplet, in diametrically opposite positions.
Classification with the Eightfold Way was the first step for a development of a coherent theory that classifies all the particles observed, and not.

Mediator of the forces

In nowadays view the entire universe could be described by the 6 leptons, 6 quarks and the mediator of the forces (Electromagnetic, Strong, Weak and Gravity).
In the Fermi beta decay theory (in 1933) the particles was treated as a point, the interactions occurring in a single point and therefore without the requiring of mediator particles. The weak force (responsable of the beta decay) is extremely short range, and the Fermi model was not so distant from the truth, and gave excellent results at low energies [1]. This approach was failing at high energies, and it had be replaced with a theory in which the interaction is mediated by an exchange of some particles: named *intermediate vector bosons*. Also Yukawa handled with this approach for the strong force, permitting him

[1] The approximation at low energy of some decays is reasonable because to the high mass of the vector intermediate boson, and the low value of the Fermi constant ($G_F = 1.166 \times 10^{-5}/GeV^2$)

to predict the pion mass in terms of the range of the force. After a period of speculation and guesses about the masses of these intermediate vector bosons, the unification of electromagnetic and weak forces in an electroweak theory by Glashow, Weinberg [19] and Salam gave a prediction about their masses. In this theory there are three intermediate bosons: two charged ($W^{\pm}$) and one neutral (Z), with masses: $m_{W^{\pm}} \sim 82\,GeV/c^2$ and $m_Z \sim 92\,GeV/c^2$.
In the 1970*s*, with the construction of the proton-antiproton collider designed to produce extremely heavy particles, the race to the intermediate vector bosons began. In 1983 [20] [21] the discovery of the W with $m_{W^{\pm}} = 81 \pm 5\,GeV/c^2$ and the Z with $m_Z = 95 \pm 5\,GeV/c^2$ represented a confirming crucial aspect of the Standard Model.

The quark model

With the success of the Eightfold Way a question of why the hadrons fit into these patters rose. A first answer came in 1964 when Gell-Mann and Zweig [22] [23] independently proposed that all hadrons are composed of even more elementary particles, called *quarks*. The quarks were of three types (or flavours): the u (up) quark carries a charge of $+\frac{2}{3} \times Q$, where Q is the charge of the electron, and 0 strangeness; d (down) carries a charge of $-\frac{1}{3} \times Q$ and 0 strangeness and s (strange) with charge $-\frac{1}{3} \times Q$ and strangeness 1. For every quark there was the corresponding anti-quark with opposite numbers.
The model states that:

- every baryon is composed of three quarks, or anti-quarks;
- every meson is composed of a quark and an anti-quark.

With these rules it is possible to reproduce the geometric multiplet scheme: all is made of combinations of a quark or of a quark and an anti-quark. Even in this model there is a prediction: the η'.
The failure to produce isolated quarks occasioned widespread scepticism about the model in the 1960*s* and 1970*s*: who clung to the model tried to conceal it by introducing the *quark confinement*: for reason still unknown, the quarks are absolutely confined within baryons and mesons, and it is impossible to see them as free particles. To confirm the inside structure of the nucleons, proton and neutron, it was possible to probe the inside of them in the same way as Rutherford probed the inside of the atom: firing something into it. This was possible in the accelerator laboratories: as SLAC and CERN. The results of this "deep inelastic scattering"confirm the Rutherford's idea: most of the incident particle pass through the target and a small number bounce back sharply. The mass of the proton is concentrated in its nucleus.
Another problem to be solved was the Pauli's exclusion principle. To save the model a new

quantic number was introduced. The quarks must carry another quantic "charge", named *colour* (red, blue and green), with following property all naturally occurring particle are colourless. Either the total amount of each colour is zero or all three colours are present in equal amounts. This seems to explain the impossibility to make a particle with two or four quarks, and why the individual quarks does not occur in nature.
The period from 1964 to 1974 was a difficult time for the elementary particle physics. The quark model, promising at the beginning, was in a state of idle. Something came out: the discovery of the J/ψ meson in 1974. The particle was discovered independently by Ting group at Brookhaven, and by Burton Richter's group at SLAC. First named it J [24] and the second ψ[25]. This particle was electrically neutral, and extremely heavy ($3.096\,GeV/c^2$) and it had an extraordinary short lifetime, $10^{-20}\,s$, 10^7 times less for the hadrons in this mass range. It was something unexpected and in the months that followed the true nature of J/ψ give a new positive push to the quark model. The new particle represents a state of a new quark, the c, *charm* together with its antiquark. The charm has the same properties of the *up* quark: charge $+\frac{2}{3} \times Q$ and 0 strangeness. Glashow, Iliopoulos and Maiani [26] offered more compelling reasons to the fourth quark, but the simple idea of a parallel between quarks and leptons is another of those speculations that turned out to have more substance. Evidence of charmed baryons appeared already in 1975: the $\Lambda_c^+ = udc$ and $\Xi_c^{++} = uuc$; the first charmed mesons ($D^0 = c\overline{u}$ and $D^+ = c\overline{d}$) were found in 1977.
The story of new bricks continued when a new *lepton* was discovered in 1975: the τ with its neutrino. With a leptons family increased by number, also the quark family was enlarged: the *Upsilon* was discovered [27], and it became clear that it is a carrier of a fifth quark, the b, *beauty, bottom*. The upsilon is a meson composed by $b\overline{b}$. As for the charmonium new particles, the beauty new particles were discovered in 1981-1983: baryon $\Lambda_b = udb$ and mesons $B^0 = b\overline{d}$, $B^0 = b\overline{u}$. The bottom has the same properties of the *down* quark: $-\frac{1}{3} \times Q$ and 0 strangeness. The new piece of the puzzle of the six family quark was found in 1995 at Tevatron, by the CDF and D0 experiment: the t, *top* [28]. It was predicted by Kobayashi and Maskawa, explaining the CP violation in the kaon decay. The top has the same properties of the *up* and the *charm* quark: charge $+\frac{2}{3} \times Q$ and 0 strangeness. With all these particles, the puzzle seemed complete: the jobs were passed to the theorist trying to build up a new theory convolving all of them, and with the possibility of new predictions: it came the Standard Model.

4.3 The theory of the quark model

The first schematic arrangement in multiplets of the particles was made by Heisenberg in 1930s, when he introduced the concept of *isospin* [29]. The hint for reaching this idea was

		t	t_3	Q_{e^-}	$bar.Num.$	q	J^P	m
first	u	$\frac{1}{2}$	$+\frac{1}{2}$	$+\frac{2}{3}$	$\frac{1}{3}$	0	$(\frac{1}{2})^+$	$1.7 - 3.1\, MeV/c^2$
generation	d	$\frac{1}{2}$	$-\frac{1}{2}$	$-\frac{1}{3}$	$\frac{1}{3}$	0	$(\frac{1}{2})^+$	$4.1 - 5.7\, MeV/c^2$
second	c	0	0	$+\frac{2}{3}$	$\frac{1}{3}$	$1, c$	$(\frac{1}{2})^+$	$100^{+30}_{-20}\, MeV/c^2$
generation	s	0	0	$-\frac{1}{3}$	$\frac{1}{3}$	$1, s$	$(\frac{1}{2})^+$	$1.29^{+0.05}_{-0.11}\, GeV/c^2$
third	t	0	0	$+\frac{2}{3}$	$\frac{1}{3}$	$1, t$	$(\frac{1}{2})^+$	$172.9^{\pm 0.6}_{\pm 0.9}\, GeV/c^2$
generation	b	0	0	$-\frac{1}{3}$	$\frac{1}{3}$	$1, b$	$(\frac{1}{2})^+$	$4.19 - 4.67^{+0.18}_{-0.06}\, GeV/c^2$

Table 4.1: Quarks: t is the isospin number, $bar.Num.$ is the baryon number, Q is the charge and q is the *flavour* of the quark.

given by similar mass of the two known baryons: the proton ($m = 938.3\, MeV/c^2$) and the neutron ($m = 938.3\, MeV/c^2$). Other additional hints were given by the similar cross sections for processes pp and pn and by the level of specular nuclei[1]. An internal degree of freedom can be introduced: the nucleon can have two possible states, the proton and the neutron. Like for the spin ($S = \frac{1}{2}$ with two projection $S_3 = \pm\frac{1}{2}$), the nucleon was defined as $I = \frac{1}{2}$ with $I_3 = +\frac{1}{2}$ for the proton and $I_3 = -\frac{1}{2}$ for the neutron.
With this new quantum number (4.1) it can be reproduced the charge of the particles (in e^- charge units), with the relation [30]:

$$Q = I_3 + \frac{Bar + S + C + B + T}{2} \tag{4.1}$$

where Bar is the baryon number, and S, C, B and T are the quantum numbers (flavour) of the quark that compose the particle. This *flavour* has, by convention, the same sign of the charge, Q. This convention permits to any charged meson to carry the flavour with the same sign of the charge, for example: the strangeness of the K^+ is $+1$, the bottomness of the B^+ is $+1$ and the charm and strangeness of D_s^- are both -1. The anti-quarks have the opposite flavour signs.

The mesons

Mesons have baryon number equal to 0. They are bound states of two different quark and anti-quark ($q\overline{q'}$), not necessary with the same flavour. If the bound state $q\overline{q'}$ has orbital angular momentum l, the parity is defined in this way: $P = (-1)^{l+1}$, and the spin of the meson is given by the relation $|l - s| \leq J \leq |l + s|$, where s is 0 for anti-parallel quark spins, or 1 for parallel quark spins. The charge conjugation, the $C-$parity, is defined as $C = (-1)^{l+s}$, only for the $q\overline{q}$ bound state, with the same type of quark.

With these numbers it is possible to arrange the quarks in J^{PC} multiplets. The $l = 0$ states are the pseudoscalars (0^{-+}) and the vectors (1^{--}); the excitations, with $l = 1$

[1] where the number of protons and neutron are exchanged

are the scalars (0^{++}), the axial vectors (1^{++} and 1^{+-}) and the tensors (2^{++}). Radial excitation could be denoted by its principal quantum number n. Due to the very short lifetime of the quark t bound state hadrons containing it or its anti-partner cannot exist. In natural spin-parity series $P = (-1)^J$, the particles have to be $s = 1$ and $CP = +1$, so natural spin-parity and $CP = -1$ (0^{+-}, 1^{+-}, 2^{+-} and so on) are forbidden when using $q\overline{q'}$ as well as $J^{PC} = 0^{--}$.
To explain and understand better the quark model, it is important to handle the group symmetry.

4.3.1 The symmetry group

For a better understanding of the quark model are useful some informations about the symmetry groups.
In general, a $SU(N)$ group is the collection of the unitary matrices $N \times N$ with determinant equals to 1. The hermitian $N \times N$ matrices with null trace linearly independent are $N^2 - 1$. Let us indicate with F_a this set of hermitian matrices with that characteristic: these are the *generators* of the group. These generators have to satisfy this commutation rule:

$$[F_a, F_b] = i\, C^c_{ab}\, F_c \qquad \text{with} \quad c = 1, 2, \ldots N^2 - 1 \tag{4.2}$$

The constants C^c_{ab} are called *structure constants* of the group and they are antisymmetric in the index a and b.
There are two theorems useful for the subsequent steps.
First: when there is a hermitian representation of the Lie algebra of a group, F_a , $a = 1, 2 \ldots N^2 - 1$, it is always possible to find another algebra's base.
A representation of a semi-simple algebra is called *fundamental* if it is irreducible and finite dimensional. In the case of of $SU(N)$ the *fundamental representation*, the defining representation of the group, is hermitian and so the theorem is valid. It is also possible to consider always the structure constants antisymmetric.
Second: if the adjoint representation (defined below) of the Lie algebra is irreducible, the diagonalizability of $\tilde{F}_a, \tilde{F}_b$ from λ is valid for every base of the algebra. The adjoint representation of $SU(N)$ is irreducible $\forall N$:

$$tr(\tilde{F}^{(r)}_a, \tilde{F}^{(r)}_b) = T^{(r)}_R \delta_{ab} \qquad \text{with}\, T^{(r)}_R > 0$$

$T^{(r)}_R$ is called the Dinkin index. The adjoint representation of the algebra of a group is the representation obtained using the Jacobi identity and it is also possible to define:

$$[F^{adj}_a, F^{adj}_b] = i\, f_{abe}\, F^{adj}_e \tag{4.3}$$

that are the commutation rules of the $SU(N)$ algebra, and F_a^{adj} is the *adjoint representation* of $SU(N)$.

If there are some generators that commute between each other, according to the formulas 4.2 and 4.3, they form a set of generators called *Cartan subalgebra*.

Some examples could explain better this theorem.

If $N = 2$ and the group is $SU(2)$, the generators are 3 ($= N^2 - 1$). They are T_a with $a = 1, 2, 3$, and the fundamental representation is defined as:

$$T_a^{(f)} = \frac{1}{2}\sigma_a \qquad \text{where } \sigma_a \text{ are the Pauli matrices} \tag{4.4}$$

The adjoint representation is obtainable with the same procedure defined before.

Since the first discovery of the parton components, this representation scheme was adopted by physicist. The $SU(2)$ group could describe the isospin quantum number as well as the spin in the atoms.

Another useful example is the case when $N = 3$. The $SU(3)$ group has 8 generators, defined as:

$$T_a^{(f)} = \frac{\lambda_a}{2} \qquad \text{where } a = 1, 2 \dots 8 \tag{4.5}$$

and the *lambda matrices* are:

$$\lambda_1 = \begin{pmatrix} 0 & 1 & 0 \\ 1 & 0 & 0 \\ 0 & 0 & 0 \end{pmatrix} \; \lambda_2 = \begin{pmatrix} 0 & -i & 0 \\ i & 0 & 0 \\ 0 & 0 & 0 \end{pmatrix} \; \lambda_3 = \begin{pmatrix} 1 & 0 & 0 \\ 0 & -1 & 0 \\ 0 & 0 & 0 \end{pmatrix} \; \lambda_4 = \begin{pmatrix} 0 & 0 & 1 \\ 0 & 0 & 0 \\ 1 & 0 & 0 \end{pmatrix}$$

$$\lambda_5 = \begin{pmatrix} 0 & 0 & -i \\ 0 & 0 & 0 \\ i & 0 & 0 \end{pmatrix} \; \lambda_6 = \begin{pmatrix} 0 & 0 & 0 \\ 0 & 0 & 1 \\ 0 & 1 & 0 \end{pmatrix} \; \lambda_7 = \begin{pmatrix} 0 & 0 & 0 \\ 0 & 0 & -i \\ 0 & i & 0 \end{pmatrix} \; \lambda_8 = \tfrac{1}{\sqrt{3}} \begin{pmatrix} 1 & 0 & 0 \\ 0 & 1 & 0 \\ 0 & 0 & -2 \end{pmatrix}$$

with only λ_3 and λ_8 diagonal. The commutation rules and the traces are:

$$[F_a^{(f)}, F_b^{(f)}] = i\, f_{abc}\, F_c^{(f)} \qquad tr(F_a^{(f)}, F_b^{(f)}) = \frac{1}{2}\delta_{ab} \qquad \text{where } F_a = \frac{1}{2}\lambda_a \tag{4.6}$$

by using the commutation rule, it is possible to define new quantities:

$$\begin{gathered} T_\pm \equiv F_1 \pm iF_2 \qquad U_\pm \equiv F_6 \pm iF_7 \qquad V_\pm \equiv F_4 \pm iF_5 \\ T_3 \equiv F_3 \qquad Y \equiv \frac{2}{\sqrt{3}}F_8 \end{gathered} \tag{4.7}$$

and using the 4.6, it is possible to find that the T_1, T_2, T_3, V_1, V_2, V_3 and U_1, U_2, U_3 form three subalgebras, called: $T-$spin, $V-$spin and $U-$spin. T_1, T_2, T_3 are the $SU(2)$ generators. The diagonal λ matrices of the 4.3.1 could be associated with observables:

$$I_3 = \frac{1}{3}\lambda_3 \qquad Y = \frac{1}{\sqrt{3}}\lambda_8 \tag{4.8}$$

where I_3 is the third component of the isospin, and Y is the hypercharge. In the $SU(3)$ group a possible set of compatible observables is composed of: $F^{(2)}, G^{(3)}, T^{(2)}, T_3, Y$[1] [2]. With the eigenvalues of these five numbers, it is possible to identify a state. In every representation it is possible to find simultaneous eigenstates of the operator $T^{(2)}, T_3$ and Y.

With a fixed representation it is possible to draw the eigenvalues of T_3 and Y (t_3 and y), and every points could be degenerate in the isospin values $T^{(2)}$. In this plot the $T_\pm, U_\pm, V_\pm$ operators could move the eigenvalues t_3 and y:

- T_+ raises the t_3 of 1 and doesn't change the y;
- U_+ reduces the t_3 value of $\frac{1}{2}$ and raises y of 1;
- V_+ raises t_3 of $\frac{1}{2}$ and y of 1.

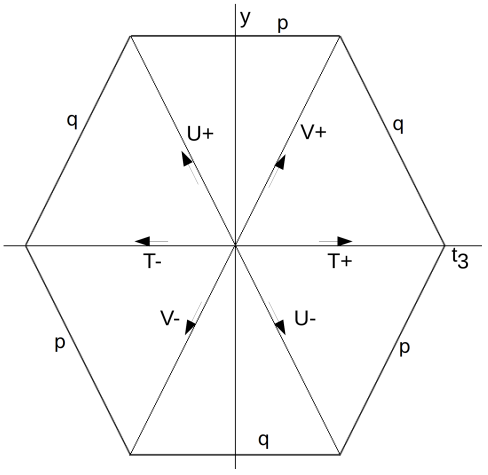

Figure 4.3: Representation of the eigenvalues of t_3 and y, and the action of the operators.

and the opposite sign operators works in the opposite way, fig. 4.3.

Now it is important to set the maximum border, for example starting from the maximum t_3 value, in this state:

$$T_+|\psi_{max}\rangle = 0 \qquad V_+|\psi_{max}\rangle = 0 \qquad U_-|\psi_{max}\rangle = 0$$

and only the U_+, V_- and T_- could operate on it. So it could be possible to proceed in the V_- direction $p-$times till:

$$V_-^{p+1}|\psi_{max}\rangle = 0$$

Then, it is possible to go in the T_- direction till the null result. After q steps in the T_- direction, one could proceed in the U_+ direction then in the T_+, and finally in the U_-

[1] defined as: $F^{(2)} = \sum_{a=1}^{8} F_a^2$

[2] defined as: $G^{(3)} = \frac{2}{3} d_{abc} F_a F_b F_c$

direction, till coming back to the starting point. A regular hexagon symmetric among the $y-$axis it is drawn: with three sides long p and three long q, fig. 4.3. The vertices is defined as a $|\psi_{max}\rangle$. The dimension of the representation, with p and q fixed, is defined as:

$$d(p,q) = \frac{1}{2}(p+1)(q+1)(p+q+2) \tag{4.9}$$

Using this formula it is possible to draw different shapes, like shown in the figure above 4.4. In the 1964 the isospin multiplets were known, they are represented by a $SU(2)$ group

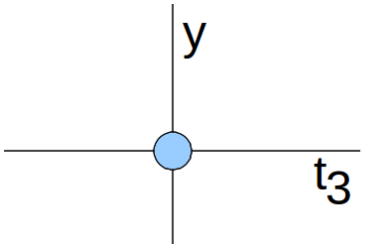

(a) Representation with: $p = 0$ and $q = 0$, dimension 0: it is the *banal representation.*

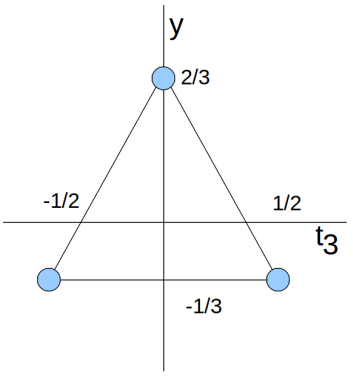

(b) Representation with: $p = 1$ and $q = 0$, dimension 3: it is the *fundamental representation.*

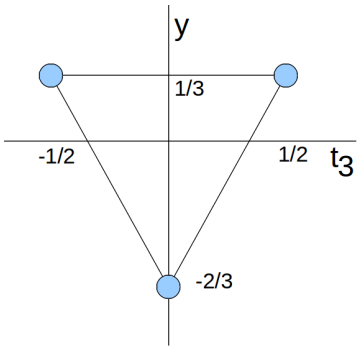

(c) Representation with: $p = 0$ and $q = 1$, dimension 3: it is the *adjoint representation*, also called 3^*.

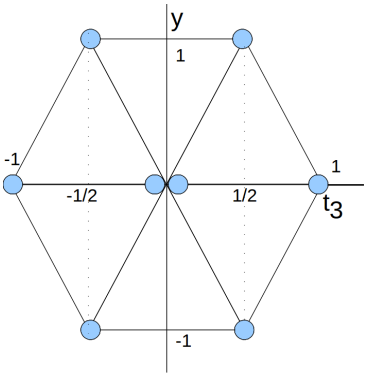

(d) Representation with: $p = 1$ and $q = 1$, dimension 8: at the centre there are degeneration 2.

Figure 4.4: Possible representations in different dimension.

(approximate) symmetry.

Gell-Mann & Ne′eman tried to extend the group to a $SU(3)$: they called this new symmetry *flavour symmetry.* It is an approximate symmetry due to the mass terms in the Lagrangian. The isospin multiplets known at that time were:

- *isosinglet:* $t = 0$: $\underset{Q=t_3=B=0}{\eta\,\eta'\,\omega\,\phi}$ $\underset{Q=t_3=0B=1}{\Lambda^0}$

- *isodoblet:* $t = \frac{1}{2}$: $\underset{\substack{Q = t_3 + \frac{1}{2} \\ B = 1}}{\begin{pmatrix} p \\ n \end{pmatrix}}$ $\underset{\substack{Q = t_3 + \frac{1}{2} \\ B = 0, S = 1}}{\begin{pmatrix} K^+ \\ K^0 \end{pmatrix}}$ $\underset{\substack{Q = t_3 - \frac{1}{2} \\ B = 0, S = -1}}{\begin{pmatrix} \overline{K^0} \\ K^- \end{pmatrix}}$ $\underset{\substack{Q = t_3 - \frac{1}{2} \\ B = 1, S = -2}}{\begin{pmatrix} \Xi^0 \\ \Xi^- \end{pmatrix}}$
- *isotriplet:* $t = 1$: $\underset{\substack{Q = t_3 \\ B = 0}}{\begin{pmatrix} \pi^+ \\ \pi^0 \\ \pi^- \end{pmatrix}}$ $\underset{\substack{Q = t_3 \\ B = 1, S = -1}}{\begin{pmatrix} \Sigma^+ \\ \Sigma^0 \\ \Sigma^- \end{pmatrix}}$ $\underset{\substack{Q = t_3 \\ B = 0}}{\begin{pmatrix} \rho^+ \\ \rho^0 \\ \rho^- \end{pmatrix}}$
- *isoquadruplet:* $t = \frac{3}{2}$: $\underset{\substack{Q = t_3 + \frac{1}{2} \\ B = 1, S = 0}}{\begin{pmatrix} \Delta^{++} \\ \Delta^+ \\ \Delta^0 \\ \Delta^- \end{pmatrix}}$

and it is possible to rearrange them into the multiplets show in fig. 4.1 and 4.2.
Another important representation is the *complex representation*. We can start from a general matrix belonging to $SU(N)$:

$$U = e^{i\sum_{a=1}^{N^2-1} \epsilon_a F_a} \quad \text{with: } [F_a, F_b] = i\, f_{abc}\, F_c \quad \text{and: } f_{abc} \text{ real} \tag{4.10}$$

then we can define the complex representation as:

$$U^* = e^{i\sum_{a=1}^{N^2-1} \epsilon_a F_a^*} \equiv e^{i\sum_{a=1}^{N^2-1} \epsilon_a \tilde{F}_a^*} \quad \text{where: } \tilde{F}_a^* \equiv -F_a^* \tag{4.11}$$

The operators $\tilde{F}_a^*$ satisfy the same commutation rules of F_a, formula 4.2. The $\tilde{F}_a$ is called the *complex-conjugate representation*. In the $SU(3)$ group, the representation is not real and, with some other theorems, the 3 and the 3^* are not equivalent.

4.3.1.1 Compositions of representations

Studying the composition of fundamental representations gives and overview on the hadronic physics.
Describing the total system with the basis, it could be possible to rewrite it with the *Clebsh-Gordan series*. Every reducible representation could be written as sum of irreducible representations with opportune Clebsh-Gordan coefficients .
In the $SU(2)$ group the composition of representations is done using the additivity of the J_2. In particular imagine that it is possible to put at the centre of every state the other, and then count the states.

In the $SU(3)$ group it is using the additivity of t_3 and y.
For example, the $3 \oplus 3^*$ is calculating using the fundamental and the adjoint representations, figures 4.4(b) and 4.4(c).

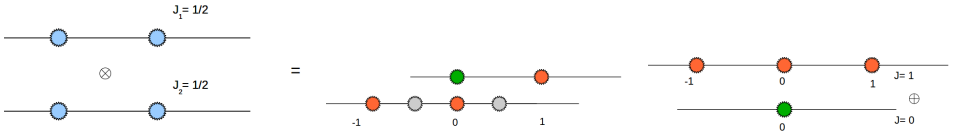

(a) Initial state: $J_1 = \frac{1}{2} \otimes J_2 = \frac{1}{2}$ (b) intermediate state (c) final State: $J = 1 \oplus J = 0$

Figure 4.5: Compositions of states in $SU(2)$

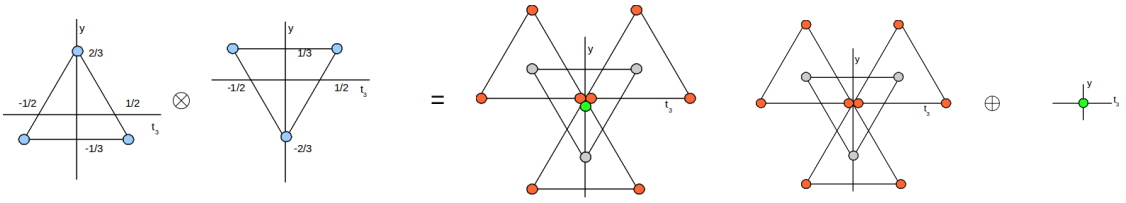

(a) Initial state: $3 \otimes 3^*$ (b) intermediate state (c) final State: $1 \oplus 8$, fundamental ones

Figure 4.6: Compositions of states in $SU(3)$

The Gell-Mann idea was to match the three fundamental states with the three quarks known (u. d and s), as the simultaneous eigenvectors of the diagonal matrices, defined in 4.8.

$$q^1 = u = \begin{pmatrix} 1 \\ 0 \\ 0 \end{pmatrix} \qquad q^2 = d = \begin{pmatrix} 0 \\ 1 \\ 0 \end{pmatrix} \qquad q^3 = s = \begin{pmatrix} 0 \\ 0 \\ 1 \end{pmatrix}$$

The quarks could be identified as the vertices of the triangles of the fundamental representation and the anti-quarks as the vertices of the adjoint one.
If we use three quarks, the baryons are represented, ordered in octuplets and decuplets, as in figure 4.1.

$$3 \otimes 3 \otimes 3 = 3 \otimes (3^* \oplus 6) = 1 \oplus 8 \oplus 8 \oplus 10 \tag{4.12}$$

As it is mentioned at the beginning of the chapter, the hadrons are classified in:

- *mesons*: as bound states of $q\overline{q}$, with group: $3 \otimes 3^* = 1 \oplus 8$, in singlet and eightuplet. They are bosons ($J = 0, 1, 2, \dots$) and have baryon number 0;

- *baryons*: as bound states of qqq, with group: $3 \otimes 3 \otimes 3 = 1 \oplus 8 \oplus 8 \oplus 10$, in singlet, eightuplet and decuplet. They are fermions ($J = \frac{1}{2}, \frac{3}{2}, \frac{5}{2}, \dots$) and have baryon number 1;

  anti-baryons: as bound states of $\overline{qqq}$

They are classifiable using their spin: mesons with $J^P = 0^-$, spin 0 (octuplet), figure 4.2; baryons with: $J^P = \frac{1}{2}^+$ in octuplet and $J^P = \frac{3}{2}^+$ in decuplet, figure 4.1.
When three quarks (u, d and c) were discovered the natural group was the $SU(3)$ and using the $q\overline{q'}$ nine possible combinations The discovery of the fourth generation of quark can be consider in the mathematical overview expanding the group to $SU(4)$: the heavier mass of the c respect to the other three quarks is responsable for the badly broken of the group. The group of 16 elements could be decomposed into a 15−plet and a singlet:

$$\mathbf{4} \oplus \overline{\mathbf{4}} = \mathbf{15} \oplus \mathbf{1} \tag{4.13}$$

The baryon in the most general case they are composed of three quarks, with the possibility of adding a quark anti-quark pair, maintaining the colourless of the hadron. This characteristic forms an $SU(3)$ singlet, a state completely antisymmetric of the three colours. The state function of the quarks, as fermions, must be antisymmetric under interchange of any two equal-mass quarks. The normal baryons are made up by u, d and s quarks. These flavours imply an approximate flavour $SU(3)$, forcing the baryon to be in this scheme:

$$\mathbf{3} \oplus \mathbf{3} \oplus \mathbf{3} = \mathbf{10_S} \oplus \mathbf{8_M} \oplus \mathbf{8_M} \oplus \mathbf{1_A} \tag{4.14}$$

where the subscripts indicate the states under interchange of any of two quarks: symmetric, mixed-symmetric and antisymmetric. The **1** is a uds state (Λ_1) and there is a similar state in the octet (Λ_8); with the same spin and parity they can mix.
The addition of the c quark to the light quarks extend the symmetry to an $SU(4)$ group: symmetry is broken in a strong way, due to the heavier mass of the new entry. The addiction of the b extends the flavour symmetry to $SU(5)$. The existence of hadrons with the t quarks is very unlikely, due to the short lifetime of the quark top.

4.4 Quantum Chrodynamics and hadron production

After the discovery of the mechanism of the combinations of quarks in the particles, the overview of the scheme evolves to a complete gauge theory, part of the SM: the *Quantum Chromodynamics, QCD*. The theory is based on the $SU(3)$ symmetry group, where the rule of the charge is played by the colour of the quark (red, green and blue), in the same way of the electric charge for the electromagnetic force. The quark model is a simplified version of this theory. In particular, the quantum chromodynamics introduces rules to compute the dynamic of the quark and gluon interactions.
In this theory the hadrons are not only composed of the valence quarks, but must consider also gluons as well as the virtual quarks anti-quarks pairs. The landscape with this theory is bigger with the *exotic* states.

Glueballs are only made by valence gluons, and no quarks. The theoretical calculations show that this kind of "particle"could exist at energy available at the current colliders. Its difficult detection derives from their mixing with ordinary mesons states, at the moment there are not secure signal of it.

Hybrids contains valence quarks and gluon(s). Their ground state mass spectrum are excepted to be in the order of $1.8\,GeV/c^2$, a possible candidate are $\pi_1(1400)$ $\pi_1(1600)$. Some hybrids are predicted to have exotic quantum numbers which would signal a non$-q\overline{q}$ state. Almost all models of hybrids predicted that hybrids with conventional quantum numbers have very distinctive decay modes, distinguishable from the conventional states.

Multiquark states: *molecular states* are a loosely bound state of a pair of mesons near threshold of the particle. One signature of these states is that they exhibit a large isospin violation.

Tetraquark are mesons containing two pairs of quark anti-quark states. At the moment there have been no confirmed reports of a tetraquark evidence state, although the $f_0(980)$ is considered by someone to be a light tetraquark state. Other two narrow states (the $D_{sJ}(2317)^{*\pm}$ and $D_{sJ}(2460)^{*\pm}$) have also been interpreted as states of tetraquark. A prediction of tetraquark models is that they are expected to come in flavour multiplets.

Pentaquark are baryons that contain four quarks and one anti-quark. The LEPS collaboration reported in the 2003 the evidence for the Θ^+, a pentaquark state candidate with mass of $\sim 1540\,GeV/c^2$ and composite by $ud\overline{u}d\overline{s}$ quark. This state was documented by a lot of experimental papers but it was not confirmed in the B factories and other HEP experiments.

The discoveries of the last years puts a new interest in the possibility of the existence of mesons with a more complex structure than the simple $q\overline{q}$ states of the quark model. The searches for this new type are made by looking for systems including a charm quark (charmonium state) $c\overline{c}$, because in some of these cases the states are expected to have an experimental clean signature and relatively narrow widths.

The X,Y and Z mesons family represent one of this new charmonium state.

Charmonium state

One possible meson state is represented by the composition of a c and a $\overline{c}$ quarks, the resultant state is called *charmonium*. The bound state of two quarks is an analogy with an atom model, where two particles, oppositely charged, are bound together. The dominant force, instead of the electromagnetic one with the exchange of a photon, is the strong one, mediated by gluon exchanges.

The label of the spectroscopy of the charmonium states is the same of the atomic spectroscopy. n is the radial excitation, $S, P, D, \ldots$ corresponding to $L = 0, 1, 2, \ldots$ are the

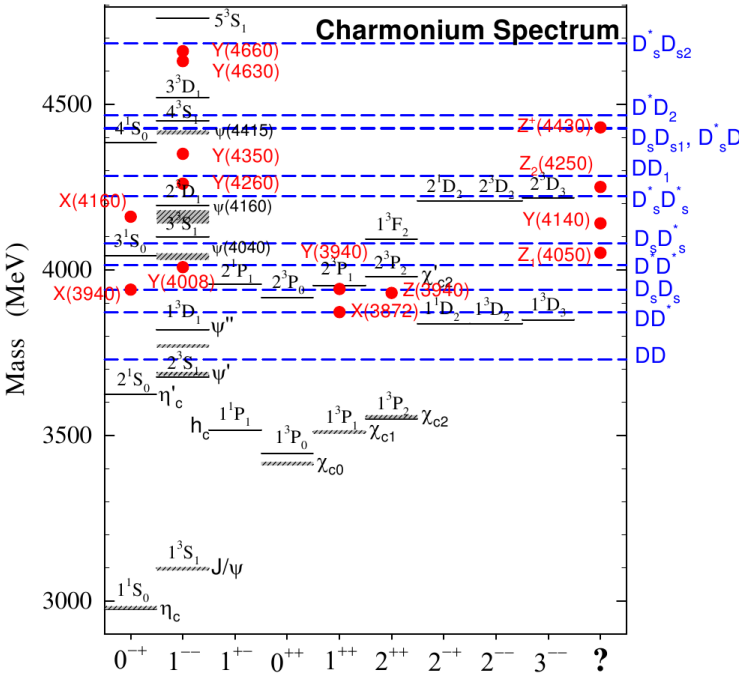

Figure 4.7: Charmonium spectrum. The solid lines are quark mode predictions, the shaded lines are the observed conventional charmonium states, the horizontal dashed lines represent various $D_s^{(*)}\overline{D}_s^{(*)}$ thresholds, the red dots are the newly discovered charmonium-like states placed in the column with the most probable spin assignment. The state in the last column do not fit elsewhere and appear to be truly exotic.

orbital angular momenta between the quarks, $S = 0, 1$ is the combined spin of the two quarks: the total angular momentum is defined as $J = L \oplus S$. The notation becomes: $(n+1)^{2S+1}$. [1]

The other important number use to classify the states is J^{PC}, with relations: $P = (-1)^{L+1}$ and $C = (-1)^{L+S}$. As example, the lightest charmonium state is the η_c with $J^{PC} = 0^{-+}$: the two quarks spins are arranged to have total spin 0 and orbital momentum null, the resultant total momentum is null $J = 0$. In spectroscopy notation it is known as 1^1S_0. The subsequent state, with increased S, is the J/ψ, known as 1^3S_1 and with $J^{PC} = 1^{--}$. The excitations of these states are the η_c' and the ψ' (also known as $\psi(2S)$): their spectroscopy notations are 2^1S_0 and 2^3S_1, respectively. There are other bound states with $L = 1$.

There are not higher states because they would have the masses above the $D\overline{D}$ threshold ($\sim 3.730 - 4.015 GeV/c^2$). The states with higher masses are kinematically allowed to decay into two mesons D. If this channel is not suppressed for some reasons, it would become dominant because it is a strong decay involving low energy gluons. But this state is also difficult to isolate because to its broad state mass. As example, there are narrow even

[1] Another option is to use: for $L-$even singlet (triplet) state η (ψ) with $S = 0$ ($S = 1$), for $L-$odd singlet (triplet) state h (χ) with $S = 0$ ($S = 1$).

state above the $D\overline{D}$ threshold, because they can not decay into $D\overline{D}$ for the conservation of parity.
Now it is given an overview of the exotic charmonium states: the $Y(4140)$ and the $Z(4400)$.

The Y(4140)

The CDF Collaboration found evidence for $Y(4140)$ in the $J/\psi\phi$ invariant mass distribution from the decay $B^+ \to J/\psi\phi K^+$ [31]. The state, with significance $3.8\,\sigma$, has mass $4143^{+2.9}_{-1.2}\,MeV/c^2$. Because both the J/ψ and ϕ have $J^{PC} = 1^{--}$, the $Y(4140)$ has to have $+$ parity.
This state does not seem to be a *Conventional state*, since its mass is above the charm threshold. Hence it would be expected to have a large width, which is in contradiction to the measured one ($\Gamma = 11.7 \pm 3.7\,MeV/c^2$). It is, therefore, unlikely to be a $c\bar{c}$ state.
An other interpretation of this state is given by tetraquark model, or by a charmonium hybrid and a molecule of D mesons. Further studies on the decay modes will help to distinguish between the various possibilities.

The Z(4400)

The Belle Collaboration observed a number of charmonium like states in B decays that carry charge [32], this indicate that they cannot be conventional $c\bar{c}$ state. The observed peak has a statistical significance of $6.5\,\sigma$. The mass of the state is: $4443^{+4}_{-2}\,MeV/c^2$. The unusual properties of $Z^+(4430)$ led to unusual explanations. Tetraquark state: $[cu][\overline{cd}]$, threshold effect of $D^*\overline{D}_1(2420)$ or a molecule of $D^*\overline{D}_1(2420)$ with $J^P = 0^-, 1^-$. Belle has also observed two resonance structure in $\pi^+\chi_{c1}$ mass distributions. Confirmation is needed for all of three them.

4.5 The X(3872) particle

The discovery

In the 2003 the Belle Collaboration reported the observation of a new narrow charmonium state produced in the exclusive decay process $B^\pm \to K^\pm\pi^+\pi^- J/\psi$, showed in figure 4.8 [33]. The principal decay mode of this state was into $\pi^+\pi^- J/\psi$ and had a mass of $3872 \pm 0.6(stat) \pm 0.5(sys)\,MeV/c^2$, very close to the mass threshold of two D mesons. 35.7 ± 6.8 events were collected in total, with a statistical significance of 10σ. Due to the unclear nature of this new particle the given name was $X(3872)$.

The CDF collaboration confirm this observation very quickly with a significance excess of 730 ± 90 candidates in the invariant mass spectrum of $J/\psi\pi^+\pi^-$[34], figure 4.9. Other confirmations in that channel came from the D0 and BaBar Collaborations.

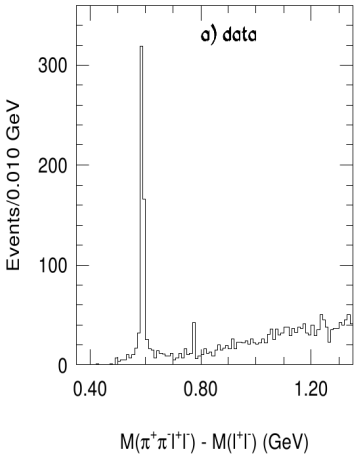

Figure 4.8: Distribution of the $M(\pi^+\pi^- l^+ l^-) - M(l^+ l^-)$ for selected events.

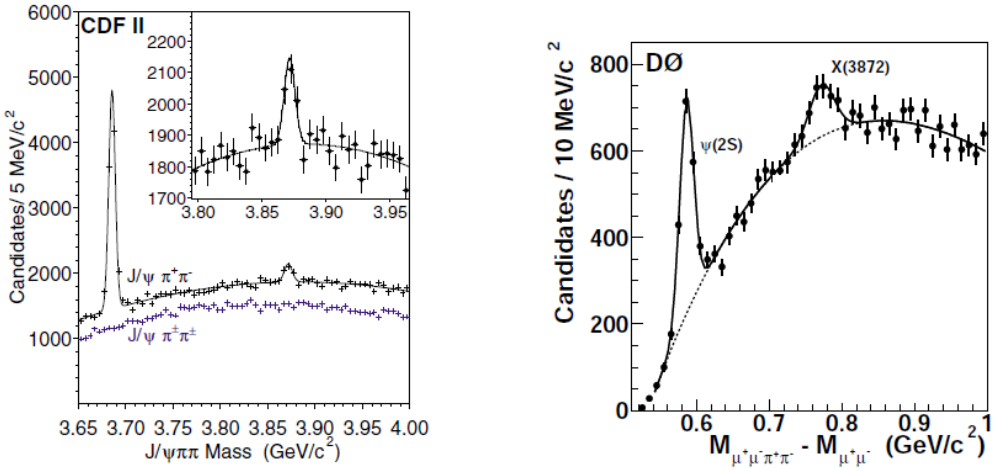

Figure 4.9: Left, CDF: the mass distribution of $J/\psi\pi^+\pi^-$ and $J/\psi\pi^\pm\pi^\pm$ candidates selection, the peak on the left is the $\Psi(2S)$; Right, D0: $\Delta M = M(\pi^+\pi^- l^+ l^-) - M(l^+ l^-)$ for the selected events.

Decay Mode	Mass (MeV/c^2)	Width (MeV)	Experiment
$J/\psi\pi^+\pi^-$	$3871.46 \pm 0.37 \pm 0.07$	1.4 ± 0.7	Belle
$(B^\pm)$	$3871.4 \pm 0.6 \pm 0.1$	$1.1 \pm 1.5 \pm 0.2$	BaBar
(B^0)	$3868.7 \pm 1.5 \pm 0.4$	-	BaBar
	$3871.8 \pm 3.1 \pm 3.0$	-	D0
	$3871.61 \pm 0.16 \pm 0.19$	-	CDF
$D^{0*}\overline{D^0}$	$3875.1^{+0.7}_{-0.5} \pm 0.5$	$3.0^{+1.9}_{-1.4} \pm 0.9$	BaBar
	$3872.9^{+0.6+0.4}_{-0.4-0.5}$	$3.9^{+2.8+0.2}_{-1.4-1.1}$	Belle

Table 4.2: The $X(3872)$ mass and width measurements by decay mode and experiment. $(B^\pm)$ and (B^0) represent mass values quoted by BaBar in charged and neutral B-decays, respectively.

The observation of the decay $X \to J/\psi\pi^+\pi^-$ was also observed to occur in prompt production from $p\overline{p}$ by Tevatron experiments. CDF also studied the angular distributions and correlations of the $J/\psi\pi^+\pi^-$ final state [35], finding that the dipion system was favoured to form a ρ^0. However, the decay $c\overline{c} \to \rho J/\psi$ violates isospin and should be strongly suppressed. The J^{PC} assignments 1^{++} and 2^{-+} explained their measurements adequately. Belle also reported evidence for the decay $J/\psi\gamma$ [36], confirmed also by BaBar experiment. The radiative decay verifies the positive $C-$parity assignment of CDF observation. It also reinforces the 1^{++} assignment because the 2^{+-} state would have to undergo in a high-order multipole transition which would be more strongly suppressed than the observed rates allow.
It has been observed also the decay $X(3872) \to D^0\overline{D}^0\pi^0$, by Belle and the decay $X(3872) \to D^0\overline{D}^0\gamma$ by BaBar. These decays imply that the $X(3872)$ decays mostly via $D^0\overline{D}^{*0}$ (the branching ratio is about ten times higher than $J/\psi\pi^+\pi^-$).
Measuring the $X(3872)$ mass with the $D^{0*}\overline{D}^0$ decay is considerably more challenging then with $J/\psi\pi^+\pi^-$ for several reasons. If conceived as a bound or virtual $D^{0*}\overline{D}^0$ state, the X line-shape in this decay mode is determined by the binding energy, the D^{0*} natural width, and the natural width of the X itself, which is at least as large as the D^{0*} width. Because the binding energy of the X is less then $1\,MeV/c^2$, whether or not its mass peak is below $D^{0*}\overline{D}^0$ threshold, substantial fractions of the line-scape will lie both and below that threshold. The portion of the X line-scape below $D^{0*}\overline{D}^0$, by definition, can not decay to $D^{0*}\overline{D}^0$. In the $J/\psi\pi^+\pi^-$ decay mode these problem of threshold are not so important, because to the large amount of energy to produce the J/ψ and the πs.

4.5.1 The interpretations

Since the first observation it was very difficult to understand the real nature of the $X(3872)$, even if there were four different interpretation. The natural interpretation is that it is a charmonium state ($c\overline{c}$), the other hypothesis do not matched with expectations. A new theoretical interpretations of the XYZ state states that they could be new forms of matter such a quark-gluon hybrids, mesonic molecules and tetraquarks. A hint for the mesonic molecule is given by the fact that the mass of the particle is, within the errors, identical to the combined mass of the D^0 and D^{0*} mesons, figure 4.7.

Charmonium state

The interpretation of the X as a charmonium state was one of the first. Between the various possible states only few are interested and close to the real properties of the particle.
The 1^1D_2 and the 2^3P_1 are the only conventional states with the correct quantum numbers that are close enough to be associated with the $X(3872)$.

The 1^1D_2, with state η_{c2}, would assign the quantum numbers $J^{PC} = 2^{-+}$. But this decay is violating the isospin and one would expect to have a very tiny decay width into $J/\psi\pi^+\pi^-$. If the X were in this state, the radiative transition $1^1D_2 \to \gamma 1^3S_1$ would be highly suppressed: the observation of $X(3872) \to \gamma J/\psi$ disfavours the identification of the X as the 1^1D_2 state.

The 2^3P_1, with state χ'_{c1}, has the quantum number $J^{PC} = 1^{++}$ and the mass of $\sim 3930 - 4000\, MeV/c^2$, the expected width of this state is greater then $10\, MeV/c^2$. The problems rise from the observation of a new state, the $Z(3921)$, identified with the 2^3P_2 state, implying that the $2P$ mass is $\sim 3940\, MeV/c^2$. Identifying the $X(3872)$ with the 2^3P_1 also implies s spin splitting much larger than would be expected.

The other possibilities are excluded by the decay of the $X(3872)$ and its width. The $F-$wave states are neglected since they are expected to have mass greater then $4\, GeV/c^2$. All the considered states do not show a complete agreement with the observation properties of the $X(3872)$.

Molecule of particles

The close proximity of the PDG measure of the $X(3872)$, $3871.56 \pm 0.22\, MeV/c^2$, to the $m_{D^0} + m_{\overline{D}^{*0}}$ mass threshold, $3871.8 \pm 0.3\, MeV/c^2$, gives reason to the molecular interpretation.

The molecular hypothesis would also clarifies the apparent isospin breaking in the decay $X \to J/\psi\rho$. The difference in mass between the two Ds states is $\sim 8\, MeV/c^2$. The irregular isospin ($I = 0$) wave function of the state $((|D^0 D^{0*}\rangle + |D^+ D^{-*}\rangle)/\sqrt{2})$ shows the breaking because the contribution of the charged part is above threshold and suppressed. This concludes that the wave function of a molecular state is not an isospin eigenstate, and there is a contribution of the $I = 1$ state.

Theoretical studies of the bound state of D^0 and $\overline{D}^{0*}$ were done by Törnqvist in the 1994 and the prediction J^{PC} values are 0^{-+} and 1^{++} [37]. This model can also be useful for the bound state with the $b-$quark sector.

Törnqvist extended model, the Swanson one [38], adds a short range quark-gluon interaction to the long range pion exchange.

The radiative decays of the X ($\to \gamma J/\psi$ and $\to \gamma\psi(2S)$) favour the $c\bar{c}$ content. The most likely explanation is that the $X(3872)$ has more complicated structure, consisting of mixing with both 2^3P_1 and D^0D^{*0} components.

Further analysis on the width of the decay in the various channels would shed light on the real interpretation.

Tetraquark

Another proposed interpretation is that the $X(3872)$ particle is a tightly bound diquark-antidiquark four quarks state. This scenario predicts more nearly degenerate state not yet observed. The expected states, a orthogonal mixtures of $[cu][\overline{cu}]$ and $[cd][\overline{cd}]$ would be shifted in mass by $8 \pm 3\, MeV/c^2$. One suggestion is that these two different states might result in different $X(3872)$ masses in the decay chains: $B^{\pm} \to K^+\pi^+\pi^- J/\psi$ and $B^0 \to K^0\pi^+\pi^- J/\psi$.

Babar measured the X properties separately for this two channels and found a mass difference of $\Delta M = 2.7 \pm 1.6 \pm 0.4\, MeV/c^2$ that is consistent both with zero and the lower range of the theoretical prediction. CDF used its experimental resolution to measured the line width of $X(3872) \to J/\psi\pi\pi$ to establish a 95%CL upon experiment limit of $\Delta M < 3.6\, MeV/c^2$ for the equal production of the two states.

These results are not definitive test to this prediction. The statistical significance of the BaBar signal for $B^0 \to K^0 X(3872)$ is marginal (9.4 ± 5.2 events) and the CDF interpretation limit depends upon the unknown relative production strengths for the two different states.

In this scheme, the $X(3872)$ is $I_3 = 0$ member of an isospin triplet. The predicted states of this model are: $X^+ = [cu][\overline{cd}]$, $X^- = [cd][\overline{cu}]$ as charged states, and $X^0_u = [cu][\overline{cu}]$, $X^0_d = [cd][\overline{cd}]$ as neutral states. The two latter states are expected to be a mixture: $X_{low} = X^0_u \cos\theta + X^0_d \sin\theta$ and $X_{up} = -X^0_u \sin\theta + X^0_d \cos\theta$. The break of the isospin symmetry gives a mass difference of these two states of $\frac{7\pm2}{\cos(2\theta)}\, MeV/c^2$.

Since the dominant weak interaction process responsible for the decays $B \to KX(3872)$ is the isospin conserving $b \to c\bar{c}s$ transition, the charged $I_3 = \pm 1$ partner states, decaying in this mode $X^+ \to \rho^+ J/\psi$, are expected to be produced in B decays at a rate that is twice of the neutral state. BaBar studied the process $B \to K\pi^+\pi^0 J/\psi$ and placed upper limits on the product branching fractions for the $X^+ \to \pi^+\pi^0 J/\psi$ that are below isospin expectations.

There are not confirmations of this hypothesis, further study will shed light on this interpretation.

4.5.2 The charmonium production at LHC

The production of the charmonium state in the hadron colliders happens in three different ways.

Direct production: when a $c\bar{c}$ state is directly produced by the pp collision: $pp \to c\bar{c} + others$. The charm quarks in the final state could combined each others to form a J/ψ particles, or another charmonium state (like the $\psi(2S)$ or the $X(3872)$).

Feed-down: when the final observed state is the decay product of another heavier charmonium state. As example, the J/ψ particle in the $X(3872)$ decay chain: $pp \rightarrow c\bar{c}(\rightarrow J/\psi + other) + other$.
This two methods are also called *prompt* production mechanism, and they happen in the primary vertex of the collision.
Non-prompt production: when the state is produced by the decay of the particle with the b quark: $pp \rightarrow B(\rightarrow c\bar{c} + other) + other$. The relatively long live time of the b hadrons moves the vertex from the interaction point to few mm from the primary vertex. This allows the identification of the secondary vertex of the decay.

The models of the production

The Colour Evaporation Model (CEM) has been developed by Fritzch and others in the 1970s [39] [40], and has been reviewed by Amundson and others in the 1990 [41] [42]. The total cross section of the production is calculated integrating the cross section of the charmonium from the minimal value ($m_{c\bar{c}}$) to a pair of heavy-light mesons (m_D), the production occurs via multiple gluon interactions, evaporations. The output particles is predicted to be unpolarized. This model is not very interesting because of the weak predictive power and does not agree with data.
The charmonium production over a wide range environment (leptons and hadrons collisions and by photo-production) is given by the Colour Singlet Model (CSM), developed since the 1980 [43]. For example, in the CSM model the J/ψ is produced in two steps: at first the charmonium state is produced with a quantum number in a colour singlet state, and then it is calculated the binding of the $c\bar{c}$ into charmonium state. The CSM model can predict the radiative decay of the charmonium state, such the $\chi_{cJ} \rightarrow J/\psi + \gamma$. In principle it can also be applied for the $X(3872)$ case. The $X(3872)$ could decay into radiative way, as observed by Belle experiment [36]. An enhancement to the predicted cross section, at high p_T could arrive from the parton fragmentation (a dominant contribute to the prompt production) of the gluon (at higher order) or of the quark charm . The last one depends on the transverse momentum of the output particle.
Another way to compute the production is done by the Non Relativistic QCD, NRQCD [44]. This treats the quarkonium state as a non relativistic system. The production is achieved in two steps: the perturbative level generation and the evolution to colourless meson through a gluon emission at non perturbative domain. The $c\bar{c}$ is produced often as a colour octet state, this also gives the name of Colour Octet Mechanism (COM) to the model. The matrix elements used in this model calculations greatly increase the predictive power of the NRQCD and leave the calculation process independent.
The non-prompt production of the charmonium comes from the decay of B hadrons,

from interaction that produce a b quark. The next-to-leading order contributions can be classified into three classes: the gluon fusion (when the $b\bar{b}$ pair is produced separated by 180° in azimuthal range), the gluon splitting (produce b quarks close together) and the flavour excitation (from the gluon scattering, in this case the b quark goes in the same direction of the proton beams). After the b production the hadron decays in different way, included the way with a c quark with a particular branching ratio for every possible way [30].

Charmonium states decay

The charmonium state with $J^{PC} = 1^{--}$ have four possible ways to decay, as shown in figure 4.10.

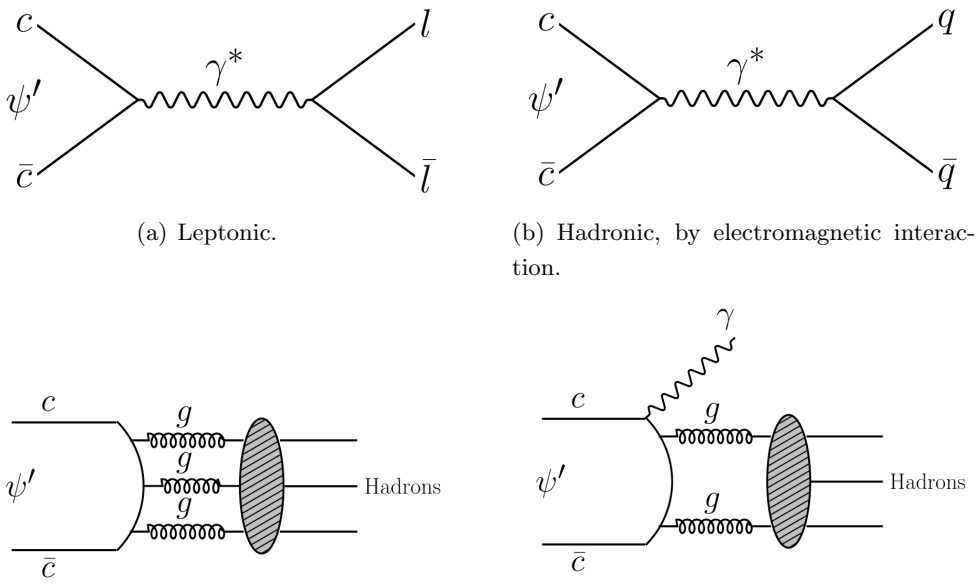

(a) Leptonic.

(b) Hadronic, by electromagnetic interaction.

(c) Leptonic, by strong interaction.

(d) Radiative.

Figure 4.10: Charm meson decay modes.

- *Leptonic decays*: the quark and antiquark pair annihilate to create a virtual photon and then the virtual photon produces a lepton antilepton pair, as example: $J/\psi, \psi(2S) \rightarrow \gamma^* \rightarrow l^+l^-$. Figure 4.10(a).

- *Hadronic decays*, by electromagnetic interaction: the quark and antiquark pair annihilate to create a virtual photon and then the virtual photon produces a quark antiquark pair. This pair fragments into a final state of hadrons, as $J/\psi, \psi(2S) \rightarrow \gamma^* \rightarrow hadrons$. Figure 4.10(b).

- *Hadronic decays*, by strong interaction: the quark and antiquark pair annihilate to three gluons, then these gluons fragments into a final state of hadrons, as: $J/\psi, \psi(2S) \rightarrow g + g + g \rightarrow hadrons$. Figure 4.10(c).

- *Radiative decays*: the quark and antiquark pair annihilate to a photon and two virtual gluons; the two gluons produce the final state hadrons, as $J/\psi, \psi(2S) \rightarrow \gamma + g + g \rightarrow \gamma + hadrons$. Figure 4.10(d).

In the hadronic decay one of possible final states made of pions. In particular, in the case of the charmonium state $\psi(2S)$ one accessible final state is this: $\psi(2S) \rightarrow J/\psi\pi^-\pi^+$.

5

Cross section measurement of the X(3872) with CMS

In this chapter it is presented the measurement procedure of the ratio of the cross sections of the $X(3872)$ and $\psi(2S)$. The evaluations of all the possible sources of errors are accounted and quantified. A possible way to reduce the background is also studied, the matching of the pions. Finally a first measurement of the non-prompt fraction is given.

5.1 The overview

The direct production of quarkonium states in the hadron collider, as LHC, is described in the framework of the NRQCD. The quantitative prediction of this theory for differential production cross section of $X(3872)$ have been achieved for both $p\overline{p}$ collisions at Tevatron and also pp collisions at the LHC.

As was found at the Tevatron, a hadron collider can provide a unique contribution to the study of this particle. The CMS detector and the large production rate allows to study the properties of the $X(3872)$. At the Tevatron the production of $X(3872)$ in $p\overline{p}$ collisions was found to be dominantly prompt, without the typical lifetime signature indicating the presence of B in the event. For the long lived fraction the value of $16 \pm 4.9\%$ was been calculated.

The goal of this analysis is the measurement of the ratio of the cross section of the $X(3872)$ to the $\psi(2S)$, in the proton proton collisions at $\sqrt{s} = 7\,TeV$. The decays observed are: $X(3872), \psi \to J/\psi\pi^+\pi^-$. The procedure is quite similar to that adopted in the Tevatron experiments, CDF and D0.

In a first step the J/ψ candidates are reconstructed utilizing their decay in two oppositely charged muons. The branching ration for this decay has the value of: $5.93 \pm 0.06\%$ [30].

In a second step two pions are paired to the J/ψ to reconstruct the $X(3872)$ and the $\psi(2S)$.

From the invariant mass spectrum the number of $X(3872)$ and $\psi(2S)$ signal events is determined, and used to calculate the ratio [45]:

$$\frac{\sigma(pp \to X(3872) + anything) \times BR(X(3872) \to J/\psi\pi^+\pi^-)}{\sigma(pp \to \psi(2S) + anything) \times BR(\psi(2S) \to J/\psi\pi^+\pi^-)} \tag{5.1}$$

in this way the systematics errors are mainly cancelled out. The uncertainties simplified in the ratio are those related to the triggering and reconstruction of the J/ψ mesons and the external normalization errors of the luminosity. The first is due to the efficiency of the muon reconstruction in the detector and the second is due to the measurement of the luminosity of LHC, this is one of the most important error in every physics analysis.
The remained systematics uncertainties arise from the pion spectra of the two states, because they are different for the $X(3872)$ and for the $\psi(2S)$, in transverse momentum and in the angular distribution of the particles.
In the measurement of the cross section ratio, the differences in acceptance and efficiency are accounted for by a factor determined by simulated events. In the future, a data driven method will be used to verify the accuracy of the simulations.
Another important issue to study is the prompt and no prompt components of the $X(3872)$. A first attempt will be shown in this thesis. Further analysis, less limited by statics, will permit to perform better measurement of these fractions.

5.1.1 Samples used

Computation in CMS experiment is made by a software developed for this particular issue, CMSSW: *CMS Software*. This program allows to manage all the informations stored for every event. In particular it permits to handle the track of the tracker and all the specific data from the devices of the detector. It also permits to build the vertex of a group of particles reconstructed in the various part of the detector.
The Monte Carlo samples and all the analysis are made using the release CMSSW_3_9_7. The simulation samples were produced using the PYTHIA6 [46] to generate the $\psi(2S)$ and $X(3872)$ samples and EvtGen [47] to force them to decay into the final $J/\psi\pi^+\pi^-$ channel. PYTHIA is a program developed for the study of the collision between particles, in this analysis it computed the production of the X and ψ from the pp collision at $\sqrt{s} = 7\,TeV$. PYTHIA generates the four vectors of the particles with all the conservation rules, from a precise collision process (pp in this case). These vectors are processed by the CMSSW software that is interfaced with another program, GEANT. This program simulates the interactions of the particles in the various detector layers and it produces an output with the same informations of a real event. In particular, in these programs it is used the same reconstruction mode of the real events. For example, the hit requested in the tracker are

the same simulated by the GEANT programs. In this way a complete simulation of the pp collision and a reconstruction of the particles is implemented in a set of programs. EvtGen is another program used to simulate the decays of the particles.
Since the properties of $X(3872)$ are not well understood, the simulation of its production is done using a known particle. To do this the particle more similar to the $X(3872)$ is the χ_{c1}: its quantum number are $J^{PC} = 1^{++}$, corresponding to those favoured for the $X(3872)$.
The Monte Carlo dataset produced are shown in table 5.1. In the simulated samples, events are selected according to the trigger: *HLT_DoubleMu0_Quarkonium_v1* (defined below). The "no prompt"components are obtained from the decay of the B meson.

Table 5.1: Monte Carlo samples used in the analysis.

Sample	**Cross section**$[pb]$	**Events**	**Lumin.**$[pb^{-1}]$
$X(3872)$ prompt	14672	1167177	434.8
$X(3872)$ NO prompt	950	1103543	6000
$\psi(2S)$ prompt	78959	974524	72.6
$\psi(2S)$ NO prompt	8617476	993447	191

The data are those collected in the 2010 data run A and run B, corresponding to an integrated luminosity of $36\,pb^{-1}$. The samples used are shown in table 5.2. The ranges

Table 5.2: Data samples used in the analysis.

sample	**run range**
MuOnia/Run2010A-Dec22ReReco_v1/RECO	$135821 - 144114$
MuOnia/Run2010A-Dec22ReReco_v1/RECO	$146240 - 149294$

used is selected in the correct machine runs, the list of all the correct run is stored in a so called: *JSON* file. It is a text file, with all the runs certificated by the group of shifters. The certification takes place at the data taking step. The "certified "data are those one collected when all detectors components relevant for the analysis are working well and they are calibrated.
The RECO format of data is produced applying several levels of pattern recognition and reduction algorithms to the RAW data. The RAW events contain the full recorded information from the detector, plus a record of the trigger decision. The algorithms used in the RECO include: detector specific filtering and correction of the digitised data; cluster and track-finding; primary and secondary vertex reconstruction and particle ID, using a variety of algorithms operating on cross detector information. The reconstruction step is the most CPU intensive activity in the CMS data processing chain. The resulting RECO

events contain high level physics object plus a full record of the reconstructed hits and cluster used to create them. The event size is around $0.5\,MB/event$.

5.1.2 Trigger and event selection

During the 2010 run the trigger evolved with the increasing instantaneous luminosity. A run-dependent trigger selection is applied to the data. The run range, the integrated luminosity and the trigger is shown in figure 5.3. where the *HLT_DoubleMu0* requires in

Table 5.3: Trigger used to select events.

Run range	**Trigger**	**Integr. Luminosity**$[pb^{-1}]$
$136033 - 147195$	*HLT_DoubleMu0*	8.7
$146240 - 149294$	*HLT_DoubleMu0_Quarkonium_v1*	31.3

the event two muons at the L3 trigger level, without a minimal p_T value. The *HLT_DoubleMu0_Quarkonium_v1* requires the same two muons but with different charges and the invariant mass of the muons system has to be in the window from $1.5\,GeV/c^2$ to $14.5\,GeV/c^2$.

5.1.2.1 $J/\psi \to \mu^+\mu^-$ selection

The selection of the J/ψ candidates events is done with two identified muon candidates: tracker muons or global muons [14]. Events are selected with two identified muons of opposite charge consistent with the invariant mass of the J/ψ meson ($3096.916 \pm 0.011\,MeV/c^2$[30]). In particular, the reconstructed inner tracks are required to have at least two hits in the pixel detector and at least twelve hits in the tracker system, pixel plus strip. The condition requested to the track fit of the inner tracker is to have $\chi^2/NDF < 1.8$. Additional quality criteria are imposed to remove mostly the duplicate muon, called ghost, coming from the same muon.
For the global muons it is required to leave at least one valid hit in the muon system. A valid hit is when a muon track leaves at least one hit in the muon chambers. The total fit to the inner tracker and the outer muon track yields must be $\chi^2/NDF < 20$. Finally the two muons are required to originate a common vertex with probability at least 0.01. The identified muons is also asked to match with the muons that triggered the event.
There are three kinematic regions in the CMS detector, in each of them there is a specific requirement imposed. In the barrel region, $|\eta| < 1.3$, the muons must have $p_T > 3.3\,GeV/c$; in the intermediate region, $1.3 < |\eta| < 2.2$ they must have $p > 2.9\,GeV/c$ and in the endcap region they must have $p_T > 0.8\,GeV/c$. Where p is the momentum, p_T is the transverse momentum and $\eta = -\ln[\tan(\theta/2)]$ (θ is the polar angle measured from the $z-$axis which points along the counter clockwise beam direction) is the pseudorapidity of the muons.

These cuts are selected to permit at the muons to be within the detector acceptance. The muon has to be in the acceptance of the detector and is then chosen so as to guarantee a single-muon detectability exceeding 10% [14]. About 2 millions J/ψ are found. In the figures 5.1, 5.2(a) and 5.2(b) are shown the properties of these candidates. No explicit cuts on the J/ψ kinematics are applied.

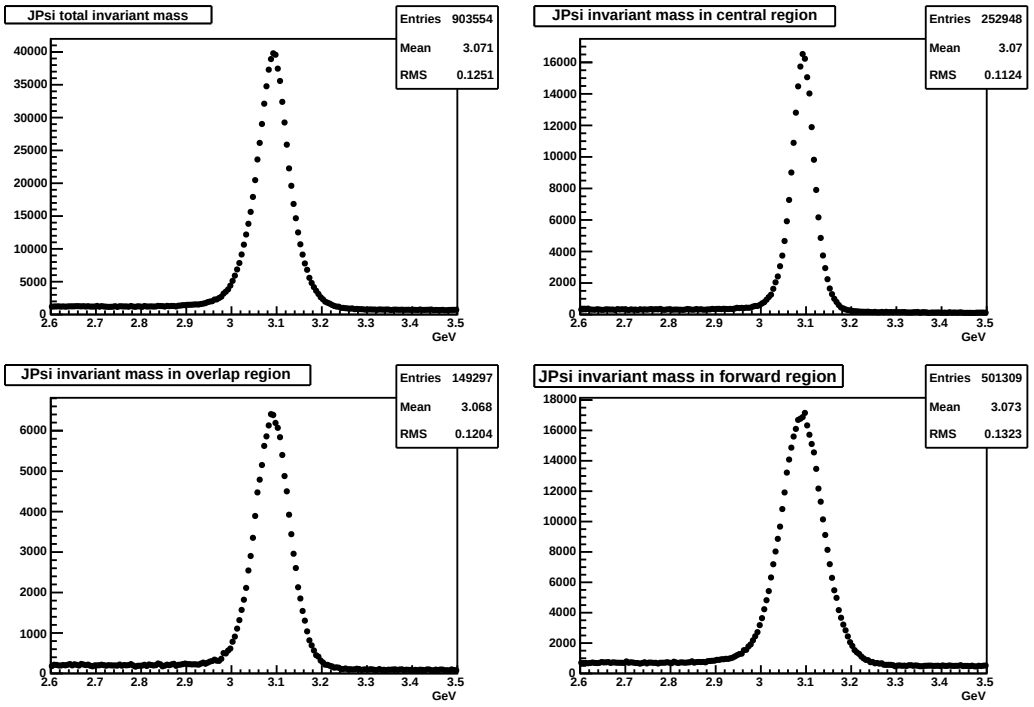

Figure 5.1: The invariant mass distribution, measured in the data (where GeV is meant to be GeV/c^2), of the two opposite charged muons after the selection cuts for the J/ψ, in the full range of rapidity (top left), and separately for the three different ranges of rapidity: central $|y| < 1.3$ (top right), overlap $1.3 < |y| < 2.2$ (bottom left), forward $2.2 < |y| < 2.4$ (bottom right).

5.1.2.2 $J/\psi \to \mu^+\mu^-\pi^+\pi^-$ selection

In order to select the J/ψ candidate for further analysis, the invariant mass in three rapidity regions has been fitted with two functions (Crystal Ball and Gaussian). A window is defined in order to keep at least 99% of the signal, table 5.4.
The Crystal Ball function has the form of:

$$f(n) = \begin{cases} e^{-\frac{(m-\mu)^2}{2\sigma^2}} & \text{for } \frac{m-\mu}{2\sigma} > \alpha \\ A \times (B - \frac{m-\mu}{\sigma})^{-n} & \text{for } \frac{m-\mu}{2\sigma} \leq \alpha \end{cases}$$

$$\text{where: } A = (\frac{n}{|\alpha|})^n \times e^{\frac{|\alpha|^2}{2}} \text{ and } B = \frac{n}{|\alpha|} - |\alpha|$$

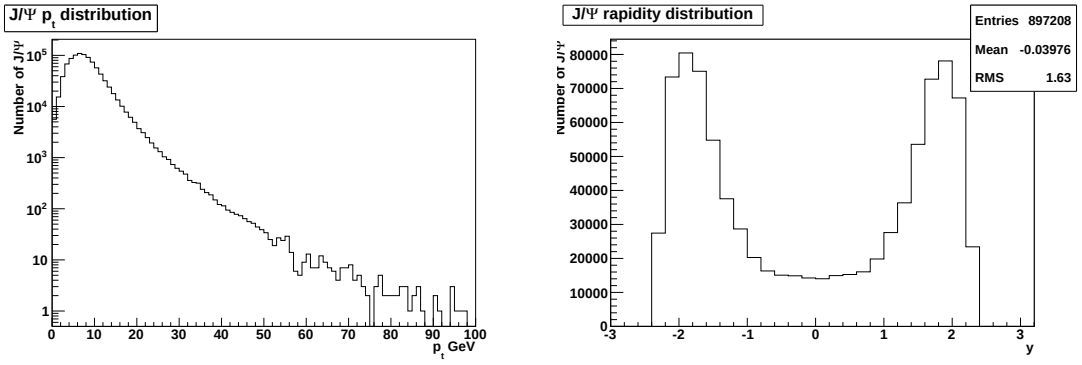

(a) J/ψ p_T distribution (where GeV is meant to be GeV/c).

(b) J/ψ y, rapidity distribution.

Figure 5.2: Kinematic characteristics for the J/ψ candidates as measured in data.

Table 5.4: J/ψ mass selection.

$\lvert y\rvert$ **range**	**Weighted** $\sigma[MeV]$	J/ψ **mass range** $[MeV]$
$\lvert y\rvert < 1.3$	29	$3019 - 3167$
$1.3 < \lvert y\rvert < 2.2$	42	$2981 - 3198$
$2.2 < \lvert y\rvert < 2.4$	51	$2959 - 3221$

After the reconstruction of the J/ψ meson candidate, pair of opposite charge pions are searched for. A refit of the four tracks is performed, constrained to originate from the same vertex and the dimuon system to have the mass of the J/ψ.
Pion tracks are required to have at least two hits in the pixel tracker detector, and five hits in the strip detector [48] [49]. In the figure 5.3 is shown the distribution of hits of the pion tracks on the data.

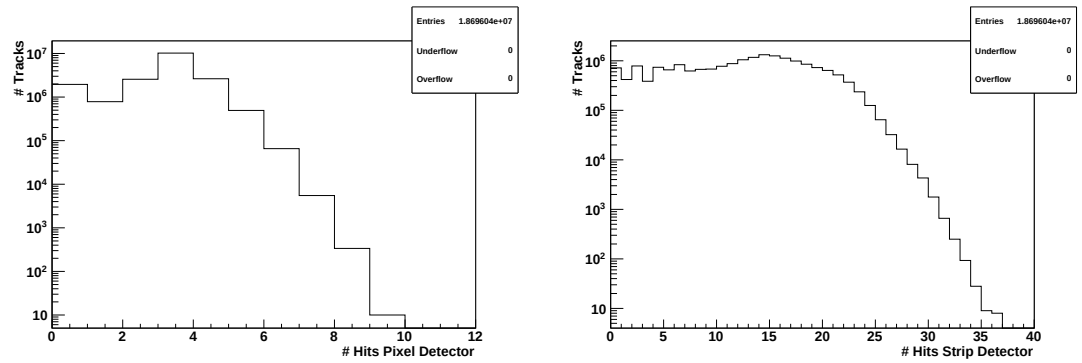

(a) Pixel hits distribution.

(b) Strip hits distribution.

Figure 5.3: Distribution of the hits of the pion tracks on measured data. Left: Pixel and right: strip.

The transverse momentum of the pions, before the four tracks refit, is required to be larger than 400 MeV/c. The pion tracks kinematically matching with the muon tracks are removed. In this case, if the pion track is very close in space and in kinematic values to the muon track it is discarded. If the $\frac{|p^{\mu^{rec}} - p^{\pi}|}{p^{\mu^{rec}}} < 0.1$ (where p is the momentum of the tracks) and $\Delta R(\mu^{rec} - \pi) < 0.5$ the tracks are the same, and have been discarded. The charge of the two pions is required to be opposite. In the figure 5.4 is shown the pions p_T (separately, the one with higher and the one with lower), after the four track refit.

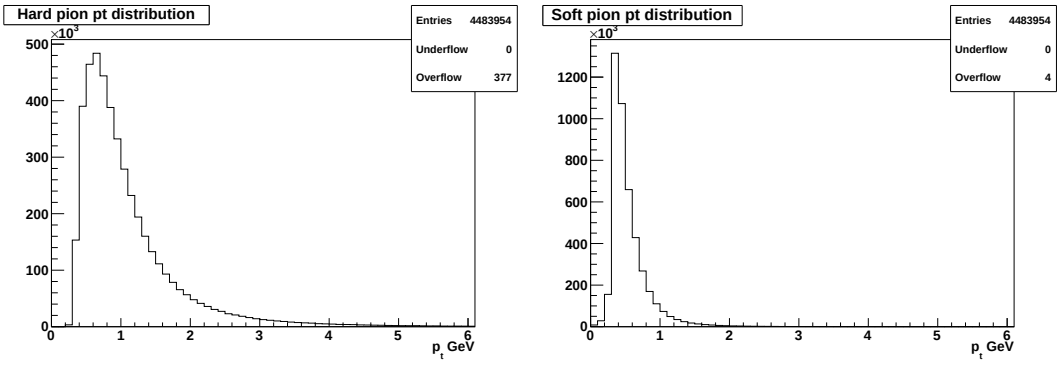

Figure 5.4: Distribution of p_T pions as measured in data (where GeV is meant to be GeV/c).

The invariant mass of this system, $\mu^+\mu^-\pi^+\pi^-$ is required to be smaller than 5 GeV/c^2. The four vertex fit probability is required to be larger than 0.01 in order to reduce the combinatorial background coming from tracks originating from different vertices. The probability of the vertex is shown in figure 5.5.

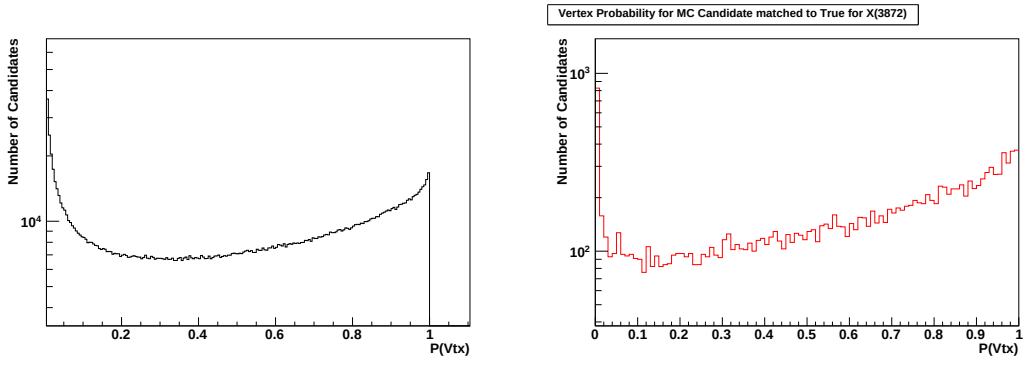

(a) Data (b) Monte Carlo signal

Figure 5.5: Vertex probability of the four track system.

The distribution is not flat because the errors from the track fits are not correctly evaluated. With all of these cuts the remaining candidates have the transverse momentum

distribution of the pions pair and its opening angular distribution ΔR[1] as shown in figure 5.6.

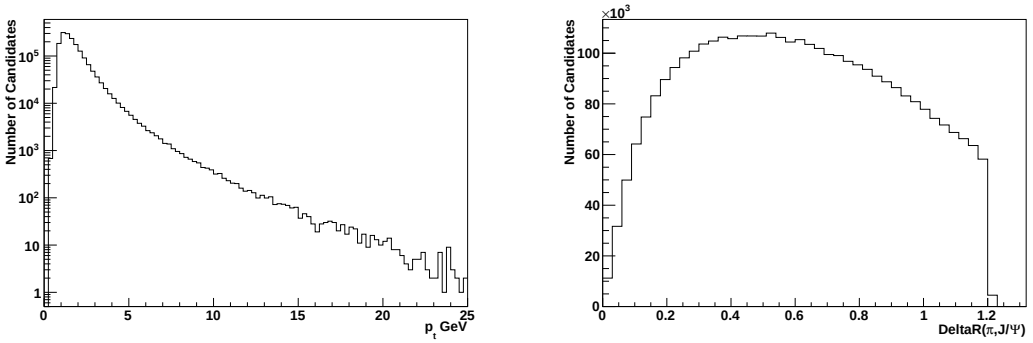

(a) $p_T(\pi^+\pi^-)$ (where GeV is meant to be GeV/c) (b) ΔR between J/ψ and $(\pi^+\pi^-)$.

Figure 5.6: Characteristics of the $(\pi^+\pi^-)$ system as measured in data.

The truncation of the ΔR distribution is related to the preselection cuts $\Delta R < 1.2$ between the original tracks and the J/ψ candidate.
ΔR distribution shown in figure 5.7 is done separately for the mass window and in the sidebands region (see below in section 5.1.7). The sideband entries are scaled to correct the difference in the width of the sidebands.

The lower plots of the figure 5.7 show the difference between the signal and the sidebands distributions. Data are compared to the Monte Carlo, which is normalized to the data. From these figures, a cut on $\Delta R < 0.7$ is applied.
The $p_T(\pi^+\pi^-)$ distributions for signal and background (from Monte Carlo) are shown in figure 5.8: to minimize the combinatorial background, increasing the signal over background ratio for the X signal $p_T(\pi^+\pi^-) > 1.5\,GeV/c$ is applied. These additional cuts reduce the data sample of a factor ~ 40, while retaining about 85% of the signal events.
Another variable under study was the mass of the dipion system. With this it could be possible to discriminate the resonance of this system, expected to be a ρ particle, with mass $775.49 \pm 0.34\,MeV/c^2$ [30]. But there is not a real huge contribution to the signal over background, so it is not used in the analysis.

5.1.2.3 Acceptance and efficiency

The acceptance reflects the finite geometrical coverage of the CMS detector and the limited kinematic reach of the muon trigger and reconstructions systems, constrained by the thickness of the material in front of the muon detectors and by the track curvature in the magnetic field. For example, the acceptance of the J/ψ meson is defined as the fraction of

[1] $\Delta R = \sqrt{(\Delta\eta)^2 + (\Delta\phi)^2}$, where η is the pseudorapidity and ϕ is the angle between the particles.

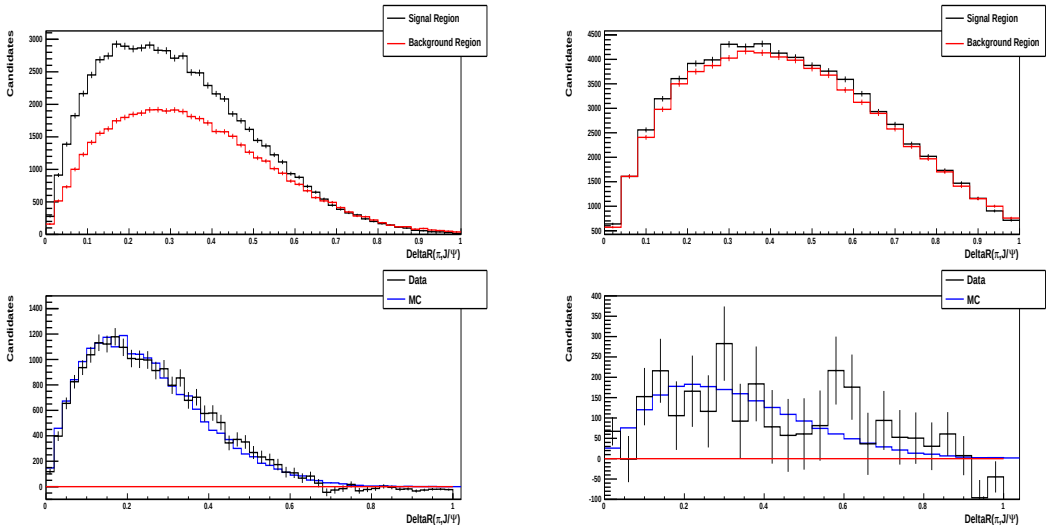

(a) $\psi(2S)$ (b) $X(3872)$

Figure 5.7: The ΔR between the pion pair and the J/ψ for the mass interval (black) and the sidebands (red). For the $\psi(2S)$ (left) and $X(3872)$ (right).
The bottom histograms show the mass window distributions after subtraction of the distribution from the sidebands (black) and the Monte Carlo simulation scaled to the number of entries in the data (blue).

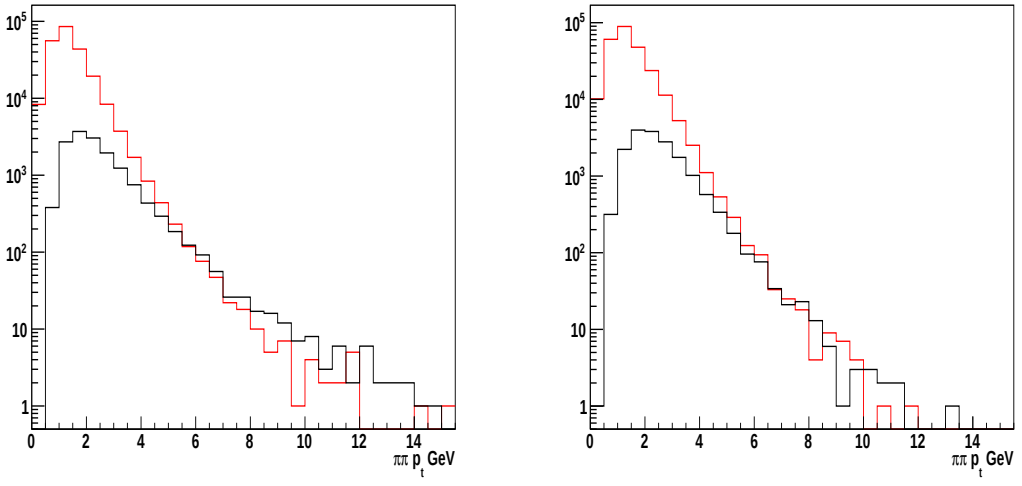

(a) $\psi(2S)$ (b) $X(3872)$

Figure 5.8: $p_T(\pi^+\pi^-)$ distributions from Monte Carlo for signal (black) and background (red) (where GeV is meant to be GeV/c).

detectable muon $J/\psi \to \mu^+\mu^-$ decays, as a function of the dimuon transverse momentum and rapidity:

$$A(p_T; y) = \frac{N_{det}(p_T; y)}{N_{gen}(p_T; y)}$$

where N_{det} is the number of detectable J/ψ events in a given $(p_T; y)$ bin and N_{gen} is the corresponding total number of generated J/ψ events in the simulation.
The efficiency is defined as the ratio of the passed events over the total generated events, in the acceptance region.
These definitions can be applied at the $X(3872)$ and $\psi(2S)$, either for the J/ψ and for the pions pair ($\pi^+\pi^-$). The corrected signal yield can be factorized into four components. $A_{J/\psi}$ and $\epsilon_{J/\psi}$ are the acceptance and the efficiency for the J/ψ reconstruction. Similarly, $A_{\pi\pi}$ and $\epsilon_{\pi\pi}$ are the acceptance and efficiency of the pion pair. The final correction value is:

$$C = \frac{A_{J/\psi}(X(3872)) \times \epsilon_{J/\psi}(X(3872)) \times A_{\pi\pi}(X(3872)) \times \epsilon_{\pi\pi}(X(3872))}{A_{J/\psi}(\psi(2S)) \times \epsilon_{J/\psi}(\psi(2S)) \times A_{\pi\pi}(\psi(2S)) \times \epsilon_{\pi\pi}(\psi(2S))} \tag{5.2}$$

The ratio of each of the four components and their product, due to the similar properties of the particles, is close, but not equal, to the unity.
The first term $A_{J/\psi}(X(3872))$ is shown in figure 5.9, as a function of the p_T and the rapidity. Sufficiently large acceptance is found in the kinematic region of: $p_T(X) > 8\,GeV/c$ for $|y(X)| < 2.2$. This region is chosen for the measurement.

The ratio of the $A_{J/\psi}$ terms of the $X(3872)$ and $\psi(2S)$ in this kinematic region is close to the unity. It is steeply decreasing at the smallest values of p_T and $|y|$ with an average value of, for the ratio between the prompt production of the particles, $A_{J/\psi} 0.876 \pm 0.002(stat.)$. The result is shown in figure 5.10.

In the figure 5.11 the distributions of the prompt component of the $X(3872)$ are shown: for all simulated candidates and after subsequent cuts, after the application of the kinematic cuts on the decay muons from the J/ψ. The cuts are the same of before: $p_T(X) > 8\,GeV/c$ for $|y(X)| < 2.2$, and the selection cuts on the $J/\psi\pi^+\pi^-$ system.
The same study has been performed for simulated events of non-prompt $X(3872)$ and $\psi(2S)$. The yield is very similar, with prompt to non-prompt ratio of 0.97 ± 0.01 for $\psi(2S)$ and 0.94 ± 0.01 for $X(3872)$. The ratio: $A_{J/\psi}(X)/A_{J/\psi}(\psi)$ for prompt e non prompt simulations is found to be: $0.91 \pm 0.01(stat.)$.
The term $\epsilon_{J/\psi}$ accounts the efficiency of the reconstruction and of the trigger. The ratio for the prompt component is $0.842 \pm 0.007(stat.)$, it is shown in figure 5.12. Using the non-prompt component the ratio is 0.94 ± 0.01.

The ratio $(A_{\pi\pi}(X) \times \epsilon_{\pi\pi}(X))/(A_{\pi\pi}(\psi) \times \epsilon_{\pi\pi}(\psi))$ of the number of reconstructed $X(3872)$ and $\psi(2S)$ candidates, inside the J/ψ acceptance region, is determined from Monte Carlo

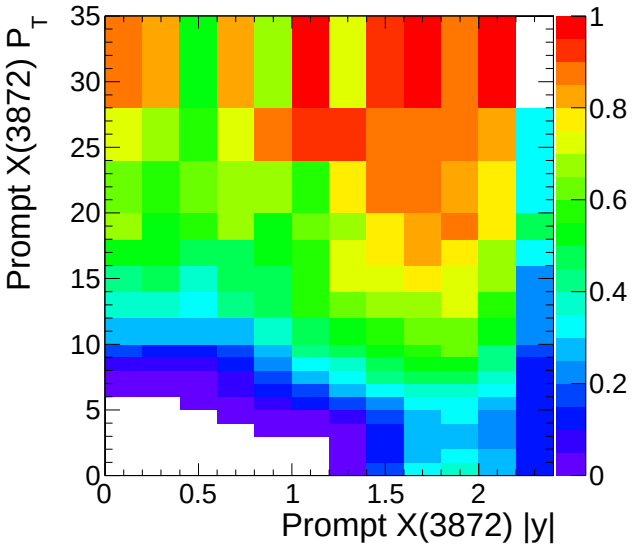

Figure 5.9: Acceptance map $A_{J/\psi}(X(3872))$, function of p_T and $|y|$ (where p_T is in GeV/c), for only the prompt produced $X(3872)$

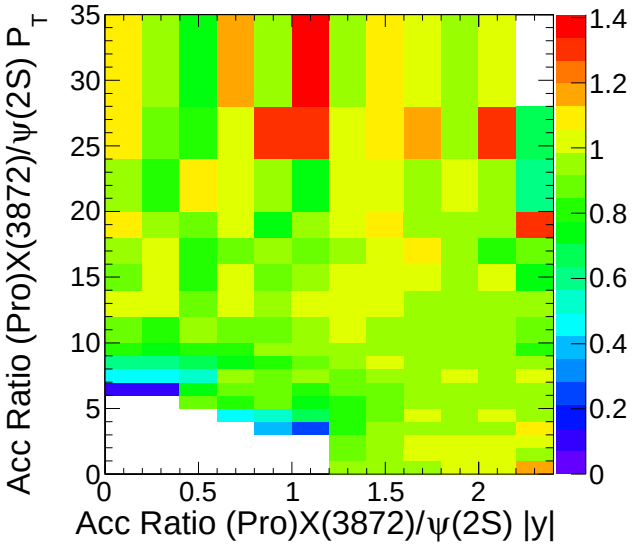

Figure 5.10: Ratio between the acceptance maps for the prompt component of $X(3872)$ and $\psi(2S)$

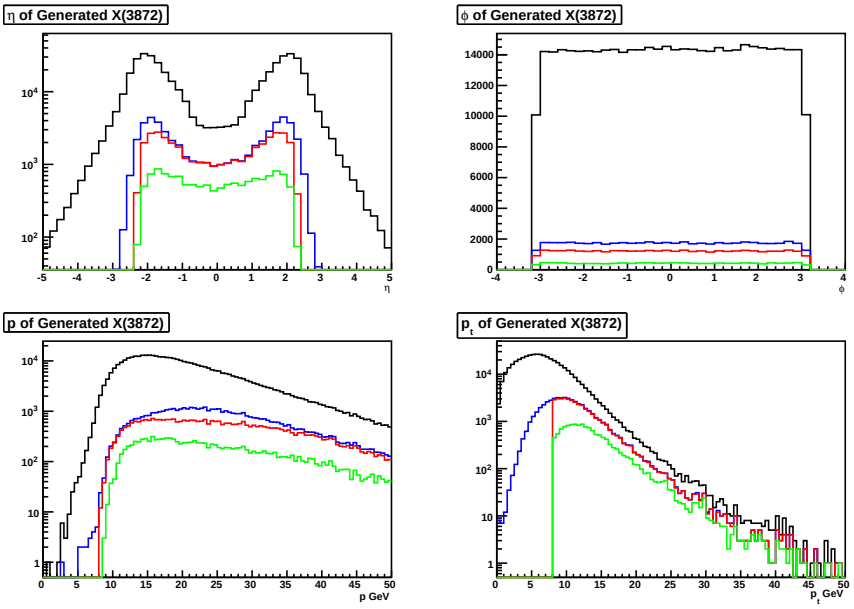

Figure 5.11: Acceptance and efficiency of the $X(3872)$ candidates as function of η, ϕ, p and p_T (where GeV is meant to be GeV/c for the p and p_T).
Black line: all candidates; Red line: sample after cuts of transverse momentum and rapidity ($p_T > 8\,GeV/c$ and $|y| < 2.2$); Green line: sample of candidates for which the $X(3872)$ is successfully reconstructed.

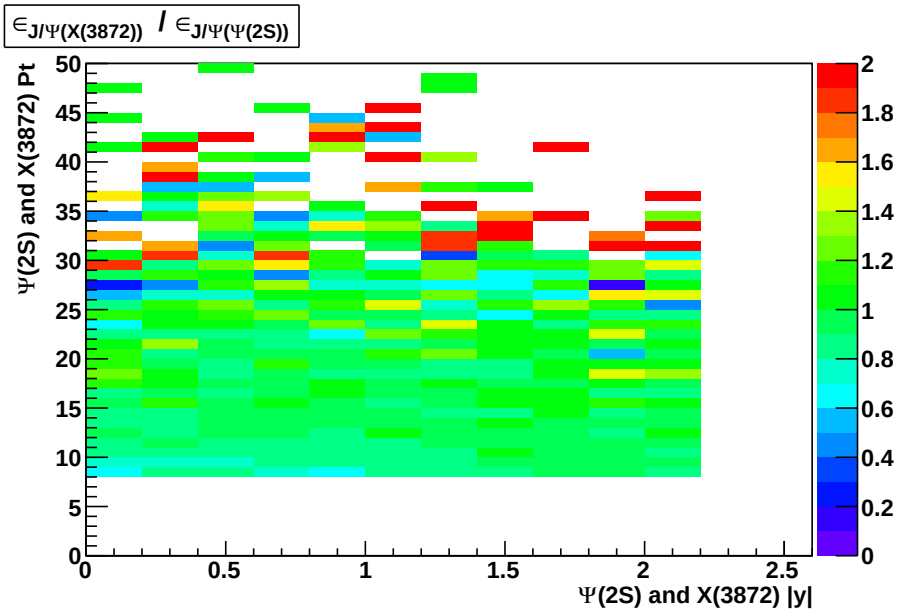

Figure 5.12: Ratio between $\epsilon_{J/\psi}$ for the prompt component of $X(3872)$ and $\psi(2S)$.

samples of true $X(3872)$ and $\psi(2S)$ candidates extracting the number of truth matched particles after all cuts divided by the number of true X and ψ with a reconstructed J/ψ

Table 5.5: Signal yields and acceptance and efficiency for $\psi(2S)$ and $X(3872)$ in the Monte Carlo samples. The **N pass** are the events passing that particular cut.

Part.	**Yield**	**N pass** J/ψ **cut**	**N pass** $J/\psi + \pi\pi$ **cuts**	$A_{\pi\pi}$	$\epsilon_{\pi\pi}$	$A_{\pi\pi} \times \epsilon_{\pi\pi}$
$X(3872)$	13398	36529	21233	0.581 ± 0.005	0.631 ± 0.007	0.367 ± 0.004
$\psi(2S)$	11543	34540	17918	0.519 ± 0.003	0.644 ± 0.006	0.334 ± 0.004

candidate, after trigger. The result is: $(0.367 \pm 0.004)/(0.334 \pm 0.004) = 1.098 \pm 0.016$. The table 5.5 contains numbers for the prompt component in the Monte Carlo samples, where this term has also been divided in the acceptance term. For the non-prompt component this term is found to be 1.199 ± 0.017.

The correction factor, 5.2, is obtained by multiplying the ratio for the different terms. Prompt component: $A_{J/\psi} = 0.876$, $\epsilon_{J/\psi} = 0.842$ (is the efficiency of reconstructing J/ψ) and $A_{\pi\pi} \times \epsilon_{\pi\pi} = 1.098$, the correction factor is: $0.809 \pm 0.014(stat.)$. For the non-prompt component is: $0.990 \pm 0.018(stat.)$. An assumption of the non-prompt component fraction is obtained using a $B-$enriched sample with a further selection based on $c\tau > 0.1\,mm$ in the transverse plane (see later for a better explanation).

5.1.3 Measurement of the non-prompt component

The measurement of the fraction of $X(3872)$ coming from the decay of $b-$hadrons it is used the $c\tau$ variable, also know as proper decay length, l_{xy}. It is defined as follows:

$$l_{xy} = L_{xy} \times \frac{m}{p_T}$$

where m and p_T are the mass and the transverse momentum of the examined particle ($X(3872)$ and $\psi(2S)$) and L_{xy} is the most probable decay length in the laboratory frame, in the $x - y$ plane. And the L_{xy} is defined as:

$$L_{xy} = \frac{\mathbf{u}^T \cdot \sigma^{-1} \cdot \mathbf{x}}{\mathbf{u}^T \cdot \sigma^{-1} \cdot \mathbf{u}}$$

where $\mathbf{x}$ is the vector joining the vertex of the decay and the primary vertex of the event in the transverse plane, $\mathbf{u}$ is the unit vector of the particle p_T, and σ is the sum of the primary and secondary vertex covariance matrices [14]. In figures 5.13 and 5.14 there are the L_{xy} and $c\tau$ distribution of the vertex in Monte Carlo samples. The distributions in the data is shown in figure 5.15. The distributions of that variables in the prompt Monte Carlo sample is very symmetric, reflecting the experimental resolution. The non-prompt in very

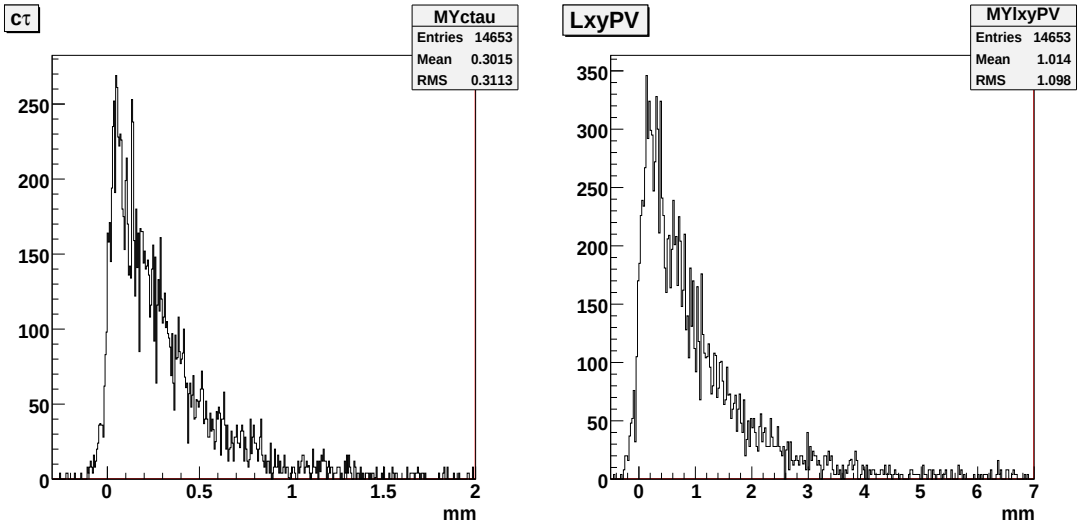

(a) $c\tau$ (b) L_{xy}

Figure 5.13: L_{xy} and $c\tau$ distributions in the $X(3872)$ non-prompt Monte Carlo samples.

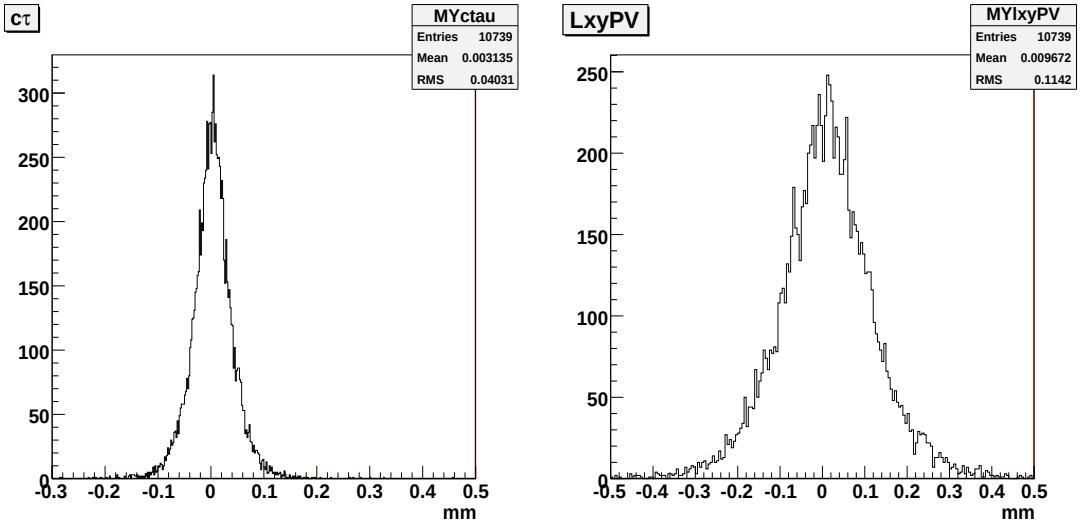

(a) $c\tau$ (b) L_{xy}

Figure 5.14: L_{xy} and $c\tau$ distributions in the $X(3872)$ prompt Monte Carlo samples.

asymmetric, this is due to $b-$hadron lifetime that has an average value of $\sim 1.6\,ps$. In the data the shape of the distributions is a mix of the non-prompt and prompt components.

To calculate the non-prompt component this system of equations is used:

$$\begin{cases} N(cuts + c\tau) = N_{non-prompt} \cdot B_{non-prompt} + N_{prompt} \cdot P_{prompt} \\ N(cuts) = N_{non-prompt} + N_{prompt} \end{cases} \tag{5.3}$$

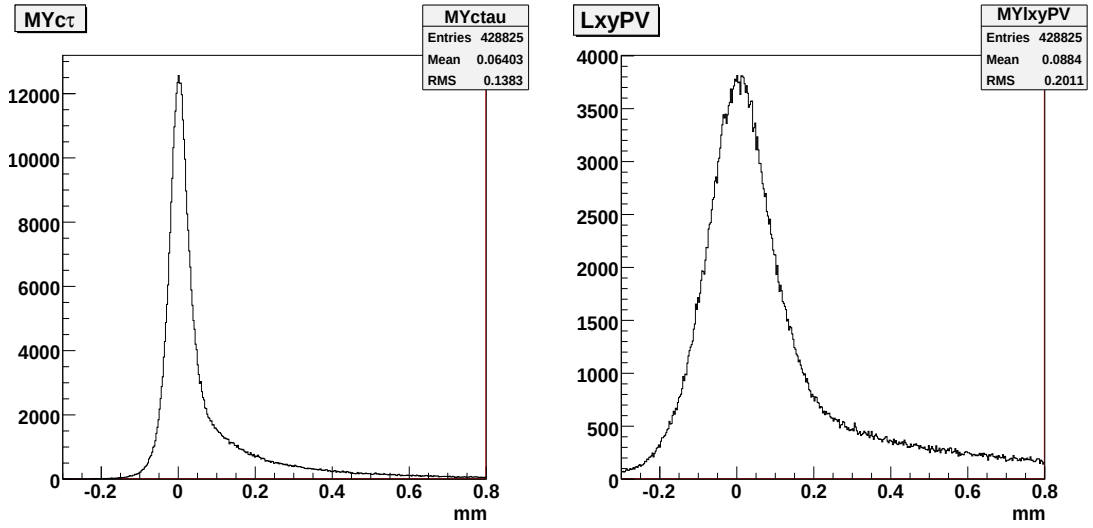

(a) $c\tau$ (b) L_{xy}

Figure 5.15: L_{xy} and $c\tau$ distributions in the data.

where: $N(cuts)$ is the events passing all the cuts, $N(cuts + c\tau)$ is the number of events passing all the cuts plus the $c\tau > 0.1\,mm$ cut. They are obtained from the 2010 data. The $B_{non-prompt}$ is the efficiency of the $c\tau > 0.1\,mm$ cut for the non-prompt sample. The $P_{non-prompt}$ is the efficiency of the $c\tau > 0.1\,mm$ cut for the prompt sample. Solving this system gives the ratio of the prompt and non-prompt component in the data, using the Monte Carlo efficiencies. The system can be used for both the $X(3872)$ and $\psi(2S)$. The results are shown in table 5.6.

Table 5.6: Efficiencies from the Monte Carlo samples.

name	**Value**
P_X	0.0144 ± 0.0010
B_X	0.7216 ± 0.0033
P_ψ	0.0109 ± 0.0010
B_ψ	0.7229 ± 0.0032

The calculation for the $\psi(2S)$ gives $N^{non-prompt}_{\psi(2S)}/N_{\psi(2S)}(cuts) = 0.488 \pm 0.023(stat.)$ of the non-prompt component of the $\psi(2S)$. For the $X(3872)$ the result is $N^{non-prompt}_{X(3872)}/N_{X(3872)}(cuts) = 0.41 \pm 0.18(stat.)$. The result obtained for the $\psi(2S)$ is in agreement with that obtained from a study of the $\psi(2S) \to \mu^+\mu^-$, in the same momentum range $\sim 15\,GeV/c$, as presented by CMS at the EPS2011 conference [50].
The non-prompt fraction is about the 45% for both $X(3872)$ and $\psi(2S)$ candidates. The overall correction factor in the scenario with $\sim 45\%$ of non-prompt component for both X

and ψ is:

$$C = 0.908 \pm 0.014(stat.) \tag{5.4}$$

Variations of the non-prompt fraction are considered to estimate the systematic uncertainty.

The ratio of the signal yields is computed from the $J/\psi\pi^+\pi^-$ invariant mass spectrum, in the kinematic region in which the $X(3872)$ candidate has $p_T > 8\,GeV/c$ and $|y| < 2.2$. The resultant mass spectrum, after all the cuts, is shown in figure 5.16. The signals of $\psi(2S)$ and $X(3872)$ are clear.

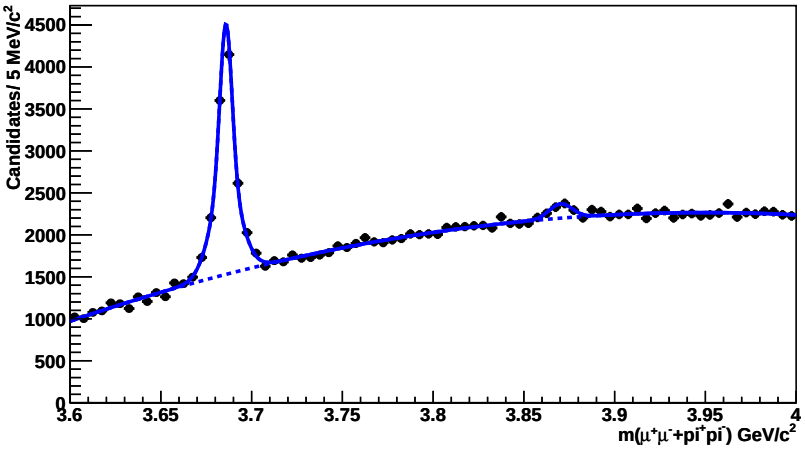

Figure 5.16: $J/\psi\pi^+\pi^-$ invariant mass spectrum in the region where the candidates have $p_T > 8\,GeV/c$ and $|y| < 2.2$. The curve represents the unbinned log likelihood fit.

To extract the number of candidates, an unbinned log likelihood fit is performed to the invariant mass spectrum of the $J/\psi\pi^+\pi^-$ range from $3.6\,GeV/c^2$ to $4.0\,GeV/c^2$, with an average of 2.4 candidates for an accepted event.
The $\psi(2S)$ signal is parametrized using a double Gaussian function, the $X(3872)$ signal is fitted with a single Gaussian. A second order Čebyšëv polynomial is used for the background.
The Čebyšëv polynomial is defined as follow:

$$T(x; c_0, \ldots, c_n) = \frac{1}{N} \times (T^0(x) + \sum_{k=0}^{n} c_k T^k(x))$$

where $T^k(x)$ is the k^{th} order Čebyšëv polynomial, starting form the easiest case ($T(0) = 1$) to higher order.

Table 5.7: Parameters from the fit to the invariant mass spectrum.

Parameter	Value
$m(\psi(2S))$	3.6859 ± 0.0001
$\sigma 1(\psi(2S))$	0.0081 ± 0.0006
$\sigma 2(\psi(2S))$	0.0033 ± 0.0002
$m(X(3872))$	3.8703 ± 0.0017
$\sigma(X(3872))$	0.0065 ± 0.0015
$c1$	0.349 ± 0.005
$c2$	-0.117 ± 0.005
$N(\psi(2S))$	7460 ± 162
$N(X(3872))$	542 ± 121
$N(\text{bkg})$	150985 ± 412
χ^2	0.693

The statistical error on the $X(3872)$ is about 20%. The table 5.7 contains all the parameters of the unbinned fit. To extract roughly non-prompt component fraction, a $B-$enriched sample is collected requiring the candidate's $c\tau > 0.1mm$, in the transverse plane. The mass spectrum of this case is shown in figure 5.17. The fit parameters are in the table 5.8.

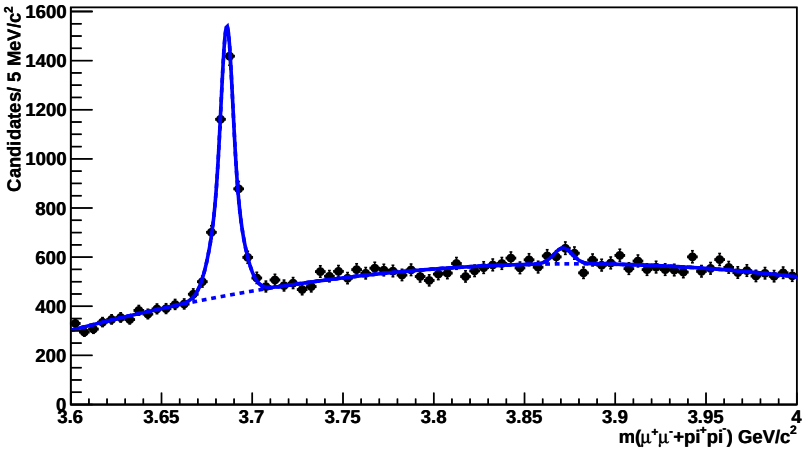

Figure 5.17: $B-$enriched sample: $J/\psi\pi^+\pi^-$ invariant mass spectrum in the region where the candidates have $p_T > 8\,GeV/c$ and $|y| < 2.2$. The curve represents the unbinned log likelihood fit. The fit parameters are in table 5.8.

5.1.4 Systematic uncertainties

Uncertainties correlated between $X(3872)$ and $\psi(2S)$ are distinguished from the uncorrelated ones. The correlated systematic errors cancel out in the ratio of the acceptance corrected signal yields. A table of all the contribution is shown in 5.9. The following uncertainties is been calculated and described.

Table 5.8: Parameters from the fit to the invariant mass spectrum before the $c\tau > 0.1\,mm$.

Parameter	Value
$m(\psi(2S))$	3.686 ± 0.0002
$\sigma1(\psi(2S))$	0.0073 ± 0.0029
$\sigma2(\psi(2S))$	0.0030 ± 0.0021
$m(X(3872))$	3.8712 ± 0.0027
$\sigma(X(3872))$	0.005 ± 0.0019
$c1$	0.227 ± 0.009
$c2$	-0.146 ± 0.009
$N(\psi(2S))$	2689 ± 109
$N(X(3872))$	163 ± 58
N(bkg)	40731 ± 230
χ^2	0.633

Table 5.9: Table of systematic uncertainties.

Track finding efficiency of pions	4%
Signal extraction	5.3%
Non-prompt fraction	6.0%
$X(3872)$ p_T shape	3.5%
MC statistics	1.8%
Full systematic error:	10%

Signal and background parametrization: signal and background parametrization are varied as follow. Background: third and fourth order Čebyšëv polynomial and a fourth "regular"polynomial is used. Signal: Voigtan function is used for the $\psi(2S)$ peak, other function failed in this goal. The maximum difference between the standard result and the values obtained changing the PDFs is assigned as systemic uncertainty. For the $\psi(2S)$ yield it amounts to 10%, with the Voigtan function. In the yields ratio, (also for the $X(3872)$ itself) the largest difference is found when using the fourth order regular polynomial and it amounts to 5.3%, 5.4% for the itself case.

Reconstruction efficiency of pion: according to the Monte Carlo simulation, the efficiency for the successful reconstruction of a single pion track, with at least two pixel and five strip hits and a transverse momentum of $400\,MeV/c$ is $\sim 70\%$. In this similar kinematic region, the absolute uncertainty on the efficiency to reconstruct a single pion track successfully has been measured to be 3.9% (see [51] and section 5.1.5). For the measurement of the cross section ratio, the uncertainty on the track finding efficiency is expected to cancel in part. The uncertainty on the ratio is conservatively estimated to be 4%.

Prompt Non-prompt compositions: in the $X(3872)$ and $\psi(2S)$ samples the combinations of the prompt non-prompt component are $\sim 20\%/40\%$, results in a 6% difference with re-

spect to the cross section ratio obtained with the assumption of 30% non-prompt fraction. This is a systematic uncertainty (see above).

Production mechanism: the production mechanism is unknown and the p_T dependence of the result is evaluated modifying the prompt $X(3872)$ distribution of p_T. A function based on the normalized p_T spectrum coming from PYTHIA is used to extract an event by event weight. On the basis of this weight all the correction factor are recalculated. In figure 5.18(a) the final effect of applying an opportune third grade polynomial or its inverse to the original Monte Carlo. In figure 5.18(b) there is the ratio between the new shape and the original one, showing variations from -50% to $+250\%$. The result applying this method are summarized in table 5.10, the maximum difference is of 7%. Half of the difference is assigned as a systematic uncertainty, yielding a systematic error of 3.5%.

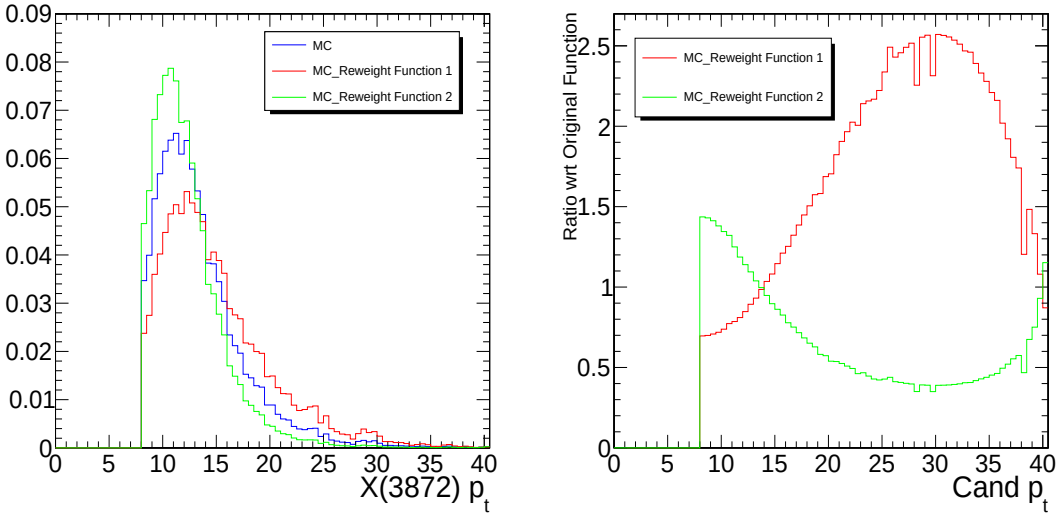

(a) Blu: p_T distribution in Monte Carlo and variations due to re weighting using a: red, polynomial and green, its inverse. The p_T is measured in GeV/c.

(b) Ratio of the two new shapes and the original one. The p_T is measured in GeV/c.

Figure 5.18: Reconstructed $X(3872)$ p_T distribution.

Monte Carlo uncertainty: the uncertainty introduced by statistical effects due to limited size of the Monte Carlo samples has been estimated to be 1.8%. It is largest in the determination of the efficiency and acceptance of the pion pair.

Trigger selection: in the kinematic range under study the trigger selection efficiency for both $X(3872)$ and $\psi(2S)$ is very high and, when calculating the ratio, the uncertainty originating from the trigger selection is small.

In total, the relative systematic error on the cross section ratio is estimated to be 10%. This is significantly smaller than the statistical uncertainty.

Table 5.10: Parameters obtained from the fit to the invariant mass spectrum.

	Function 1	**Function** 2
J/ψ Acceptance Ratio	0.835 ± 0.002	0.857 ± 0.002
J/ψ Efficiency Ratio	0.968 ± 0.009	1.076 ± 0.009
$A_{\pi\pi} \cdot \epsilon_{\pi\pi}$	1.08 ± 0.02	0.95 ± 0.01
C Total	0.873 ± 0.015	0.877 ± 0.018
$(X(3872))/\psi(2S)$ Final ratio	0.085 ± 0.016	0.087 ± 0.016
Difference From Central Value	-7%	-5.3%

To learn more confidence on the result, a cut variation study is performed, in which each of the following cuts is changed individually and one at a time. These are: the minimum number of hits in the strip detector, the minimum pion transverse momentum, the minimum four track vertex fit probability, the maximum ΔR between J/ψ and $\pi\pi$, and the minimum transverse momentum of the pion pair. These results, only made on the prompt Monte Carlo sample, are shown in table 5.11. Due to the small size of the signal sample at hand the variations on the final result are dominated to a large extent by statistics. The total uncertainty does not contain this. The varying of the p_T region of the analysis, which implies recalculating of all the terms of the correction factors and a physical different region in data, shows a good stability of the Monte Carlo, in the statistical uncertainty limit. The contribution from statistics fluctuations will be study in further analysis.

5.1.5 Data-driven cross check of pion acceptance and efficiency

It is possible a verification of the simulated pion pair acceptance and efficiency with a measurement of the candidate yields of the two decay channels of the $\psi(2S)$: $\rightarrow J/\psi(\rightarrow \mu^+\mu^-)\pi^+\pi^-$ and $\psi(2S) \rightarrow \mu^+\mu^-$. Their branching ratio are respectively: $33.6 \pm 0.4\%$ and $(7.7 \pm 0.8)\%$ [30]. Correcting for this branching ratio and differences in acceptance and efficiency of the muon pair, the difference between the two decays can be attributed to the efficiency and acceptance of the pion pair. This study is done both for data and Monte Carlo samples, in order to evaluate an eventual difference in the results, that indicate problems in the description of the pion pair reconstruction by the simulation. The study is performed in the kinematic region of the analysis: $p_T(\psi(2S)) > 8\,GeV/c$ and $|y(\psi(2S))| < 2.2$; the same trigger and dataset are analysed to extract the yield from data. The invariant mass spectrum for the $\mu^+\mu^-$ pair is shown in figure 5.19.

Unbinned log likelihood fit to the $\mu^+\mu^-$ is performed in order to extract the number of candidates. In the $\psi(2S)$ signal region, a double Gaussian function is used, while in the background region, an exponential function is adopted. The parameters of the fit are shown in table 5.12.

Table 5.11: Results for the yields and the corrected ratio for the prompt component for the different changes in the selection cuts affecting the $\pi\pi$ system.

Cut	$N(X(3872))$	$N(\psi(2S))$	$A_{\pi\pi} \times \epsilon_{\pi\pi}$	**Meas.**	**% diff.**
$nr_{Strip\ hits} > 7$	416 ± 102	6151 ± 144	1.102 ± 0.019	0.083 ± 0.020	-9.7%
$nr_{Strip\ hits} > 9$	398 ± 85	5258 ± 132	1.107 ± 0.020	0.093 ± 0.020	$+0.6\%$
$nr_{Strip\ hits} > 11$	326 ± 71	4017 ± 112	1.109 ± 0.022	0.099 ± 0.022	$+7.2\%$
$p_T(\pi) > 350\,MeV/c$	600 ± 144	7676 ± 175	1.087 ± 0.016	0.097 ± 0.024	$+5.7\%$
$p_T(\pi) > 450\,MeV/c$	500 ± 120	6894 ± 165	1.120 ± 0.017	0.088 ± 0.021	-4.7%
$p_T(\pi) > 500\,MeV/c$	489 ± 113	6468 ± 146	1.131 ± 0.017	0.091 ± 0.020	-1.6%
$p_T(\pi) > 550\,MeV/c$	469 ± 99	5961 ± 146	1.144 ± 0.018	0.093 ± 0.020	$+0.1\%$
$p_T(\pi) > 600\,MeV/c$	434 ± 95	5306 ± 112	1.148 ± 0.019	0.097 ± 0.021	$+5.1\%$
$\Delta R < 0.55$	432 ± 104	7286 ± 170	0.969 ± 0.015	0.083 ± 0.020	-10.0%
$\Delta R < 0.6$	482 ± 111	7365 ± 172	1.030 ± 0.015	0.086 ± 0.020	-6.4%
$\Delta R < 0.65$	526 ± 120	7302 ± 172	1.074 ± 0.016	0.091 ± 0.021	-1.4%
$\Delta R < 0.75$	518 ± 124	7383 ± 176	1.112 ± 0.016	0.086 ± 0.021	-7.2%
$\Delta R < 0.8$	533 ± 105	7479 ± 171	1.117 ± 0.016	0.086 ± 0.017	-6.2%
$\Delta R < 0.85$	511 ± 116	7430 ± 163	1.118 ± 0.016	0.083 ± 0.019	-9.5%
$P(Vtx) > 0.02$	527 ± 121	7272 ± 158	1.082 ± 0.018	0.091 ± 0.020	-1.5%
$P(Vtx) > 0.05$	524 ± 120	7128 ± 156	1.080 ± 0.018	0.092 ± 0.021	$+0.2\%$
$p_T(\pi^+\pi^-) > 1.2\,GeV/c$	561 ± 142	8380 ± 181	1.024 ± 0.015	0.086 ± 0.023	-6.9%
$p_T(\pi^+\pi^-) > 1.3\,GeV/c$	544 ± 183	8133 ± 187	1.047 ± 0.015	0.087 ± 0.029	-6.0%
$p_T(\pi^+\pi^-) > 1.4\,GeV/c$	526 ± 188	7788 ± 126	1.070 ± 0.016	0.086 ± 0.031	-7.0%
$p_T(\pi^+\pi^-) > 1.6\,GeV/c$	536 ± 120	7050 ± 200	1.123 ± 0.017	0.092 ± 0.021	-0.3%
$p_T(\pi^+\pi^-) > 1.7\,GeV/c$	534 ± 119	6595 ± 160	1.152 ± 0.018	0.095 ± 0.021	$+3.2\%$
$p_T(\pi^+\pi^-) > 1.8\,GeV/c$	515 ± 90	6059 ± 129	1.175 ± 0.018	0.098 ± 0.017	$+6.3\%$
$Track\pi\chi^2 < 4$	479 ± 124	7253 ± 162	1.098 ± 0.018	0.082 ± 0.021	-11.5%
$Track\pi\chi^2 < 3$	486 ± 115	7069 ± 167	1.096 ± 0.018	0.085 ± 0.020	-7.7%
$Cand.p_T > 9\,GeV/c$	562 ± 115	7032 ± 172	1.087 ± 0.017	0.096 ± 0.020	$+4.6\%$
$Cand.p_T > 10\,GeV/c$	505 ± 114	6466 ± 165	1.070 ± 0.017	0.092 ± 0.021	-0.3%
$Cand.p_T > 11\,GeV/c$	480 ± 104	5797 ± 151	1.061 ± 0.019	0.092 ± 0.021	$+2.1\%$
$Cand.p_T > 12\,GeV/c$	394 ± 84	4973 ± 133	1.060 ± 0.021	0.092 ± 0.019	-4.0%

Table 5.12: Parameters from the fit of the $\mu^+\mu^-$ invariant mass spectrum.

Parameter	**Value**
$m(\psi(2S))$	3.6815 ± 0.0004
$\sigma1(\psi(2S))$	0.024 ± 0.002
$\sigma2(\psi(2S))$	0.050 ± 0.003
n	-1.27 ± 0.04
$N(\psi(2S))$	13080 ± 170
$N(\text{bkg})$	19740 ± 190
$S/B_{2\sigma}(\psi(2S)$	2.90 ± 0.05
χ^2	1.21

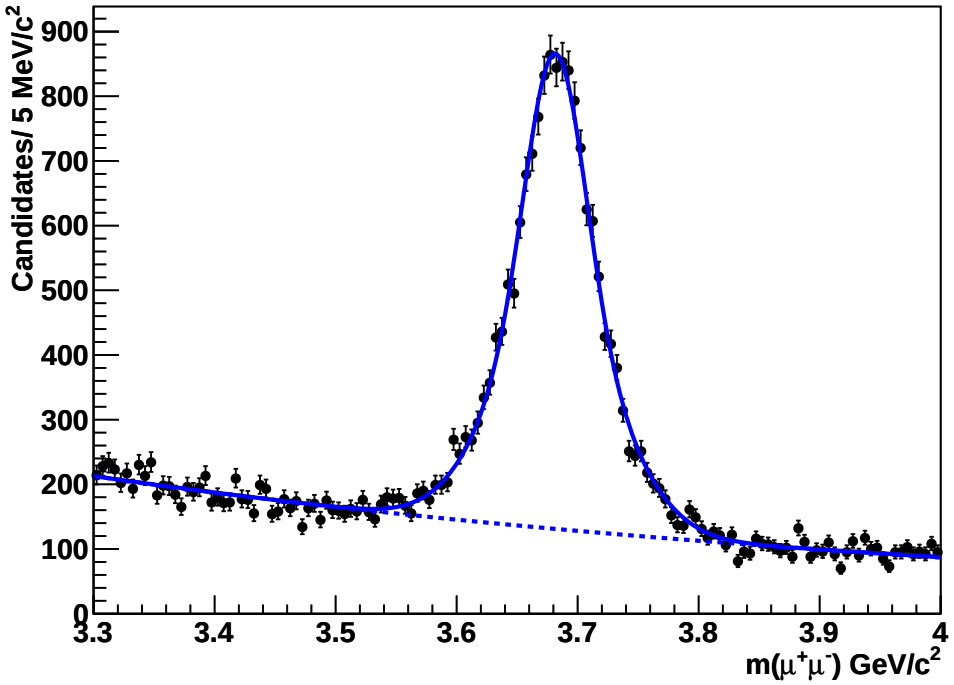

Figure 5.19: Invariant mass spectrum of the $\mu^+\mu^-$ system in the kinematic region: $p_T > 8\,GeV/c$ and $|y| < 2.2$.

In data the yields for the $J/\psi\pi^+\pi^-$ channel is 7346 ± 156 and for the $\mu^+\mu^-$ channel is 13080 ± 170. The ratio of this values is: 0.561 ± 0.014.
The acceptance ratio for the two decay channels is shown in the figure 5.20. The average value, for the kinematic range under investigation, is 0.8476 ± 0.0018.

The ratio of the efficiencies for the $\psi(2S)$ reconstruction in the two decays is shown in figure 5.21. The average value for the kinematic range investigated is 0.737 ± 0.007.

Correcting these values for the branching ratios [30], and for acceptance and efficiency obtained from Monte Carlo simulation (figure 5.22), the obtained value for the product is $A_{\pi\pi}(\psi(2S)) \times \epsilon_{\pi\pi}(\psi(2S)) = 0.35 \pm 0.04$, where the main source of uncertainty is related to the BR($\psi(2S) \to \mu^+\mu^-$). This value is compared very well with the corresponding value from Monte Carlo simulation, $A_{\pi\pi}(\psi(2S)) \times \epsilon_{\pi\pi}(\psi(2S)) = 0.334 \pm 0.004$. The measurement is repeated for different values of the p_T thresholds and the $\Delta R_{\pi\pi}$.
The agreement between data and Monte Carlo simulation, showed in figure 5.22 gives confidence that the pion pair reconstruction is well described from the simulation, within the uncertainties of the method.

To estimate an average pion pair efficiency and pion reconstruction efficiency, for the range of the measurement, the value from the data (0.35 ± 0.04) is divided by the pion

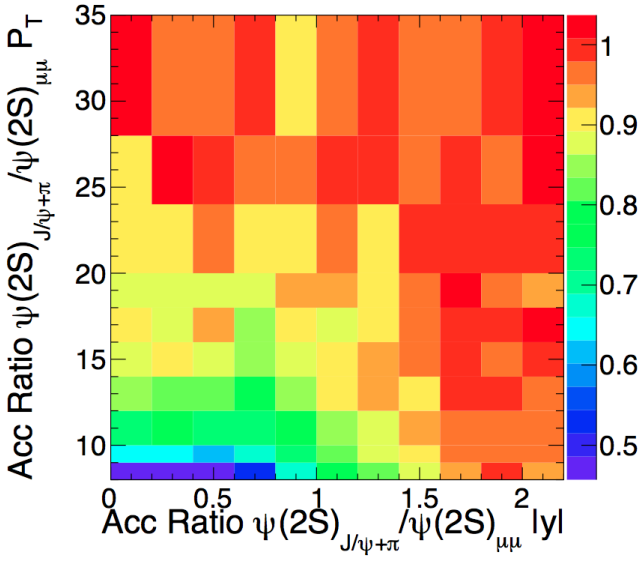

Figure 5.20: Ratio between the acceptance for $\psi(2S) \to J/\psi\pi^+\pi^-$ and $\psi(2S) \to \mu^+\mu^-$.

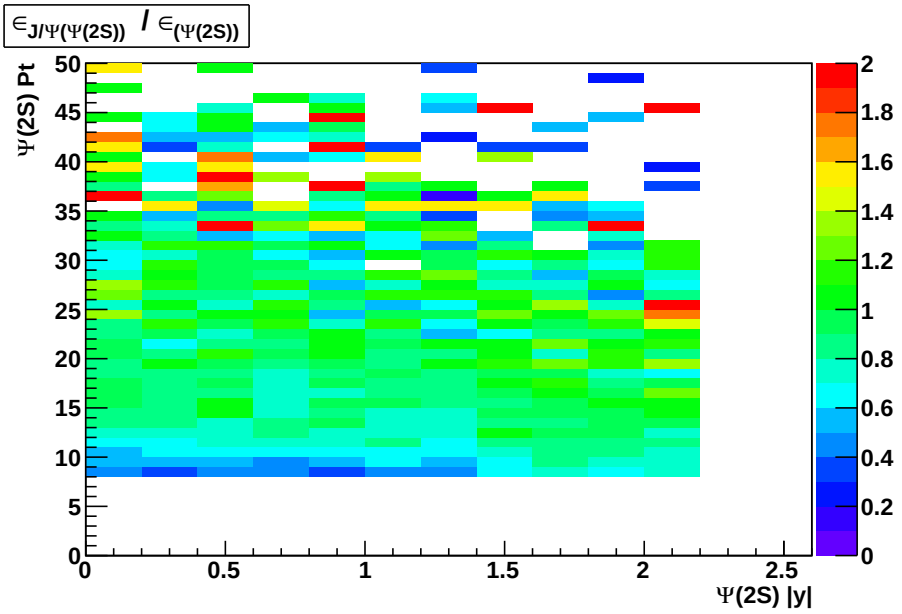

Figure 5.21: Ratio of efficiency for $\psi(2S) \to J/\psi\pi^+\pi^-$ and $\psi(2S) \to \mu^+\mu^-$.

pair acceptance, $A_{\pi\pi} = 0.519 \pm 0.003$ as determined from Monte Carlo (table 5.5): the result is $\epsilon_{\pi\pi}^{data-driv.} = 0.67 \pm 0.08$. The square root of this value is 0.82 ± 0.09 and gives an estimation for the mean value of the reconstruction efficiency for the single pion.

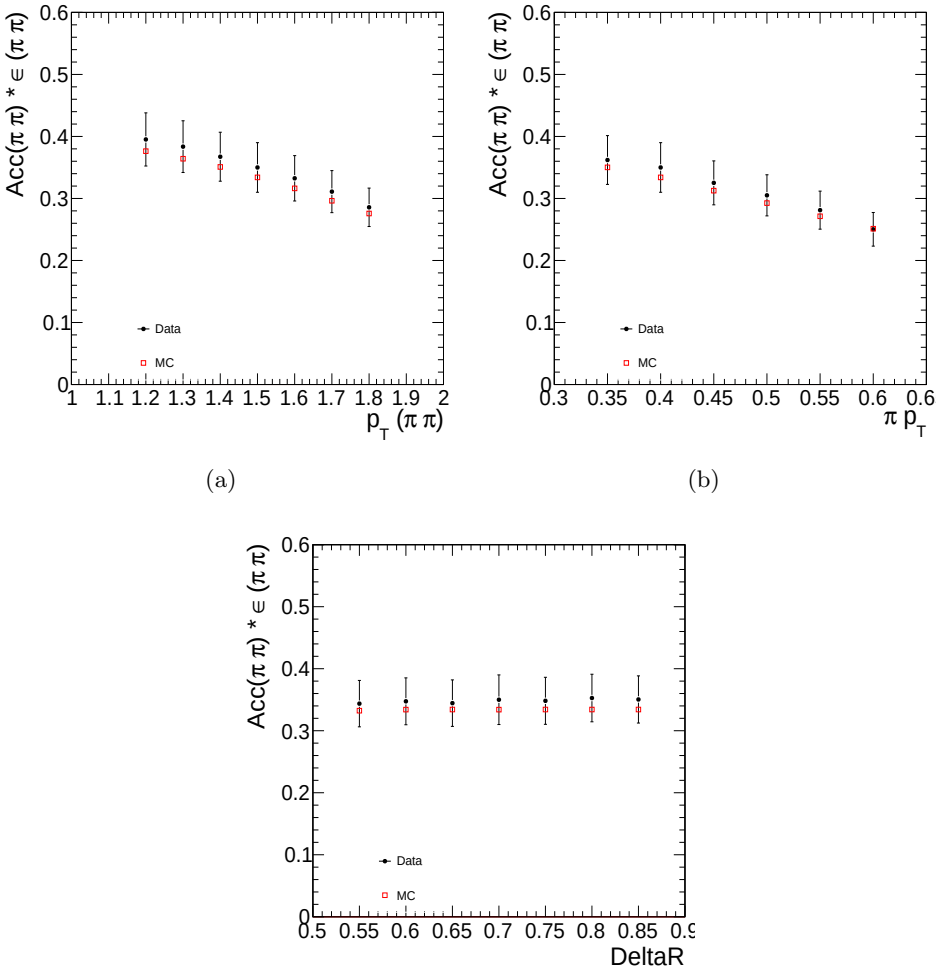

Figure 5.22: Acceptance and efficiency of the pion pair for Monte Carlo (red) and data (black) as function of different kinematic variables: $p_T(\pi\pi)$ (a), $p_T(\pi)$ (b) and ΔR (c). The p_T is measured in GeV/c.

5.1.6 Result

The invariant mass distribution fit, figure 5.16, the numbers of candidates of $X(3872)$ and $\psi(2S)$ obtained from table 5.7 are: $N_{X(3872)} = 548 \pm 104(stat.)$ and $N_{\psi(2S)} = 7346 \pm 155(stat.)$, with the errors of table 5.7. The ratio of "acceptance corrected"yields is:

$$R = \frac{N_{X(3872)}}{N_{\psi(2S)}} \times \frac{1}{C} = \frac{\sigma(pp \to X(3872) + anything) \times BR(X(3872) \to J/\psi\pi^+\pi^-)}{\sigma(pp \to \psi(2S) + anything) \times BR(\psi(2S) \to J/\psi\pi^+\pi^-)} \quad (5.5)$$

Using the correction value of $C = 0.872$ in the ratio of measured signal yields give a result of:

$$R = 0.084 \pm 0.017(stat.) \pm 0.009(syst.) \tag{5.6}$$

The first error comes from the statistical uncertainty of the signal yield in the data, the second error is the systematic uncertainty, as discussed before.

5.1.7 Kinematic properties of the signal using the sideband subtraction method

The sideband subtraction method is used to remove background from the data distributions and facilitate direct comparisons between the data and Monte Carlo simulations of signal events. The method makes use of an invariant mass spectrum and assumes that the continuum events in the sideband regions, the regions close to, but outside the invariant mass signal window, have the same properties and distributions a the background inside the mass signal window. A sideband subtracted distribution is constructed by determining the distribution of events separately in the signal and in the sidebands regions, and subtracting the sidebands distribution, normalized to the width of the sidebands, from the signal distribution. Here, the sideband distribution are extracted separately from two regions, below and above the signal region.

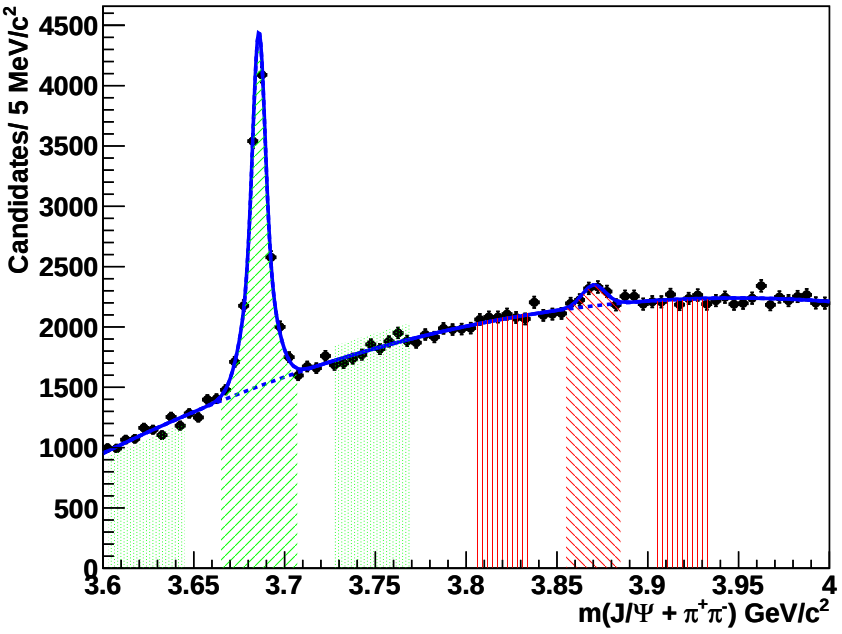

Figure 5.23: Black: data p_T distribution as extracted with the sideband subtraction method, in comparison with the distribution of: blue: Monte Carlo simulation, red: the Monte Carlo re-weighted for the polynomial and, green: for its inverse.

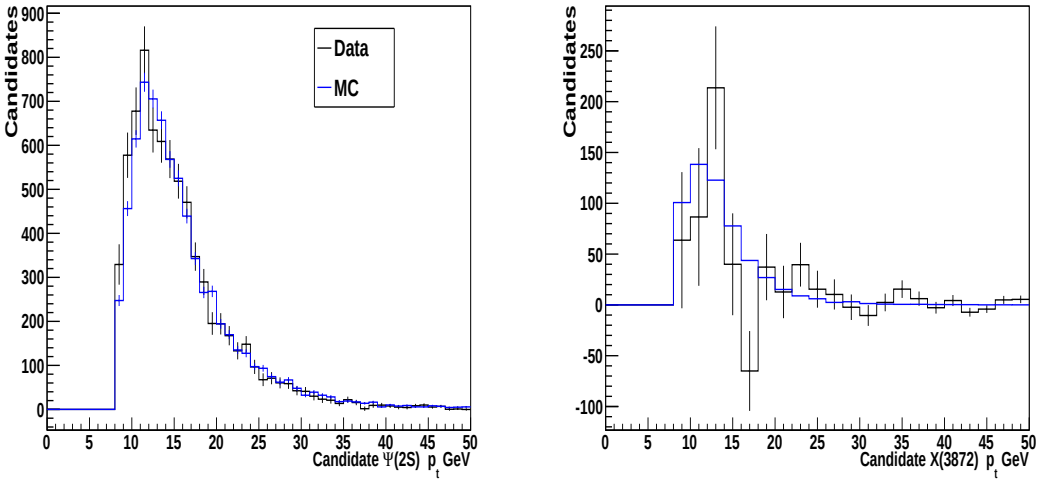

(a) $\psi(2S)$ (b) $X(3872)$

Figure 5.24: Candidate p_T after sideband subtraction, compared Monte Carlo (blue) and data (black) (where GeV is meant to be GeV/c).

Subsequently the two sideband distributions are summed and the summed sideband distribution is normalized to the signal distribution using the integral of the background function in the central and sideband regions. An example is shown in figure 5.24: the choices for the central and sideband regions for both signals, using as a discriminatory factor the invariant mass of the $J/\psi\pi^+\pi^-$ system. The shapes of the distributions for the $\psi(2S)$ show a good agreement between data and Monte Carlo, with deviations within the statistical errors. The $X(3872)$ distributions are strongly limited by statics, due to the low signal to background ratio.
In the figures (5.25, 5.26 and 5.27) are shown the distributions of few variables and compared to the Monte Carlo expectations. The comparison shows a very nice agreement of the two distributions.

Another possible improvement is for the cut on the transverse momentum of the pions 5.28. One possibility is to choose different values for the higher (*hard*) and lower (*soft*) pion. It is possible to increase the value of the cut, and it is also differentiate. On the soft pion it is possible to cut at an higher value, $p_T^{soft} \geq 700\,MeV/c$, and on the hard pions its $p_T^{hard} \geq 1000\,MeV/c$. In this way the wrong combinations will be reduced by a factor 3.

5.2 The 2011 data

In the 2011 the huge amounts of collected data allows to continue the study on the $X(3872)$ particle. The performance of the LHC has increased the acquisition of about 200 times

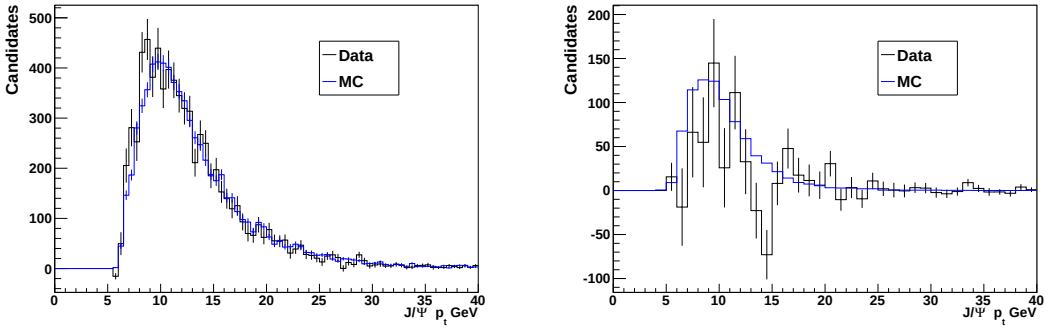

(a) $\psi(2S)$ (b) $X(3872)$

Figure 5.25: Distribution of the J/ψ p_T after sideband subtraction, compared Monte Carlo (blue) and data (black) (where GeV is meant to be GeV/c).

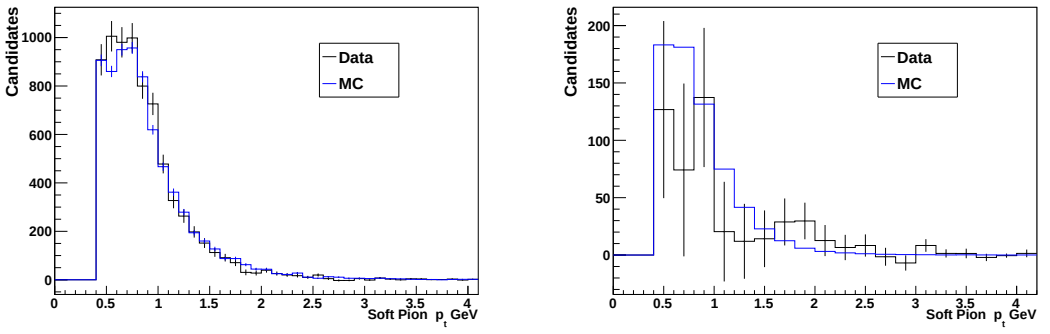

(a) $\psi(2S)$ (b) $X(3872)$

Figure 5.26: Lower momentum pion p_T distribution after sideband subtraction, compared Monte Carlo (blue) and data (black) (where GeV is meant to be GeV/c).

with respect to the 2010 data. The total collected data, up to July, is about $\sim 1\, fb^{-1}$. The great number of collisions need a important improvement of the trigger system, in particular for this analysis, there are the addition of new HLT trigger. The principal trigger used are the *HLT_Dimuon7_Jpsi_X_Barrel_v1/3* and *HLT_Dimuon6p5_Jpsi_Barrel_v1*. They require that $p_T^{\mu\mu} > (6.5)7\, GeV/c$ respectively and that the events lie in the barrel region ($|\eta| < 1.2$).

At the trigger level the transverse momentum of the J/ψ has to be greater than $7\, GeV/c$, must lie in the rapidity region $|y| < 1.25$ and the candidate have to stay in the mass window of $2.95\, GeV/c^2 < m < 3.25\, GeV/c^2$. The muons are accepted if they are in a good acceptance region: $p_T > 4\, GeV/c$ for $|\eta| < 1.3$ and $p_T > 3.3\, GeV/c$ for $1.3 < |\eta| < 2.4$. The probability vertex of the dimuon system is required to be greater than 1%. The J/ψ candidates are kept if they lie in the mass window $3.019\, GeV/c^2 < m_{J/\psi} < 3.167\, GeV/c^2$.

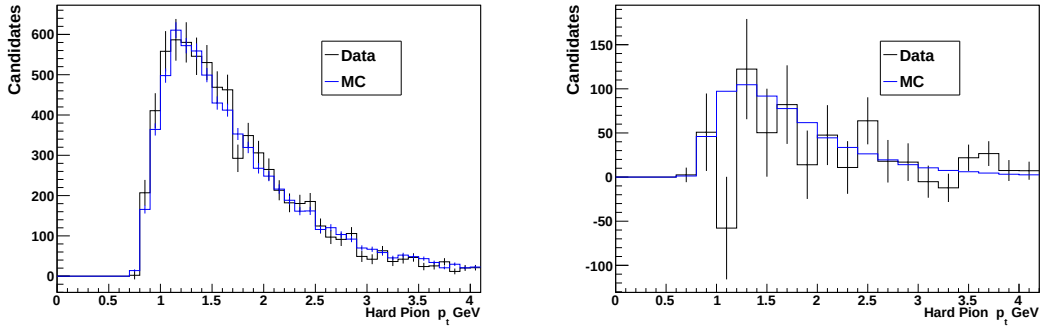

(a) $\psi(2S)$ (b) $X(3872)$

Figure 5.27: Higher momentum pion p_T distribution after sideband subtraction, compared Monte Carlo (blue) and data (black) (where GeV is meant to be GeV/c).

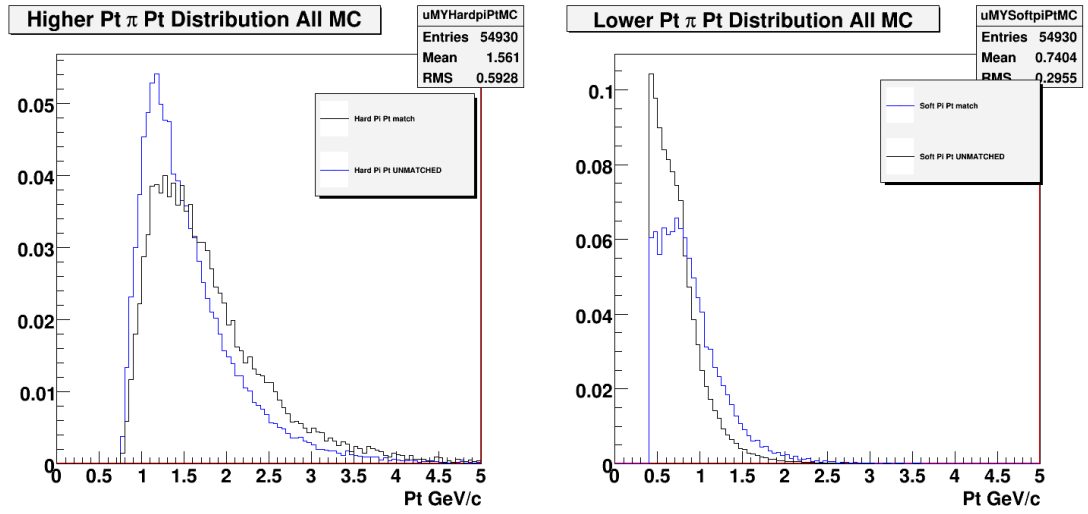

(a) Hard pion (b) Soft pion

Figure 5.28: p_T of the pions.

The tracks selection has been modified a little: the minimum transverse momentum is $p_T > 0.6\,GeV/c$ and the ΔR between the J/ψ and both pions has to be smaller than 0.7. The $X(3872)$ candidate is required to be in a specific rapidity region ($|y| < 1.25$) and to have an higher transverse momentum ($p_T > 9\,GeV/c$). The four vertex probability has to be grater than 1%, as in the 2010 selection.

The resultant invariant mass spectrum is shown in figure 5.29. The fitting is made using a Gaussian function for the $\psi(2S)$ peak and a Gaussian function for the $X(3872)$, the background is fitted with a Čebyšëv polynomial.

The measurement of the non prompt fraction in the $X(3872)$ sample can be done with

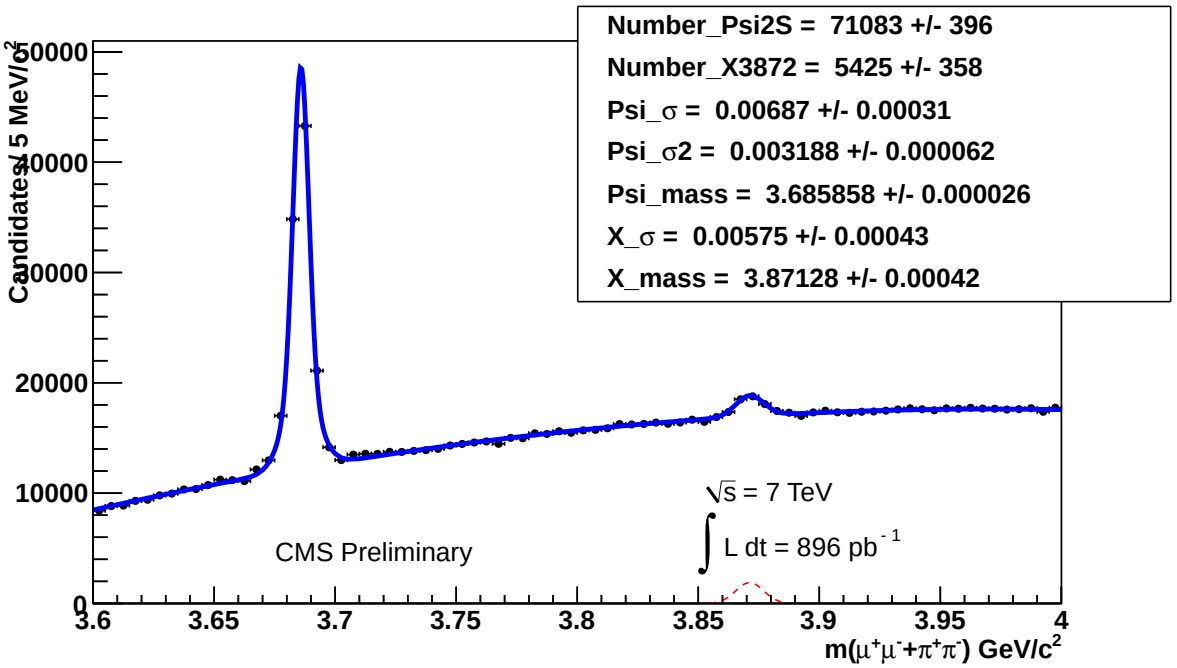

Figure 5.29: Invariant mass spectrum of the 2011 data, $\sim 900\,pb^{-1}$. The numbers of the fit are in the box.

the system 5.3. The figures of the mass spectrum after and before the cut on $c\tau > 0.1\,mm$ are shown in 5.30. The efficiencies are those from the Monte Carlo measurements. The calculation for the $\psi(2S)$ and for the $X(3872)$ gives results:

$$N^{non-prompt}_{\psi(2S)}/N_{\psi(2S)}(cuts) = 0.512 \pm 0.006(stat.)$$
$$N^{non-prompt}_{X(3872)}/N_{X(3872)}(cuts) = 0.163 \pm 0.033(stat.)$$

The difference with respect to the 2010 results for the $X(3872)$ measurements is $\sim 1.4\sigma$, so the two measurements are compatible.

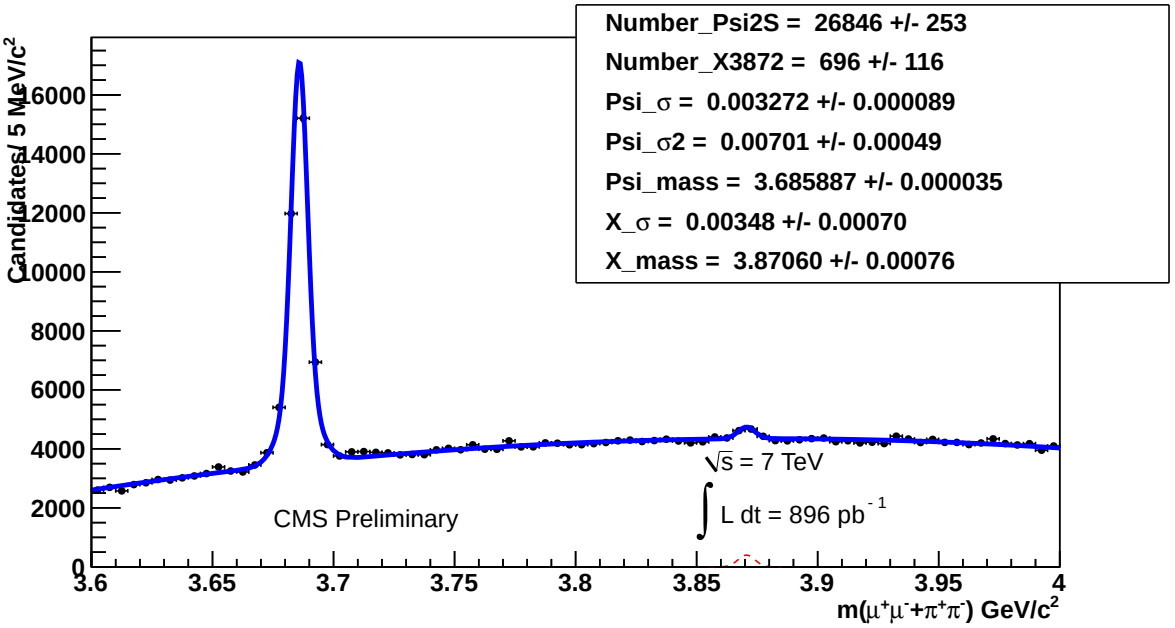

Figure 5.30: Invariant mass spectrum after the $c\tau > 0.1\,mm$ cut: the fitting functions are the same (double Gaussian for $\psi(2S)$, a Gaussian for the $X(3872)$ and a Čebyšëv polynomial foor the background. The fitting numbers are in the box.

6

Conclusions and prospects

This work has presented a measurement of the $X(3872)$ particle production in pp collisions at $\sqrt(s) = 7\,TeV$ at CMS, in the decay mode into a J/ψ and a pion pair.
The measurement is being performed with the $\sim 40\,pb^{-1}$ collected in 2010, and the cross section has been measured relative to the production of $\psi(2S)$ decaying into the same final state, in such a way factorizing most of the uncertainties. The accuracy is limited to about 20% due to the statistical error, while the systematics is $\sim 10\%$ About 500 events are reconstructed in 2010. The larger data set collected by CMS up to July 2011 ($\sim 1\,fb^{-1}$) has allowed a much better statistical evidence of such a decay, while the systematic uncertainties are still under evaluation. Where possible data-driven methods are used to validate the analysis, especially in the pion tracking efficiency.
By using the large lifetime of the $B-$hadrons, as reconstructed by the distance of the $X(3872)$ decay vertex from the collision primary vertex, and by making use of the Monte Carlo simulation efficiency estimate, I have shown a first measurement of the fraction of $X(3872)$ decays from $B-$hadrons. The results of 2011 indicate that about 16% of the $X(3872)$ originate from the decays of the $B-$hadrons, for an average p_T of the $X(3872)$ of about $15\,GeV/c$. The result is obtained for the $B-$fraction of $\psi(2S)$ decays for this particular momentum range agrees within uncertainties with an independent analysis performed in the decays of the $\psi(2S)$ into muon pairs, thus giving confidence on the method. The statistics collected in 2011 and the one which will be collected in 2012, will certainly allow to study the properties of the $X(3872)$: its mass, the spin and parity among others. These will contribute to the understanding of the nature of such an exotic state.

Bibliography

[1] The CMS coll. **The CMS experiment at the CERN LHC. The Compact Muon Solenoid experiment**. *J. Instrum.*, **3**:S08004, 2008. Also published by CERN Geneva in 2010. 5, 11, 15

[2] CMS collaboration. **Electromagnetic calorimeter commissioning and first results with 7 TeV data**. Technical Report CMS-NOTE-2010-012, CERN, Geneva, Jul 2010. 10

[3] Martina Malberti. **Operation and performance of the CMS Electromagnetic Calorimeter**. Technical Report CMS-CR-2011-040, CERN, Geneva, Mar 2011. 10

[4] The TOTEM Collaboration. **The TOTEM Experiment at the CERN Large Hadron Collider**. *Journal of Instrumentation*, **3**(08):S08007, 2008. 13

[5] Gaelle Boudoul. **CMS Silicon Strip Tracker Operation and Performance**. Technical Report CMS-CR-2011-042, CERN, Geneva, Mar 2011. 19

[6] Andrea Venturi. **CMS Tracking, Alignment and Physics Performances results**. Technical Report CMS-CR-2010-183, CERN, Geneva, Oct 2010. 21

[7] CMS collaboration. **Tracking and Vertexing Results from First Collisions**. Technical Report CMS PAS TRK-10-001, CERN, 2010. 21

[8] G Flucke, P Schleper, and M Stoye. **CMS silicon tracker alignment strategy with the Millepede II algorithm**. *Journal of Instrumentation*, **3**(09):P09002, 2008. 21

[9] Veikko Karimäki, Tapio Lampen, and Frank-Peter Schilling. **The HIP Algorithm for Track Based Alignment and its Application to the CMS Pixel Detector**. Technical Report CMS-NOTE-2006-018, CERN, Geneva, Jan 2006. 21

[10] Rudolph Emil Kalman. **A New Approach to Linear Filtering and Prediction Problems**. *Transactions of the ASME–Journal of Basic Engineering*, **82**(Series D):35–45, 1960. 23

[11] CMS collaboration. **Performance of muon identification in pp collisions at $\sqrt{s}$ = 7 TeV**. Technical Report CMS-PAS-MUO-10-002, CERN, 2010. 26

[12] CMS collaboration. **Measurement of Tracking Efficiency**. Technical Report CMS-PAS-TRK-10-002, CERN, 2010. 26, 31

[13] CMS collaboration. **The CMS muon project: Technical Design Report**. Technical report, CERN, 1997. 26

[14] CMS collaboration. **Prompt and non-prompt cross sections in J/ψ collision at pp = 7 TeV$\sqrt{s}$**. (CMS-PAS-BPH-10-002), 2010. 30, 62, 63, 71

[15] CMS collaboration . **Measurements of inclusive W and Z cross sections in pp collisions at $\sqrt{s} = 7$TeV**. *Journal of High Energy Physics*, **2011**:1–40, 2011. 10.1007/JHEP01(2011)080. 31

[16] J. D. Bjorken. **Asymptotic Sum Rules at Infinite Momentum**. *Phys. Rev. Lett.*, **179**:1547–1553, 1969. 35

[17] David J. Griffiths. *Introduction to elementary particles*. John Wiley and Sons, Inc., 1987. 36

[18] G. D. Rochester and C. C. Butler. **Evidence for the existence of new unstable elementary particles**. *Nature*, **160**:855–857, 1947. 36

[19] Steven Weinberg. **A Model of Leptons**. *Phys. Rev. Lett.*, **19**:1264–1266, 1967. 38

[20] G. Arnison et al. **Experimental observation of lepton pairs of invariant mass around $95 - GeV/c^2$ at the CERN SPS collider**. *Phys. Lett.*, **B126**:398–410, 1983. 38

[21] G. Arnison et al. **Experimental observation of isolated large transverse energy electrons with associated missing energy at $\sqrt{s}$ = 540-GeV**. *Phys. Lett.*, **B122**:103–116, 1983. 38

[22] G Zweig. **An SU_3 model for strong interaction symmetry and its breaking; Part II**. (CERN-TH-412):80 p, Feb 1964. 38

[23] M. Gell-Mann. **A Schematic model of baryons and mesons**. *Phys. Lett.*, **8**:214–215, 1964. 38

[24] J. J. Aubert et al. **Experimental Observation of a Heavy Particle J**. *Phys. Rev. Lett.*, **33**:1404–1406, 1974. 39

[25] J. E. Augustin et al. **Discovery of a Narrow Resonance in e^+ e^- Annihilation**. *Phys. Rev. Lett.*, **33**:1406–1408, 1974. 39

[26] S. L. Glashow, J. Iliopoulos, and L. Maiani. **Weak Interactions with Lepton-Hadron Symmetry**. *Phys. Rev. D*, **2**(7):1285–1292, 1970. 39

[27] S. W. Herb et al. **Observation of a Dimuon Resonance at 9.5 GeV in 400-GeV Proton-Nucleus Collisions**. *Phys. Rev. Lett.*, **39**:252–255, 1977. 39

[28] Abe et al. **Observation of Top Quark Production in $p\bar{p}$ Collisions with the Collider Detector at Fermilab**. *Phys. Rev. Lett.*, **74**:2626–2631, 1995. 39

[29] W. Heisenberg. **Über den Bau der Atomkerne. I**. *Zeitschrift für Physik A Hadrons and Nuclei*, **77**, 1932. 39

[30] K. Nakamura et al. (Particle Data Group). **Review of Particle Physics**. *J. Phys. G*, **37**(7A), 2010. 075021. 40, 56, 59, 62, 66, 78, 80

[31] Remortel van Nick et al. Aaltonen. **Evidence for a narrow near-threshold structure in the $J/\psi\phi$ mass spectrum in $B^+ \to J/\psi\phi K^+$ decays**. *Phys. Rev. Lett.*, **102**:242002, 2009. 50

[32] S.K. Choi et al. **Observation of a Resonance like Structure in the $\pi^{+-}\psi'$ Mass Distribution in Exclusive $B \to K\pi^{\pm}\psi'$ Decays**. *Phys. Rev. Lett.*, **100**(14):142001, 2008. 50

[33] S. K. Choi et al. **Observation of a new narrow charmonium state in exclusive $B^{\pm} \to K^{\pm}\pi^+\pi^- J/\psi$ decays**. *Phys. Rev. Lett.*, **91**:262001, 2003. 50

[34] D. Acosta et al. **Observation of the narrow state $X(3872) \to \pi^+\pi^- J/\psi$ decays**. *Phys. Rev. Lett.*, **91**:262001, 2003. 50

[35] A. Abulencia et al. **Analysis of the quantum numbers J^{PC} of the X(3872)**. *Phys. Rev. Lett.*, **98**:132002, 2007. 52

[36] K. Abe et al. **Evidence for $X(3872) \to \gamma J/\psi$ and the sub-threshold decay $X(3872) \to \omega J/\psi$**. 2005. 52, 55

[37] Nils A. Törnqvist. **From the deuteron to deusons, an analysis of deuteron - like meson meson bound states**. *Z. Phys.*, **C61**, 1994. 53

[38] Eric S. Swanson. **Short range structure in the X(3872)**. *Physics Letters B*, **588**(3-4):189–195, 2004. 53

[39] Harald Fritzsch. **Producing heavy quark flavors in hadronic collisions–' A test of quantum chromodynamics**. *Physics Letters B*, **67**(2):217–221, 1977. 55

[40] F. Halzen. **CVC for gluons and hadroproduction of quark flavours**. *Physics Letters B*, **69**(1):105–108, 1977. 55

[41] J.F. Amundson, O.J.P. Éboli, E.M. Gregores, and F. Halzen. **Quantitative tests of color evaporation: charmonium production**. *Physics Letters B*, **390**(1-4):323–328, 1997. 55

[42] J.F. Amundson, O.J.P. Éboli, E.M. Gregores, and F. Halzen. **Colorless states in perturbative QCD: Charmonium and rapidity gaps**. *Physics Letters B*, **372**(1-2):127–132, 1996. 55

[43] Edmond L. Berger and D. Jones. **Heavy quark contributions to inelastic photoproduction of the J/ψ, T, and other states**. *Physics Letters B*, **121**(1):61–64, 1983. 55

[44] W. E. Caswell and G. P. Lepage. **Effective lagrangians for bound state problems in QED, QCD, and other field theories**. *Physics Letters B*, **167**(4):437–442, 1986. 55

[45] CMS collaboration. **Measurement of the production cross section ratio of $X(3872)$ and $\psi(2S)$ in the decays to $J/\psi\pi^+\pi^-$ in pp collisions at $\sqrt(s) = 7$ TeV**. (CMS-PAS-BPH-10-018), 2010. 60

[46] Torbjörn Sjöstrand, Stephen Mrenna, and Peter Z. Skands. **PYTHIA 6.4 Physics and Manual**. *JHEP*, **05**, 2006. 60

[47] D. J. Lange. **The EvtGen particle decay simulation package**. *Nucl. Instrum. Meth.*, **A462**, 2001. 60

[48] CMS collaboration. **CMS Analysis Note, AN-10-453**. 2010. 64

[49] CMS collaboration. **CMS Analysis Note, AN-10-083**. 2010. 64

[50] CMS collaboration. https://twiki.cern.ch/ twiki/bin/view/CMSPublic/PhysicsResultsBPH1001 [link]. 73

[51] CMS collaboration. **Measurement of Tracking Efficiency, CMS PAS TRK-10-002**. 2010. 76